ISTANBUL TECHNICAL UNIVERSITY ★ GRADUATE SCHOOL

NICKEL AND COBALT BORIDE BASED HIGH-CAPACITY ELECTRODES: PRODUCTION, CHARACTERIZATION AND SUPERCAPACITOR PERFORMANCE

Ph.D. THESIS

Mehtap ARSLAN KABA

Department of Metallurgical and Materials Engineering

Metallurgical and Materials Engineering Programme

JANUARY 2026

ISTANBUL TECHNICAL UNIVERSITY ★ GRADUATE SCHOOL

NICKEL AND COBALT BORIDE BASED HIGH-CAPACITY ELECTRODES: PRODUCTION, CHARACTERIZATION AND SUPERCAPACITOR PERFORMANCE

Ph.D. THESIS

Mehtap ARSLAN KABA
(506192418)

Department of Metallurgical and Materials Engineering

Metallurgical and Materials Engineering Programme

Thesis Advisor: Prof. Dr. Güldem KARTAL ŞİRELİ

JANUARY 2026

İSTANBUL TEKNİK ÜNİVERSİTESİ ★ LİSANSÜSTÜ EĞİTİM ENSTİTÜSÜ

NİKEL VE KOBALT BORÜR ESASLI YÜKSEK KAPASİTELİ ELEKTROTLAR: ÜRETİMİ, KARAKTERİZASYONU VE SÜPERKAPASİTÖR PERFORMANSI

DOKTORA TEZİ

Mehtap ARSLAN KABA
(506192418)

Metalurji ve Malzeme Mühendisliği Anabilim Dalı

Metalurji ve Malzeme Mühendisliği Programı

Tez Danışmanı: Prof. Dr. Güldem KARTAL ŞİRELİ

OCAK 2026

Mehtap ARSLAN KABA, a Ph.D. student of ITU Graduate School student ID 506192418, successfully defended the dissertation entitled “NICKEL AND COBALT BORIDE BASED HIGH-CAPACITY ELECTRODES: PRODUCTION CHARACTERIZATION AND SUPERCAPACITOR PERFORMANCE”, which she prepared after fulfilling the requirements specified in the associated legislations, before the jury whose signatures are below.

Thesis Advisor : **Prof. Dr. Güldem KARTAL ŞİRELİ** ....
Istanbul Technical University

Jury Members : **Prof. Dr. Servet TİMUR** ....
Istanbul Technical University

Assist. Prof. Dr. Hatice Kübra AKBEN ....
Yeditepe University

Prof. Dr. Sebahattin GÜRMEN ....
Istanbul Technical University

Prof. Dr. Gökhan ORHAN ....
Istanbul University-Cerrahpaşa

Date of Submission : 22 December 2025
Date of Defense : 20 January 2026

To my family and friends,

FOREWORD

During my doctoral studies, I would like to express my deepest gratitude to my doctoral advisor, Prof. Dr. Güldem KARTAL ŞIRELI, my "academic mother," who has supported me for years with her vast knowledge and experience, standing by me through every challenge. I am also thankful to my esteemed mentor, Prof. Dr. Servet TIMUR, to whom I have always turned for advice; his academic wisdom and human insight have continuously illuminated my path.

I am profoundly grateful to my beloved husband and companion, M.Sc. Mertcan KABA, who has lifted me up every time I stumbled and has been my greatest source of strength and encouragement throughout this entire academic journey.

I also owe my heartfelt thanks to my dear colleagues and friends Dr. Yonca ALKAN GÖKSU, Dr. Esra BAŞTÜRKCÜ, M.Sc. Osman Can ÖZER, Res. Asst. Simay YANIK, Dr. Mehran KARIMZADEHKHOEI, Res. Asst. Utku Orçun GEZICI and Res. Asst. Deniz NALCI together with Dr. Selim ERTÜRK and all my other cherished friends, with whom I have shared laughter, tears, and countless hours of work side by side. My sincere thanks also go to my lifelong friends and sisters since my undergraduate years, M.Sc. Yasemin YEŞILÇIÇEK and M.Sc. Merve VATANSEVER, for always being there for me.

To my dearest family Tülay ARSLAN, Sadık ARSLAN, Tolga ARSLAN, Suzan ARSLAN, Zehra ARSLAN, and Mahmut ARSLAN thank you for your unconditional love and support. Life would not have been as easy or as meaningful without you.

As a woman engineer, I owe special gratitude and respect to the founder father of the Republic of Türkiye, Mustafa Kemal ATATÜRK, and his comrades-in-arms, for enabling women like me to pursue higher education, specialize in our fields, and achieve the title of Doctor.

I would like to thank to Prof. Dr. Kürşat KAZMANLI, Prof. Dr. Hüseyin ÇIMENOĞLU, Prof. Dr. Murat BAYDOĞAN, Dr. Cem ÖRNEK and Dr. Nuri SOLAK, for allowing me to use their laboratory facilities, and to the entire ITU Metallurgical and Materials Engineering family for their support and collaboration.

I would also like to thank the ITU BAP for their financial support under the General Research Project (GAP), Project No. MGA-2023-44676.

Finally, to everyone who has contributed, even in the smallest way, to this doctoral journey completed with persistence and patience I am sincerely grateful. I am truly glad that each of you exists.

January 2025 Mehtap ARSLAN KABA
(M.Sc.)

TABLE OF CONTENTS

Page

ABBREVIATIONS

CRTD-Bor : Cathodic Reduction and Thermal Diffusion based Boriding
CV : Cyclic Voltammetry
EDLC : Electrical Double Layer Capacitor
EDS : Energy Dispersive Spectrsocopy
EIS : Empedance Spectroscopy
EPMA : Electron Probe Microanalysis
FTIR : Fourier transform infrared spectroscopy
GCD : Galvanosttaic Charge-Discharge
PH : Phase Homogenization
SEM : Scanning Electron Microscopy
WDX : Wavelength Dispersive X-ray Spectrometry
XPS : X-Ray Photoelectron Spectroscopy
XRD : X-Ray Diffraction Spectroscopy

SYMBOLS

C_a : Areal Capacitance
C_s : Specific Capacitans
µm : Micrometer
C : Celsius
F : Farad
mF : Milli Farad
T : Temperature
V : Volt
mV : Milli Volt
mA : Milli Amper
cm : Centimeter
W : Watt
h : Hour

LIST OF TABLES

Page

LIST OF FIGURES

Page

NICKEL AND COBALT BORIDE BASED HIGH-CAPACITY ELECTRODES: PRODUCTION, CHARACTERIZATION AND SUPERCAPACITOR PERFORMANCE

SUMMARY

The extensive consumption of fossil fuels, coupled with global population growth, has resulted in the depletion of natural resources and significant environmental pollution. Consequently, the demand for green and sustainable energy has increased alongside technological advancements to address global environmental challenges. This stuation lead to search new advancements in energy storage. Rechargeable batteries, a primary type of electrochemical energy storage device, are widely used in electric and hybrid vehicles, laptops, phones, and medical devices. However, limitations such as low power density, restricted capacity, and short rechargeable lifespan have driven the search for alternative solutions. Supercapacitors, distinguished with superior power density, enhanced charge/discharge rates, and longer service lifespan, are regarded as promising energy storage materials and are anticipated to become the next generation of energy storage components.

Borides have garnered significant attention due to their unique electronic structure. The electron-deficient nature of boron enables the formation of various bonding configurations and stable boride phases with diverse stoichiometries. This structural characteristic increases the diversity of faradaic reactions, thereby enhancing electrode performance. In addition, boron exhibits higher electrical conductivity than most other non-metallic elements, which facilitates the achievement of greater areal and specific capacitance. Among the borides, transition metal borides have remarkable features for supercapacitor applications. The multiple oxidation states makes them ideal for the pseodocapacitors electrodes since it enhances the cycle life of the electrodes. Nickel and cobalt are distinguished amid the other transition metals due to their electrocatalytic properties. The combination of superior propoerties of Ni, Co together with B results in high energy and power density supercapacitor electrodes with long service life.

Numerous methods for producing metal borides have been reported in the literature. Depending on industrial developments, several techniques enable the mass production of high-purity borides. These include borothermal, carbothermic, and metallothermic reduction from metal oxides, mechanochemical synthesis, chemical reduction-based precipitation, hydrothermal or solvothermal synthesis, and thin film deposition. Despite their widespread use, these methods often impede the production of homogeneous and high-purity materials and present environmental and health risks. In contrast, molten salt electrolysis with oxide based electrolytes has emerged as an environmentally friendly, cost-effective, and rapid production technique. This approach does not require expensive equipment, not generate toxic gases or solid waste, and offers innovative potential for various engineering applications. Consequently, molten salt electrolysis provides an economical and efficient production method that avoids costly components and waste generation, thereby advancing the field of engineering applications.

This thesis presents the synthesis and comprehensive investigation of the structural and electrochemical properties of nickel and cobalt boride electrodes fabricated using a novel molten salt electrolysis technique for supercapacitor applications. Pure nickel substrates with two distinct geometries, flat and foam, were subjected to boriding in a borax-based electrolyte through cathodic reduction and thermal diffusion-based boriding (CRTD-Bor). The formation of nickel boride phases, specifically NiB, Ni_4B_3, and Ni_2B, arranged from the surface inward within the nickel matrix, was confirmed by X-ray diffractometry (XRD) and scanning electron microscopy (SEM) equipped with an electron probe microanalyzer (EPMA). Electrochemical properties of the resulting electrodes were evaluated using cyclic voltammetry (CV), galvanostatic charge-discharge (GCD), and electrochemical impedance spectroscopy (EIS). After 2000 CV cycles at a scan rate of 10mV/s, the capacitance values of the nickel boride electrodes reached 478 mF/cm^2 for the flat sample and 1385 mF/cm^2 for the foam sample. The reaction kinetics followed a mixed-controlled model as described by the Trasatti approach. The capacitive contribution (C_o) was significantly higher in the flat electrode at 71%, compared to 40.6% in the foam electrode. The mechanisms underlying the faradaic reactions were investigated using X-ray photoelectron spectroscopy (XPS) and Fourier Transform Infrared Spectroscopy (FTIR) before and after CV experiments. The results suggest that the mechanism is associated with the formation of Ni-O bonds resulting from oxygen saturation at defective sites on the nickel boride surfaces during electrochemical testing. Additionally, the influence of electrode geometry on electrochemical behavior and performance was systematically examined. The findings indicate that a porous structure facilitates greater energy storage and enhances rapid charge-discharge behavior, thereby increasing the power density of the electrodes.

In addition, Ni-boride powders were synthesized by CRTD-Bor, followed by structural and electrochemical characterizations. Nickel specimens with mesh geometry underwent complete cross-sectional boriding at 1000 °C and 200 mA/cm^2 for 2 hours, then were held in molten electrolyte for 1 hour to achieve phase homogenization (PH). Post-boriding, the fully boron-diffused specimens were ground using a ball mill and cold-pressed. Structural characterization of the Ni-boride powders was performed using XRD, SEM and TEM. The analysis revealed that the powders consisted of NiB, Ni_4B_3, Ni_2B, and Ni_3B, with Ni_4B_3 as the predominant phase. Electrochemical behavior of the produced electrodes was evaluated using CV and GCD techniques in a standard 3-electrode configuration. The CV tests were performed in 0 to 0.45 V over 2000 cycles at 200 mV/s. A 76% increase in areal capacitance (C_a) was observed up to the 1000th cycle, after which the value stabilized. The C_a was determined to be 1500 mF/cm^2 at 10 mV/s. Scan rate experiments yielded a “b value” of 0.65, indicating mixed control in the system by both capacitive and faradaic processes. Charge/discharge behavior was further investigated using GCD at current densities ranging from 0.1 to 0.01 A/cm^2. Based on GCD data, the energy and power density values were calculated as 57.5 mWh/cm^2 and 3450 mW/cm^2 at 0.01 A/cm^2, respectively.

For cobalt boride studies, two distinct experimental approaches were employed. In the first approach, a cobalt substrate with 99.6% purity was borided using the CRTD-Bor process at 950 °C and 200 mA/cm^2 for 15 minutes. The resulting boride layer measured approximately 80 µm in thickness, and multiple cobalt boride phases were identified.

EPMA-WDX analysis confirmed the formation of a dual-phase boride layer with mapping analysis indicating the presence of Co_2B near the surface. CV tests revealed two oxidation and reduction peaks, supporting the existence of two dominant faradaic reactions. However, the current passing through the system remained low, resulting in an areal capacitance of 55 mF/cm^2 after 2000 cycles at 200 mV/s. The Nyquist plot indicated that, while there was no solution resistance limitation in the low-frequency region, impedance in the mid-frequency region restricted charge transfer or ion transport. In the second part of the study, cobalt/cobalt boride (Co/Co_xB) composite powders were synthesized using an environmentally friendly, rapid, and cost-effective molten salt electrolysis process with oxide-based electrolytes of $Na_2B_4O_7$ and $Co(OH)_2$. Co-deposition of Co and B was achieved on a low-carbon steel substrate at 900 °C for 1 hour at current densities of 200 and 600 mA/cm^2. The growth mechanism, composition, and morphology of the composite structures were examined using XRD, SEM, and TEM. At 200 mA/cm^2, the powders consisted of metallic Co and Co_3B, while at 600 mA/cm^2, multi-phase borides such as CoB, Co_2B, and Co_3B were detected, with a trace amount of metallic Co. Electrochemical properties were evaluated using CV, GCD, and linear sweep voltammetry (LSV) to assess the electrodes' suitability for supercapacitor applications. The boride-rich electrode exhibited superior performance, achieving an areal capacitance of 4180 mF/cm^2, an energy density of 78 mWh/cm^2, and a power density of 2800 mW/cm^2. In comparison, the Co_3B/Co electrode demonstrated 2900 mF/cm^2, 48 mWh/cm^2, and 2300 mW/cm^2, respectively. The Trasatti approach indicated that both electrodes possess a mixed capacitive-diffusive charge storage mechanism. LSV experiments demonstrated enhanced catalytic behavior for the boride-rich Co/Co_xB electrode. These findings suggest that the multiphase, boron-rich Co/Co_xB composite significantly enhances electrochemical performance, underscoring its potential as a high-performance supercapacitor electrode.

All in all, the nickel and cobalt boride electrodes in several geometries and compositions have been produced via green and fast method of oxide electrolyte based molten salt electrolysis and analysed comprehensively. Results have demonstrated that Ni and Co-boride based electrodes are the promising candidates for supercapacitor applications with high energy and power density along with long service performance.

NİKEL VE KOBALT BORÜR ESASLI YÜKSEK KAPASİTELİ ELEKTROTLAR: ÜRETİMİ, KARAKTERİZASYONU VE SÜPERKAPASİTÖR PERFORMANSI

ÖZET

Fosil yakıtların yaygın tüketimi, küresel nüfus artışıyla birleşince, doğal kaynakların tükenmesine ve önemli çevresel kirliliğe yol açmıştır. Sonuç olarak, küresel çevresel zorlukların üstesinden gelmek için teknolojik gelişmelerle birlikte yeşil ve sürdürülebilir enerjiye olan talep artmıştır. Yenilenebilir enerji kaynaklarına artan talep, verimli enerji depolama cihazlarına acil bir ihtiyaç doğurmuştur. Şarj edilebilir piller, başlıca elektrokimyasal enerji depolama cihazı türü olup, elektrikli ve hibrit araçlarda, dizüstü bilgisayarlarda, telefonlarda ve tıbbi cihazlarda yaygın olarak kullanılmaktadır. Bununla birlikte, düşük güç yoğunluğu, sınırlı kapasite ve kısa şarj ömrü gibi sınırlamalar, alternatif çözümler arayışını başlatmıştır. Yüksek güç yoğunluğu, hızlı şarj ve deşarj oranları ve uzun hizmet ömrü ile öne çıkan süperkapasitörler, gelecek nesil enerji depolama bileşenleri olarak kabul edilmektedir.

Borürler, benzersiz elektronik yapıları nedeniyle oldukça ilgi görmektedir. Borun elektron eksikliği özelliği, çeşitli bağ konfigürasyonlarının ve farklı stokiyometrilere sahip kararlı borür fazlarının oluşumunu mümkün kılar. Bu yapısal özellik, faradayik reaksiyonların çeşitliliğini artırarak elektrot performansını iyileştirir. Ek olarak, bor, diğer birçok metal olmayan elementten daha yüksek elektriksel iletkenliğe sahiptir; bu da daha yüksek alansal ve özgül kapasitans elde edilmesini kolaylaştırır. Borürler arasında, geçiş metali borürleri süperkapasitör uygulamaları için dikkat çekici özelliklere sahiptir. Çoklu oksidasyon durumları, elektrotların çevrim ömrünü artırdığı için onları psödokapasitör elektrotları için ideal kılmakta olup nikel ve kobalt, elektrokatalitik özellikleri nedeniyle diğer geçiş metalleri arasında öne çıkmaktadır. Ni ve Co'nun üstün özelliklerinin B ile birleşimi, uzun hizmet ömrüne sahip yüksek enerji ve güç yoğunluğu gösteren süperkapasitör elektrotları elde edilmesini sağlar.

Literatürde metal borürlerin üretimi için çok sayıda yöntem bildirilmiştir. Endüstriyel gelişmelere bağlı olarak, çeşitli teknikler yüksek saflıkta borürlerin seri üretimini mümkün kılmaktadır. Bunlar arasında metal oksitlerden borotermal, karbotermik ve metalotermik indirgeme, mekanokimyasal sentez, kimyasal indirgeme temelli çöktürme, hidrotermal veya solvotermal sentez ve ince film kaplama yer almaktadır. Yaygın kullanımlarına rağmen, bu yöntemler genellikle homojen ve yüksek saflıkta malzemelerin üretimini engellemekte olup çevre ve insan sağlığı açısından riskler oluşturmaktadır. Buna karşılık, oksit elektrolit esaslı ergimiş tuz elektrolizi, çevre dostu, uygun maliyetli ve hızlı bir üretim tekniği olarak ortaya çıkmıştır. Bu yaklaşım pahalı ekipman gerektirmez, zehirli gazlar veya katı atık üretmez ve çeşitli mühendislik uygulamaları için yenilikçi bir potansiyel sunar. Sonuç olarak, ergimiş tuz elektrolizi, maliyetli bileşenlerden ve atık üretiminden kaçınan ekonomik ve verimli bir üretim yöntemi olarak ön plana çıkmaktadır.

Bu tez çalışması, süperkapasitör uygulamaları için özgün bir yöntem olan oksitli elektrolit esaslı ergimiş tuz elektolizi tekniği kullanılarak üretilen nikel ve kobalt borür elektrotlarının sentezini, yapısal ve elektrokimyasal özelliklerinin kapsamlı bir şekilde incelenmesini kapsamaktadır. Düz ve köpük olmak üzere iki farklı geometriye sahip saf nikel altlıklar, katodik indirgeme ve termal difüzyon esaslı borlama (CRTD-Bor) yoluyla boraks esaslı bir elektrolit içinde borlanmaya tabi tutulmuştur. Nikel matrisi içinde yüzeyden içe doğru düzenlenmiş nikel borür fazlarının, özellikle NiB, Ni_4B_3 ve Ni_2B'nin oluşumu, X-ışını kırınımı (XRD) ve elektron prob mikroanalizörü (EPMA) ile donatılmış taramalı elektron mikroskobu (SEM) ile doğrulanmıştır. Elde edilen elektrotların elektrokimyasal özellikleri, çevrimsel voltametri (CV), galvanostatik şarj-deşarj (GCD) ve elektrokimyasal empedans spektroskopisi (EIS) kullanılarak değerlendirilmiştir. Elektrokimyasal testler neticesinde; 10 mV/s tarama hızında 2000 CV döngüsünden sonra, nikel borür elektrotların alansal kapasite değerleri düz numune için 478 mF/cm^2 ve köpük numune için 1385 mF/cm^2 olarak hesaplanmıştır. Reaksiyon kinetiği, Trasatti yaklaşımında tanımlandığı gibi karma kontrollü bir modeli izlemektedir. Kapasitif katkı (C_o), köpük elektrot için hesaplanan %40,6'ya kıyasla düz elektrotta %71 ile önemli ölçüde daha yüksek bulunmuştur. Faradaik reaksiyonların altında yatan mekanizmalar, CV deneylerinden önce ve sonra X-ışını fotoelektron spektroskopisi (XPS) ve Fourier Dönüşümlü Kızılötesi Spektroskopisi (FTIR) kullanılarak incelenmiş olup sonuçlar, mekanizmanın elektrokimyasal test sırasında nikel borür yüzeylerindeki kusurlu bölgelerde oksijen doygunluğundan kaynaklanan Ni-O bağlarının oluşumuyla ilişkili olduğunu göstermektedir. Ek olarak, elektrot geometrisinin elektrokimyasal davranış ve performans üzerindeki etkisi sistematik olarak incelenmiş olup, gözenekli bir yapının daha fazla enerji depolamayı kolaylaştırdığını ve hızlı şarj-deşarj davranışını geliştirdiğini, böylece elektrotların güç yoğunluğunu artırdığını ortaya çıkarmıştır.

Ek olarak, CRTD-Bor yöntemiyle Ni-borür tozları sentezlenmiş ve ardından kapsamlı yapısal ve elektrokimyasal karakterizasyon yapılmıştır. Ağ geometrisine sahip nikel numuneler, 1000 °C ve 200 mA/cm^2 akım yoğunluğunda 2 saat boyunca tam kesit borlama işlemine tabi tutulup, daha sonra faz homojenizasyonunu sağlamak için 1 saat boyunca ergimiş elektrolitte bekletilmiştir. Borlama işleminden sonra, tamamen bor difüzyonu yapılmış numuneler bilyalı değirmen kullanılarak öğütülmüş ve sonrasında soğuk pres ile disk şekli verilmiştir. Ni-borür tozlarının yapısal karakterizasyonu XRD, SEM ve TEM kullanılarak gerçekleştirilmiştir. Analiz sonuçları, tozların NiB, Ni_4B_3, Ni_2B ve Ni_3B'den oluştuğunu ve Ni_4B_3'ün baskın faz olduğunu ortaya koymuştur. Üretilen elektrotların elektrokimyasal davranışı, standart üç elektrotlu bir sistemde CV ve GCD teknikleri kullanılarak değerlendirilmiştir. CV deneyleri, 200 mV/s hızında 2000 döngü boyunca 0 ila 0,45 V potansiyel aralığında gerçekleştirilmiş, alansal kapasitede (C_a) 1000. döngüye kadar %76'lık bir artış gözlemlenmiştir ve C_a, değeri 10 mV/s tarama hızında 1500 mF/cm^2 olarak belirlenmiştir. Tarama hızı deneyleri, hem kapasitif hem de faradayik süreçlerle karışık kontrolü gösteren 0,65'lik bir b değeri vermiştir. Şarj/deşarj davranışı, 0,1 ila 0,01 A/cm^2 arasında değişen akım yoğunluklarında GCD kullanılarak daha ayrıntılı olarak incelenmiş, ve GCD verilerine dayanarak, enerji ve güç yoğunluğu değerleri 0,01 A/cm^2'de sırasıyla 57,5 mWh/cm^2 ve 3450 mW/cm^2 olarak hesaplanmıştır.

Kobalt borür çalışmaları için iki farklı deneysel yaklaşım kullanılmıştır. Birinci yaklaşımda, %99,6 saflıkta bir kobalt altlık, 950 °C'de ve 200 mA/cm^2 akım yoğunluğunda 15 dakika boyunca CRTD-Bor işlemi kullanılarak borlanmıştır. Elde edilen borür tabakasının birden fazla kobalt borür fazı içerdiği belirlenmiştir. EPMA-

WDX analizi, yüzeyde yaklaşık 80 µm kalınlığında çift fazlı bir borür tabakasının oluşumunu doğrulamış ve haritalama analizi, yüzeye yakın bölgede Co_2B varlığını göstermiştir. CV analizi, iki baskın faradayik reaksiyonun varlığını destekleyen iki oksidasyon ve redüksiyon pik noktası ortaya koymuştur. Bununla birlikte, sistemden geçen akım düşük kalmış ve 200 mV/s hızında 2000 döngüden sonra 55 mF/cm^2'lik bir alansal kapasite elde edilmiştir. Nyquist grafiği, düşük frekans bölgesinde çözelti direnci sınırlaması olmamasına rağmen, orta frekans bölgesindeki empedansın yük transferini veya iyon taşınmasını kısıtladığını göstermiştir. Çalışmanın ikinci bölümünde, $Na_2B_4O_7$ ve $Co(OH)_2$ oksit bazlı elektrolitler kullanılarak, çevre dostu, hızlı ve uygun maliyetli bir ergimiş tuz elektroliz işlemiyle kobalt/kobalt borür (Co/Co_xB) kompozit tozları sentezlenmiştir. Co ve B'nin eş zamanlı birikimi, düşük karbonlu çelik bir altlık üzerinde 900 °C'de 1 saat boyunca 200 ve 600 mA/cm^2 akım yoğunluklarında gerçekleştirilmiştir. Kompozit yapıların büyüme mekanizması, bileşimi ve morfolojisi, XRD, SEM ve TEM kullanılarak incelenmiştir. 200 mA/cm^2'de tozlar metalik Co ve Co_3B'den oluşurken, 600 mA/cm^2'de eser miktarda metalik Co ile birlikte CoB, Co_2B ve Co_3B gibi çok fazlı borürler tespit edilmiştir. Elektrotların süperkapasitör uygulamaları için uygunluğunu değerlendirmek amacıyla elektrokimyasal özellikler CV, GCD ve doğrusal tarama voltametrisi (LSV) kullanılarak incelenmiştir. Borürce zengin elektrot, 4180 mF/cm^2'lik bir alansal kapasite, 78 mWh/cm^2'lik bir enerji yoğunluğu ve 2,8 mW/cm^2'lik bir güç yoğunluğu ile üstün performans sergilemiştir. Buna karşılık, Co_3B/Co elektrotu sırasıyla 2900 mF/cm^2, 48 mWh/cm^2 ve 2,3 mW/cm^2 değerlerini göstermiştir. Trasatti yaklaşımı ile, her iki elektrotun da karma kapasitif-difüzif bir yük depolama mekanizmasına sahip olduğu belirlenmiştir. LSV deneyleri ise, borürce zengin Co/Co_xB elektrotu için gelişmiş katalitik davranış sergilediğini ortaya çıkarmıştır. Bu bulgular, çok fazlı, borca zengin Co/Co_xB kompozitinin elektrokimyasal performansı önemli ölçüde artırdığını ve yüksek performanslı bir süperkapasitör elektrotu olarak potansiyelini vurguladığını göstermektedir.

Özetle, çeşitli geometri ve bileşimlerdeki nikel ve kobalt borür elektrotlar, oksit elektrolit bazlı ergimiş tuz elektrolizi ile çevresel ve hızlı bir şekilde üretilmiş ve kapsamlı olarak analiz edilmiştir. Sonuçlar, Ni ve Co borür bazlı elektrotların, yüksek enerji ve güç yoğunluğunun yanı sıra uzun hizmet ömrü performansı ile süperkapasitör uygulamaları için umut vadeden adaylar olduğunu göstermiştir.

1. INTRODUCTION

Increasing environmental pollution and the depletion of limited resources have increased the demand for high-tech, green, and sustainable energy conversion/storage materials. In this context, battery research has intensified, and electrodes and devices with high energy density have been developed [1–4]. However, the low power density and short service life of batteries have prompted the search for alternative storage devices. Supercapacitors are among the new generation of storage materials with relatively high energy and power density values [5].

Supercapacitors are among the new generation of storage materials with relatively high energy and power density values [5–7]. Supercapacitors are divided into two subgroups: electric double-layer capacitors (EDLC) and pseudocapacitors. While carbon-based materials (carbon nanotubes, graphene, activated carbon, etc.) are used as electrodes in EDLCs, transition metal compounds (oxides, phosphides, sulfides, selenides, borides, etc.) and conductive polymers are used as pseudo-capacitor electrodes [8–10]. Pseudocapacitors exhibit higher specific and/or areal capacitance compared to EDLCs, but their low electrical conductivity affects electrode performance. To improve this, these electrode materials are combined with carbon-based materials as asymmetric supercapacitors, providing high capacitance and improved charge/discharge behavior [11].

Among transition metal compounds, borides are emerging materials with superior metallic properties and, consequently, relatively higher electrical conductivity, resulting in better specific and/or areal capacitances [12]. For example, Ni and Co oxides exhibit pseudo-capacitance due to redox reactions, but their low conductivity limits their capacitive behavior. On the other hand, Ni and Co borides exhibit outstanding performance with fast charge-discharge cycles and increased capacities [13,14]. The reason for these differences observed in both Ni and Co compounds is the metallic properties of borides arising from mixed bond types along with interatomic interactions (e.g., metallic bonds in M-M, ionic M-B bonds, and strong covalent bonds between M-B and B-B due to electron deficiency in boron atoms where

M represents the metal) [15,16]. This bond diversity creates numerous structures with various stoichiometries and electronic configurations (i.e., MxBy; x, y ≥1), imparting superior properties.

In other respects, Ni and Co borides are distinguished from other transition borides due to their high electrical conductivity, catalytic nature, and chemical stability; which facilitates fast charge/discharge cycles and more active sites (resulting in increased energy density and improved energy transfer efficiency through fast reversible redox reactions at the electrolyte/electrode interfaces) and ensures chemical integrity (contributing to a longer cycle life) [11,17]. Furthermore, high power densities enable rapid energy storage/release, and cost-effectiveness makes them an attractive candidate for the supercapacitor sector [18,19]. In the open literature, Ni and Co compounds have been extensively investigated as supercapacitor materials [20–27], but the capacity of pure Ni and Co borides has been examined in only one publication [2] to mitigate bulk structural behavior. Other relevant studies mostly concern Ni and Co boride-based composites or amorphous electrodes.

In supercapacitor production, in addition to the electrode material, the structural porosity of the electrode is also quite critical [28]. High porosity increases the surface area, leading to more active regions and, consequently, enabling faster charge/discharge cycles, thereby improving energy storage capacity [2,29].

In this thesis study, the focus was the production and characterization of flat and foam shape Ni-borides together with the porous disc Ni-boride electrodes as well as flat shape and porous disc shape Co-borides. A patented molten salt electrolysis technique [30,31] was preferred for the synthesis of these borides. This boride production method involves the formation of borides on the substrate metal within a short processing time, without threatening the environment or human health, through the simultaneous diffusion of reduced boron atoms across the surface [30]. After electrolysis, the structural and electrochemical properties of the produced samples were systematically investigated using advanced characterization technique.

2. LITERATURE REVIEW

2.1 History and Development of Electrochemical Energy Storage Devices

The origins of modern electrochemical energy storage date back to the 18th century, when Benjamin Franklin used the term “battery” to describe his electrical storage device [32]. In 1800, Alessandro Volta developed the voltaic battery, which produced a continuous current using alternating zinc and copper plates immersed in a salt solution. This invention facilitated important technological advances such as the development of the telegraph and early communication systems, and is widely recognized as a fundamental development in battery technology [33]. Throughout the 19th century, various primary battery designs were introduced, and the Daniell cell emerged in the 1830s due to its improved stability and reliability as a voltage source [34]. The advent of rechargeable batteries occurred in 1859 with Gaston Planté's invention of the lead-acid battery. Despite its relatively low energy density, the lead-acid battery could provide high current and, being rechargeable, became the standard for automotive and uninterruptible power systems throughout the 20th century [35]. Later, nickel-cadmium (Ni-Cd) and nickel-iron (Ni-Fe) batteries were introduced in the 1890s and 1900s, respectively, and became an integral part of industrial applications and portable electronic devices [36].

In the second half of the 20th century, rising energy needs and the popularity of portable electronics and later electric vehicles drove the development of new battery technologies with higher energy density. Research in the 1970s and 1980s on lithium and transition metal oxide compounds laid the groundwork for today’s lithium-ion batteries [37]. Key researchers like Whittingham, Goodenough, Yazami, and Yoshino helped advance these studies, leading to Sony’s launch of the first commercial lithium-ion battery in 1991. This was a major milestone in energy storage for both portable devices and electric vehicles [38]. As electrochemical energy storage developed, there was also a need for solutions that could deliver high power, quick charge and discharge, and long lifespans. This led to the creation of devices now called supercapacitors or ultracapacitors [39]. In 1957, H. I. Becker at General Electric filed a patent showing how an electric double layer at the electrode-electrolyte interface could store energy [40]. In the 1960s, Standard Oil of Ohio (SOHIO) produced the first industrial carbon-based double-layer capacitors [41]. In the 1970s and 1980s, Brian E. Conway and his team, especially through work on RuO_2-based systems, explained the idea of pseudocapacitance and clarified the difference between battery-like and capacitive processes [42]. The histrorical development of energy storage devices is demonstrated in Figure 2.1.

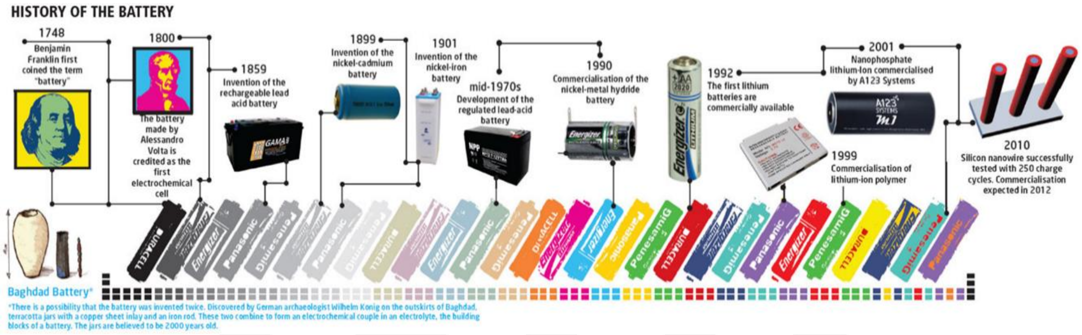

Figure 2.1 : Historical development of energy storage devices [43].

As the world relies less on fossil fuels and adds more renewable energy sources like solar and wind to the grid, energy storage has become important for not just portable devices but also for large-scale power systems, electric vehicles, and industry. Alongside lithium-ion batteries, other technologies such as sodium-ion batteries, metal-air systems, hydrogen storage, supercapacitors, and hybrid capacitors are becoming more popular, especially where high power and long life are needed [44]. Thanks to progress in materials science, researchers are now focusing on transition metal oxides, sulfides, phosphates, and especially transition metal borides, which have high electrical conductivity and chemical stability, as promising new electrode materials.

2.2 Types of Electrochemical Energy Storage Devices

Electrochemical energy storage devices are mainly categorized into four groups as batteries, capacitors, fuel cells and supercapacitors [45,46]. To compare energy storage technologies by energy density (Wh/kg or Wh/cm^2) and power density (W/kg or W/cm^2), researchers often use the Ragone diagram given in Figure 2.2, introduced by David V. Ragone in the late 1960s [47]. This diagram helps compare batteries, supercapacitors, fuel cells, and other systems on the same scale. Batteries usually provide high energy density but lower power density, while supercapacitors deliver very high power and long cycle life but lower energy density. The Ragone diagram is also a key tool for designing hybrid energy storage systems, such as battery-supercapacitor combinations [48].

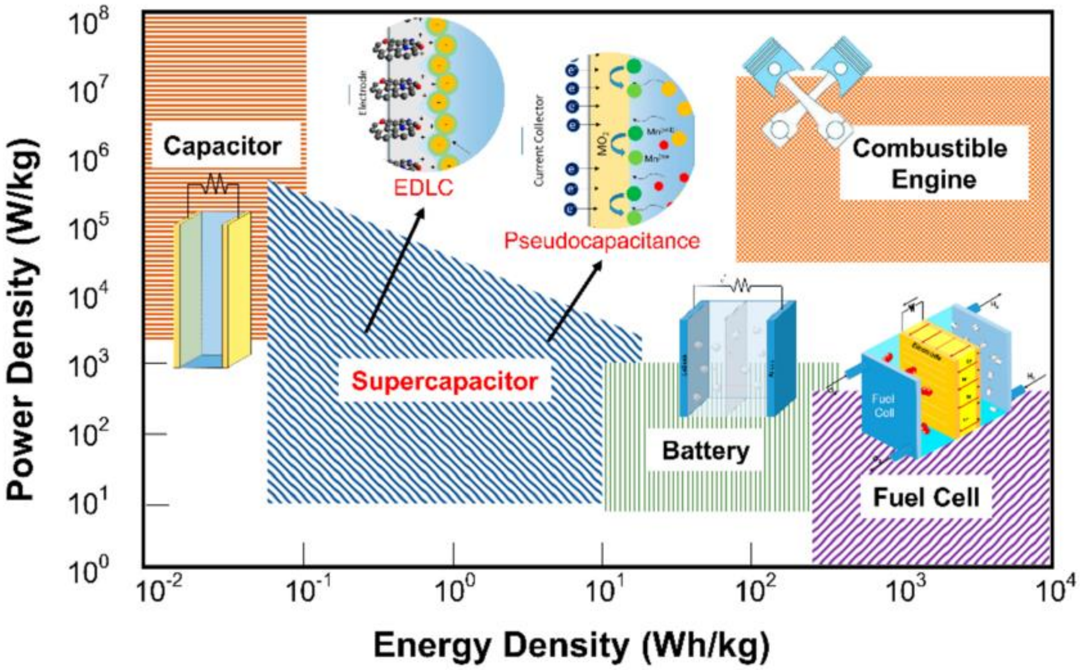

Figure 2.2 : The comparison of energy and power densities of energy storage devices [48].

2.2.1 Batteries

Batteries are independent units that store chemical energy and convert it directly into electrical energy to power various applications on demand. Batteries are divided into two general classes: Primary batteries (zinc-carbon, alkaline-manganese, lithium primer cells), which are discharged once and then discarded; secondary (lead acid, Ni-Cd, Ni-MH, Li-ion $LiFePO_4$, $LiNiMnCoO_2$ (NMc) rechargeable batteries, which can be discharged by reversing the current through the cell and then restored to their original state [6]. A battery uses two different metals (electrodes) and an electrolyte to create a potential difference; the cathode is the negative terminal, while the anode is the positive terminal (Figure 2.3) [49].

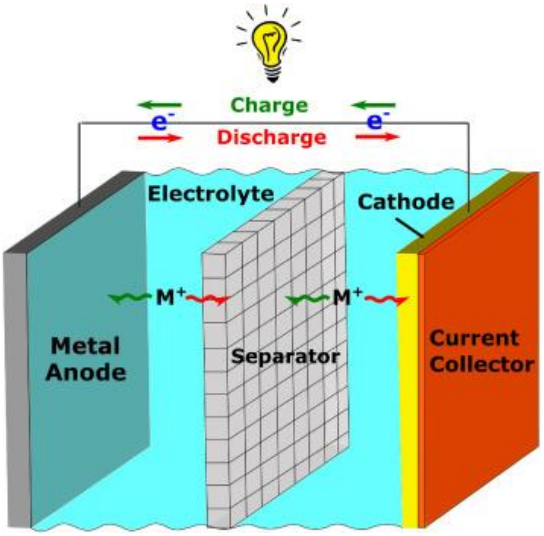

Figure 2.3 : Schematic illustration of a battery working mechanism [50].

2.2.2 Fuel cells

Fuel cells are instruments that transform chemical energy straight into electrical energy via the electrochemical interaction of a compatible fuel (commonly hydrogen) and an oxidizer (typically oxygen or air). In the discharge process, the fuel undergoes oxidation at the anode, while the oxidizer experiences reduction at the cathode; electrons travel through the external circuit to the load, and ions move through the electrolyte to sustain charge balance [51,52]. The working mechanism of fuel cells is shown in Figure 2.4.

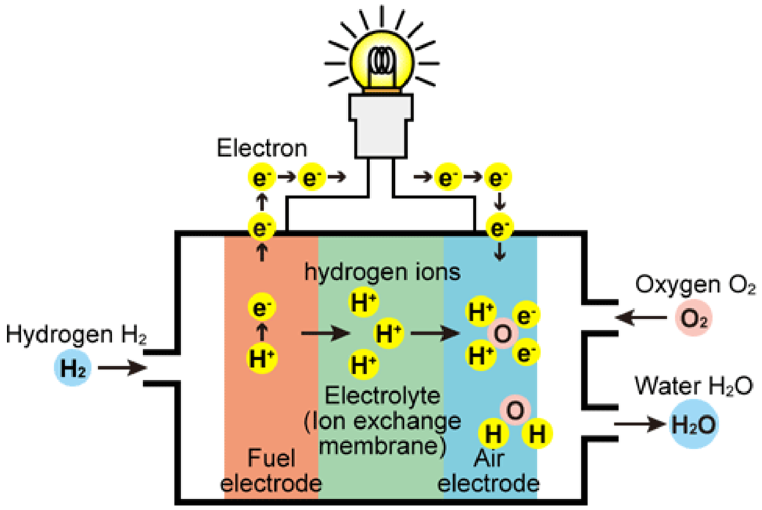

Figure 2.4 : Schematic illustration of a fuel cell working mechanism [53].

2.2.3 Capacitors

Capacitors are electrical components that store energy in the electric field between two charged surfaces. This is similar to how a raised mass stores potential energy in a gravitational field [54]. A typical capacitor has two conductive plates separated by a dielectric, which is an insulating material like air, plastic, or Teflon. Capacitors can charge and discharge faster than other energy storage devices, making them useful for handling the unpredictable nature of renewable energy sources such as wind and solar. They also help with peak shaving, frequency regulation, and smart power management in the electrical grid, which improves efficiency and supports energy savings and emission reductions. As electronics have developed, capacitors have evolved from simple designs using air, mica, or paper dielectrics to more advanced types like ceramic and electrolytic capacitors. New dielectric materials, especially organic ones, and better manufacturing methods have made capacitors smaller and improved their performance. Figure 2.5 shows how capacitors work [55].

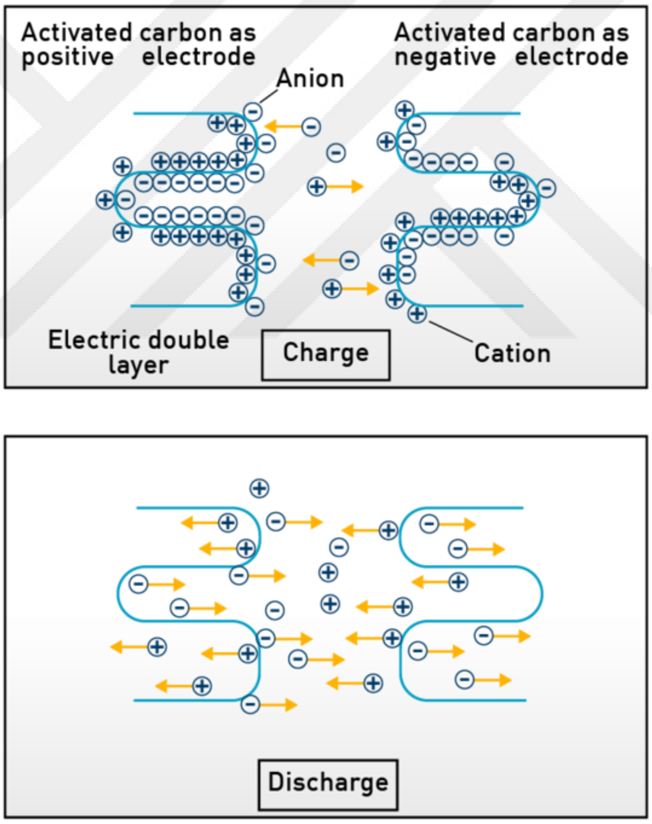

Figure 2.5 : The working mechanism of capacitors [56].

2.2.4 Supercapacitors

A supercapacitor is a type of capacitor specifically made for greater energy storage compared to traditional capacitors. Supercapacitors demonstrate much superior properties compared to other energy storage devices due to their high-power density, fast charging/discharging rate, and long service life, and are considered the materials of the future [57,58]. Supercapacitors are a group of energy storage devices that stand out not only because of their superior electrical properties but also because they do not cause waste problems or pose environmental threats, unlike batteries [8,58]. As seen in Figure 2.2, supercapacitors act as a bridge between capacitors and batteries within energy storage devices, compensating for the low power density of batteries and the low energy density of commercial capacitors [2,58] , enable their use in hybrid cars, energy harvesting systems, and smartphones and also are required in metros and trains where sudden stops and starts are needed [59].

When examining the estimated revenue of the global supercapacitor market by year (Figure 2.6a), this market is expected to grow by approximately 30% by 2025, reaching US$8.3 billion. This growth observed in the market from 2014 to the present is based on demand, particularly in the automotive sector, for regenerative braking systems and start-stop systems aimed at reducing fuel consumption. As shown in Figure 2.6b, the automotive and transportation sector dominates the supercapacitor market. The automotive and transportation sector has been among the most important sectors in the exponential growth of the supercapacitor market from the past to the present. The automotive sector continues to grow, and the supercapacitor market is expected to reach $2.7 billion by 2026. When examining the regional market shares of supercapacitors (Figure 2.6c), Asian countries play a significant role in the sector, with China in particular taking a leading position [60]. With increasing global awareness, efforts to reduce and eliminate CO_2 emissions, particularly in the automotive sector, have been initiated as a result of the threats posed by greenhouse gases and climate change. This situation has played a significant role in the development of electric and hybrid vehicles. Parallel to the development of these vehicles, the need for advanced energy storage devices has increased, and research and development efforts into the use of supercapacitors have rapidly expanded. Thanks to their high-power density, supercapacitors have enabled braking systems to achieve extremely fast stopping and acceleration capabilities. This feature is particularly prominent in metro trains and is in high demand due to the evolving capabilities of supercapacitors [60,61].

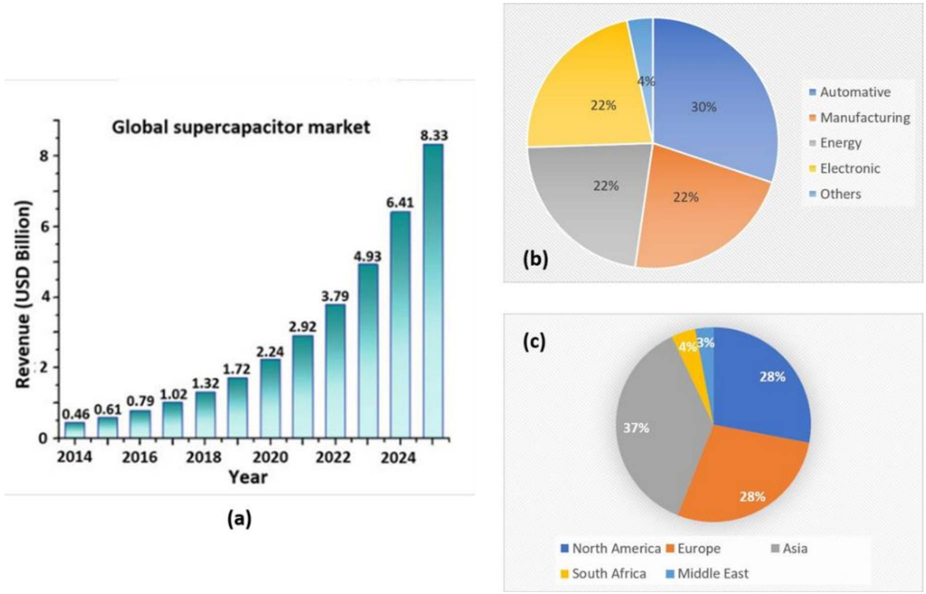

Figure 2.6 : a) The global supercapacitor market b) application areas, c) the production of supercapacitors according to regions [60].

When examining the historical development of supercapacitors (Figure 2.7), it is noteworthy that scientists have not only focused on generating electricity but also on storing the electrical energy they produce. The storability of energy was discovered by chance in 1745 at Leiden University, and the device called the Leyden jar is considered the first capacitor in history [62]. Subsequently, the formation of an electric double layer through electrostatic charging at the interface between two oppositely charged electrodes and an electrolyte was discovered by Helmholtz in 1879. This discovery was developed by Gouy and Chapman, and in 1924, Stern combined the Helmholtz model with the Gouy-Chapman model to explain the formation of the electric double layer in detail [63]. Commercialization followed the scientific developments of electric double-layer capacitors, and supercapacitor devices, patented in 1957, went into mass production in 1978. Supercapacitors did not remain limited to the charge transfer principle based solely on electrical polarization. Subsequently, they evolved into forms called pseudocapacitors, which have higher energy and power density as a result of chemical reactions occurring at the electrode and electrolyte interface based on Faraday's equations (1989). Pseudocapacitors were later combined with capacitors based on the formation of an electric double layer to produce hybrid supercapacitors, which are still being developed today [58]. The historical development of supercapacitors is demonstrated in Figure 2.7.

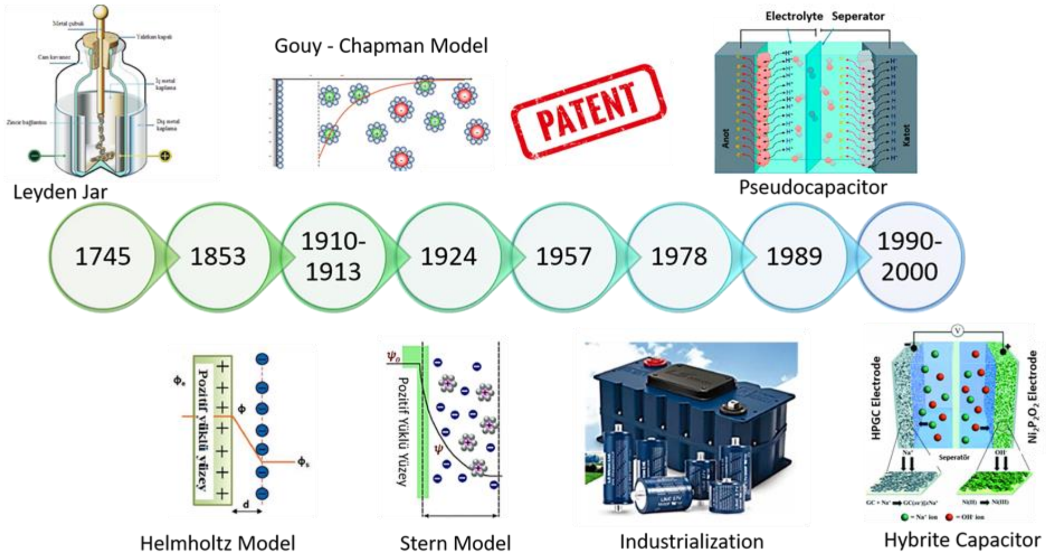

Figure 2.7 : Historical development of supercapacitors [64].

Supercapacitors (SC) can be categorized into three groups; electrical double layer capacitors (EDLCs), pseudocapacitors and hybrid capacitors according to their energy storage mechanisms [64], as illustrated in Figure 2.8.

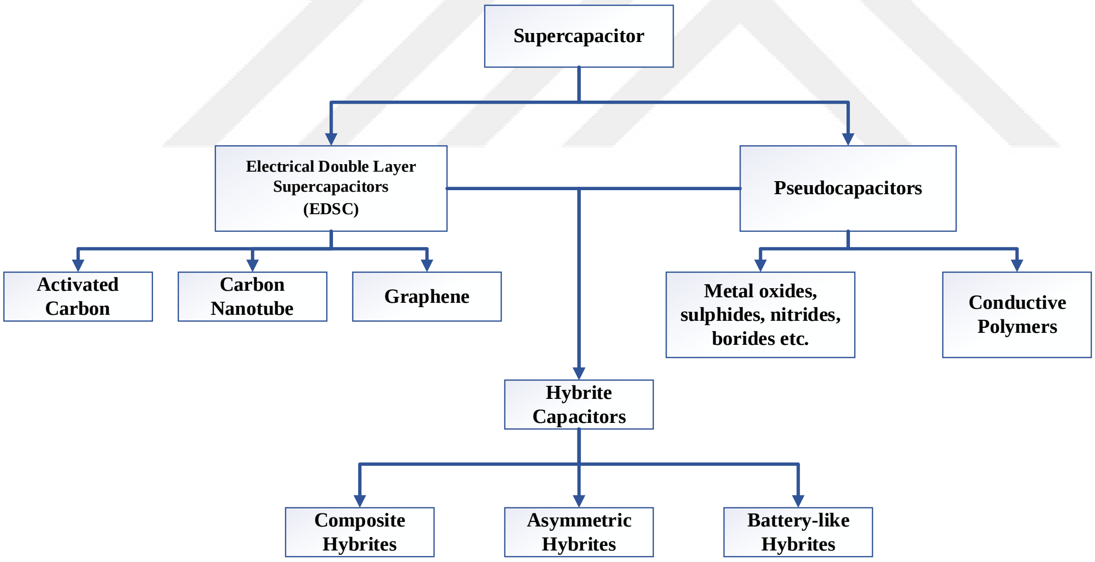

Figure 2.8 : Classification of supercapacitors.

EDLCs consist of an electrolyte, two carbon-based materials utilized as electrodes, and a separator. EDLCs can either store charges electrostatically or through a non-Faradaic process that does not involve charge transfer between the electrolyte and the electrode. When voltage is applied, charges do not accumulate on the surface of the electrode; instead, the opposing charges create a potential difference which causes the electrolyte ions to diffuse across the separator and into the pores of the oppositely charged electrode [52,65,66], as illustrated in Figure 2.9a. A double layer of charge is formed to prevent the recombination of ions in the electrodes. By increasing the specific surface area and decreasing the distance between electrodes, the double layer allows EDLCs to achieve high energy density [66].

Pseudocapacitors represent a category of supercapacitors that accumulate energy through quick and reversible faradaic (redox) reactions occurring on the electrode material surfaces [67] (Figure 2.9b). In contrast to EDLCs, which depend on the separation of electrostatic charges, pseudocapacitors attain greater capacitance and energy density by utilizing fast redox reactions [68]. The operating principle of pseudocapacitors is based on faradaic processes, which involve the transfer of electron charges between the electrode and the electrolyte, resulting in oxidation-reduction reactions. These reactions occur at or close to the surface of the electrode material and play a role in the total capacitance. Pseudocapacitors, unlike EDLCs, operate not only through physical but also chemical processes occurring at the electrodes. Thus, pseudocapacitors offer superior performance compared to EDLC-based capacitors in terms of energy and power density. The hybrid supercapacitors consist of two electrodes one is working as EDLC type and the other shows the pseudocapacitor behavior [69–71] shown in Figure 2.9c.

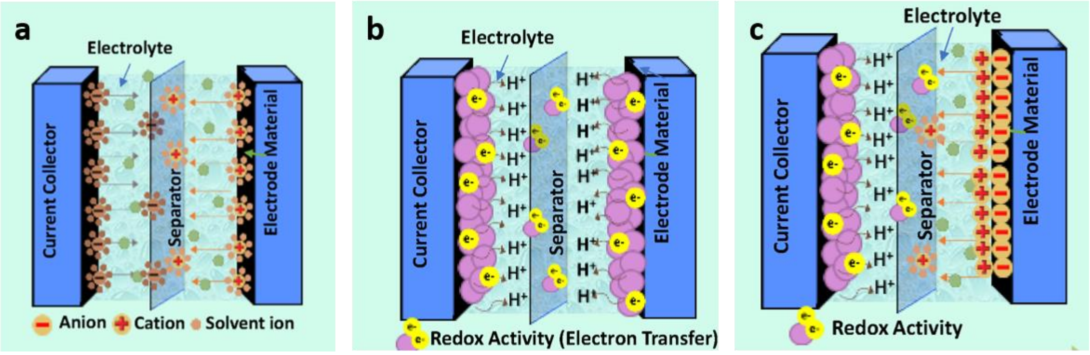

Figure 2.9 : Working mechanism of a) electrical double layers (EDLCs) b) pseudocapacitors, c) hybrid capacitors [72].

Figure 2.10 shows the CV and GCD behaviors varying according to energy storage mechanisms. In this context, in the top-ranked Type A (capacitive) behavior, charge storage occurs primarily at the surface via EDLC or rapid surface redox (pseudo-capacitance); therefore, the CV curves ideally take on a nearly rectangular form, and the GCD (discharge part) curves are approximately linear/triangular, showing that the potential changes with an almost constant slope over time. In the middle-ranked Type B (pseudo-capacitive-intercalation-dominant) systems, the entry and exit of ions into and out of the material (intercalation) is pronounced, and the CV curves deviate from the rectangle, exhibiting broad redox regions, while the GCD curves deviate from linearity. In the bottom-ranked Type C (Faradaic/battery-like) behavior, charge storage is controlled by pronounced phase transitions or slow faradaic reactions; discontinuous redox peaks are observed in the CV. In the GCD, a charge-discharge profile characteristic of batteries is formed [60,73].

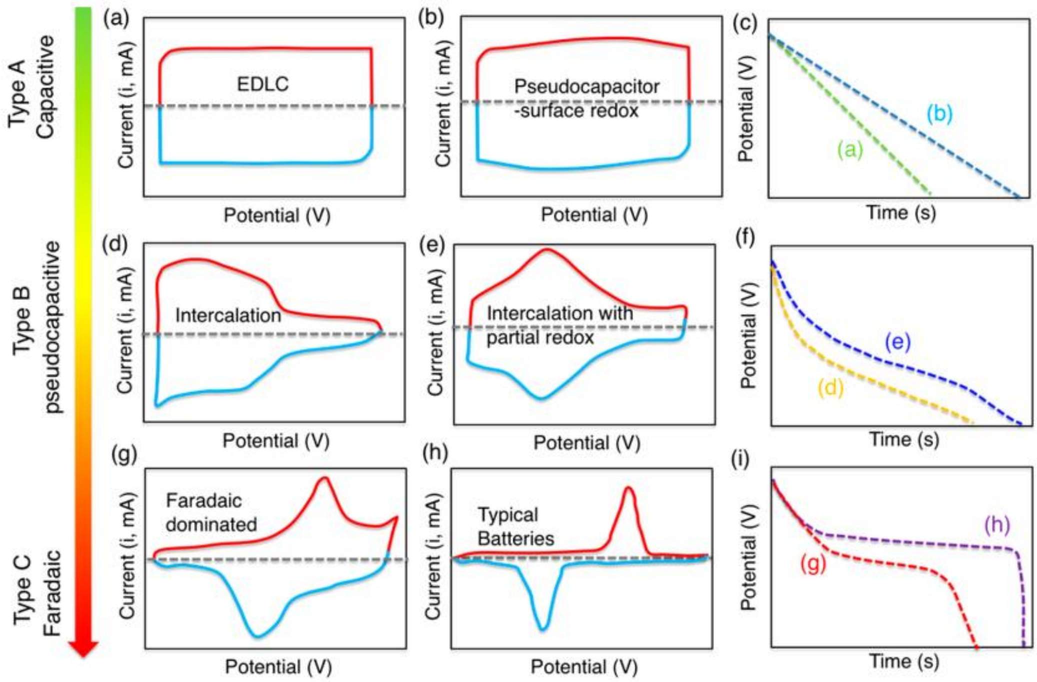

Figure 2.10 : The type of CV and GCD behavior of supercapacitors based on energy storage mechanism [73].

2.3 Electrode Material Selection in Supercapacitor Applications

While carbon-based materials (carbon nanotubes, graphene, activated carbon, etc.) are used as the electrode in EDLCs, transition metal compounds (oxides, phosphides, sulphides, selenides, borides, etc.) and conductive polymers are used as pseudocapacitor electrodes [61]. For a pseudocapacitor to exhibit high performance, the electrode material must have high conductivity, undergo rapid surface redox reactions, and maintain chemical stability over long cycles [9]. In this context, current conductive polymers (PANI, PPy, PTh, etc.), transition metal oxides (RuO_2, MnO_2, NiO, Co_3O_4, etc.), hydroxides ($Ni(OH)_2$, $Co(OH)_2$), sulfides (MoS_2, NiS, CoS, etc.), phosphides (NiP, CoP, FeP, etc.), nitrides (MnN) and borides (NiB, CoB, VB, MnB, etc.) are used as pseudocapacitive electrode materials [74–76].

Among supercapacitor electrode materials, transition metal compounds (TMCs) exhibit superior performance especially for energy density. Their multiple oxidation states enable TMCs to transfer multiple electrons and to extend the discharge time. This leads increament in capacitance performance since it results in rapid faradaic reactions [58]. Furthermore, transition metal compounds can store more energy due to reversible Faradaic reactions between the electrode and electrolyte ions, and thus exhibit higher capacitance than traditional carbon and conductive polymer based electrode materials [77,78]. Figure 2.11 shows the oxidation states of some transition metals. When these states are examined, it is seen that manganese is the metal with the most oxidation states, followed by iron, chromium, vanadium, cobalt and nickel with multiple oxidation states [79].

Ti	V	Cr	Mn	Fe	**Co**	**Ni**	Cu
3d^{2}4s^2 [Ar]	3d^{3}4s^2 [Ar]	3d^{5}4s^1 [Ar]	3d^{5}4s^2 [Ar]	3d^{6}4s^2 [Ar]	**3d^{7}4s^2** **[Ar]**	**3d^{8}4s^2** **[Ar]**	3d^{10}4s^2 [Ar]
+2	+2	+2	**+2**	**+2**	**+2**	**+2**	**+1**
+3	**+3**	**+3**	+3	**+3**	**+3**	+3	**+2**
+4	+4	+4	**+4**	+4	+4	+4	+3
	+5	+5	+5	+5	+5		
		+6	+6	+6			
			+7				

Figure 2.11 : Oxidation states of some transition metals [79].

For transition metals to be used as electrode materials, the number of valences they receive alone is not sufficient; their chemical stability also plays a significant role. As mentioned above, the existence of reversible Faradaic reactions is crucial for the production of a supercapacitor with high capacity and high energy performance. In this context, it is important that the electrode material exhibits continuous catalytic properties and does not passivate. The compound receiving the highest valence in the electrode material must be non-stoichiometric and exhibit labile (unstable) properties. In this case, Frost and Latimer diagrams, which demonstrate the stability of metals, are examined [79]. Figure 2.12 presents the Frost diagrams for metals with catalytic properties, such as nickel and cobalt, and those with the highest valence stoichiometric properties, such as titanium and chromium. Frost diagrams are plotted according to the Gibbs free energy of formation of the metal oxide compound, as opposed to the oxidation number of the metal forming it. In this context, the compounds of the transition metals nickel and cobalt, which have the highest valence 4+, have higher Gibbs free energies and exhibit non-stoichiometric properties. Therefore, since the formation of the highest valence compound is unstable during repeated Faradaic reactions, the resulting compound is decomposed, ensuring the continuity of the reactions. This, in turn, stores more energy and extends the life of the electrode material. On the other hand, when the Frost diagrams of titanium and chromium metals are examined, it is seen that the TiO_2 compound, in which titanium has the highest valence, and the $CrO4^{2-}$ compound, in which chromium has the highest valence, have lower Gibbs free energy values than the other compounds and are the most stable phases. This causes the surface of the electrode material made of these metals to become passive over time and its performance to decrease rapidly [80,81].

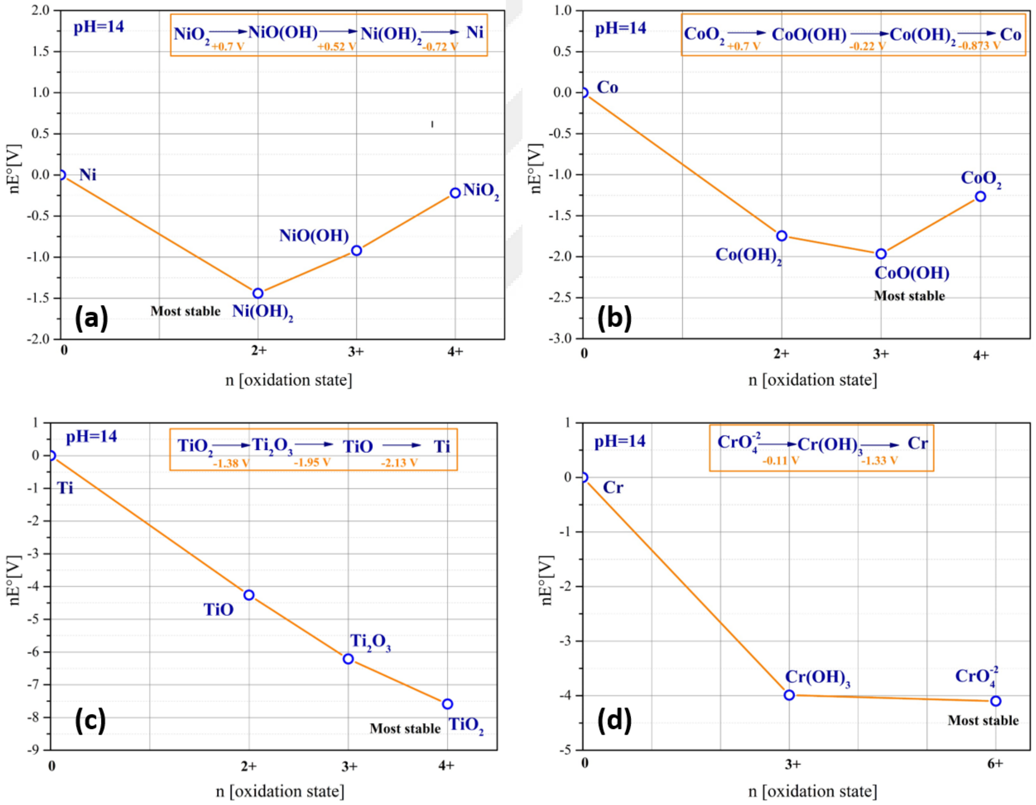

Figure 2.12 : The Frost diagrams of Ni, Co, Ti and Cr [80].

The situation observed in Frost diagrams is also revealed when Latimer diagrams are examined. Figure 2.13 shows the Latimer equations for the transition metals nickel, cobalt, titanium, and chromium, and the potential values required for the next oxidation step. The stability of the phase formed at the highest oxidation step can be determined by examining the formation potentials on the Latimer diagram. The formation potential of the highest valence phase of nickel in the Latimer diagram is

0.70 V, much higher than the formation potentials of its other compounds. This demonstrates that nickel is not passivated and that the faradaic reactions occurring at the electrode/electrolyte interface continue. Unlike cobalt, which exhibits the same properties, titanium and chromium show that the potential required for the formation of the highest valence field phases is lower than the others. Therefore, it is concluded that these phases can easily form, reach a stable phase in supercapacitor applications, and kinetically inhibit the system [81].

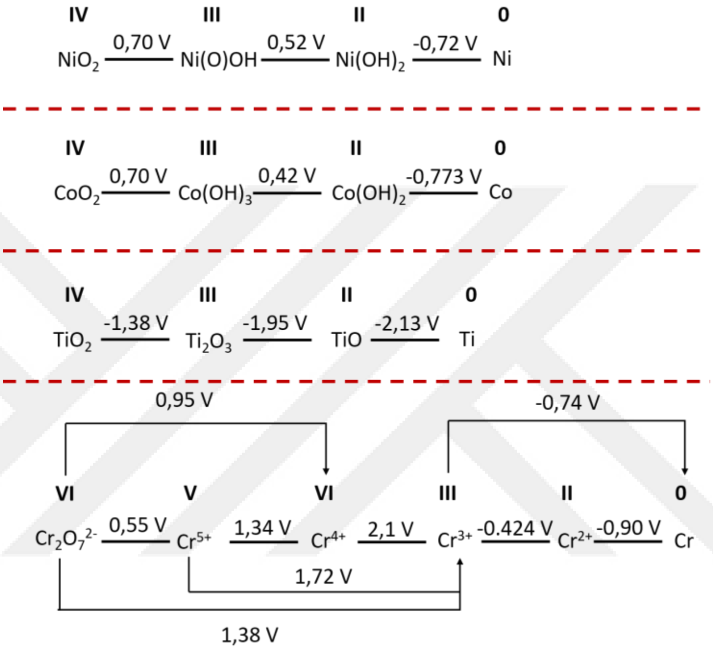

Figure 2.13 : Latimer diagrams of of Ni, Co, Ti and Cr [79].

Transition metal compounds including oxides, sulfides, phosphides, selenides, nitrides and borides are widely discussed in the open literature as the electrode materials for pseudocapacitors [12]. Among these, borides are attracting attention owing to their exclusive electronic structure. Due to the metallic properties of borides, which result from mixed bonding types such as metallic bonding in M-M, ionic M-B bonds, and strong covalent bonds between M-B and B-B, which are a consequence of the electron deficiency of boron atoms (where M represents the metal). Since boron exhibits better metallic properties than elements such as O, P, S, and N found in transition metal compounds, it increases the electrical conductivity of the compounds it forms, resulting in higher areal and specific capacity values [15,16]. This structural character enhances the assortment in faradic reactions, hence improves the electrode performance. Furthermore, compared to other non-metallic elements, boron has relatively higher electrical conductivity which contributes to attain higher areal/specific capacitance. Eventually, transition metal borides demonstrate superior electrochemical performance regards to other transition metal compounds.

2.4 Properties of Metal Borides

Boron is a non-metal element found in group IIIA of the periodic table, positioned after hydrogen, helium, lithium, and beryllium. It is categorized as a semi-metal and can also be considered a metalloid due to certain metallic characteristics it displays. Some elements might resemble the second element of the subsequent group more than the second element of their own group regarding physical and chemical properties. This occurrence is referred to as 'diagonal similarity'. Unlike the elements in group IIIA, boron has semiconductor properties and shares similarities with silicon and carbon concerning both physical and chemical characteristics. In English, boron is referred to as 'boron', derived from the root 'bor' combined with the suffix 'on', as borax deposits are reminiscent of carbon deposits [82,83].

Compounds formed by one or more metals with boron, possessing superior physical and chemical properties, are called metal borides. The ability of many different elements in the periodic table to form various boride compounds with boron has made it possible to use these compounds in different fields. Metal borides can be examined under two main headings: compounds containing only one type of metal atom in their molecule are called 'binary metal borides', while compounds containing at least two different metal atoms in their molecule are called 'terner metal borides' [83].

Metal borides are ceramic materials that stand out in advanced engineering applications due to their high melting points, high hardness and wear resistance resulting from strong covalent B-B and metal-boron bonds, superior chemical and thermal stability, and high electrical conductivity observed in many compositions [84,85]. Thanks to this versatile combination of properties, metal borides are widely used in cutting tools, mold surfaces, and protective coatings to provide tribological resistance [86]; in aerospace and energy systems for parts requiring high-temperature oxidation/erosion resistance [87]; and in components requiring structural stability under harsh conditions such as nuclear and space environments [88]. In electronics and energy storage, some transition metal borides are used as electrodes for electrocatalysis (HER/OER) batteries and supercapacitors due to their metallic conductivity and surface redox activity [1,2,89]. Rare earth borides, on the other hand, exhibit high performance in thermionic cathode and vacuum electronics technologies with their low work function and high emission stability [90]. Therefore, metal borides are considered a new generation of advanced technology materials due to their multifunctional properties. While some borides have a low number of boron molecules (e.g., M_5B), others contain a high number (e.g., MB_{66}). Therefore, their molecular structures do not conform to the rules for formulating conventional chemical formulas. A boride compound is considered boron-rich when the boron/metal ratio is 4 or higher; conversely, it is considered metal-rich when this ratio is low [83].

The high degree of covalent chemical bonding of metal borides can be expected to result from the low electronegativity of the boron element. This covalent bond structure gives metal borides many important properties. Metal borides, which are included in the group of refractory hard materials such as nitrides and carbides, have properties such as high temperature resistance, high melting point and high hardness thanks to their covalent bond structures [91] .

Metal borides, in terms of formula and molecular structure, are grouped into six main groups as monoborides (MB), diborides (MB_2), tetraborides (MB_4), hexaborides (MB_6), dodeborides (MB_{12}) and hectoborides (MB_{66}) [91,92]. The periodic table of possible elements that makes compound with boron and their properties shown in Figure 2.14.

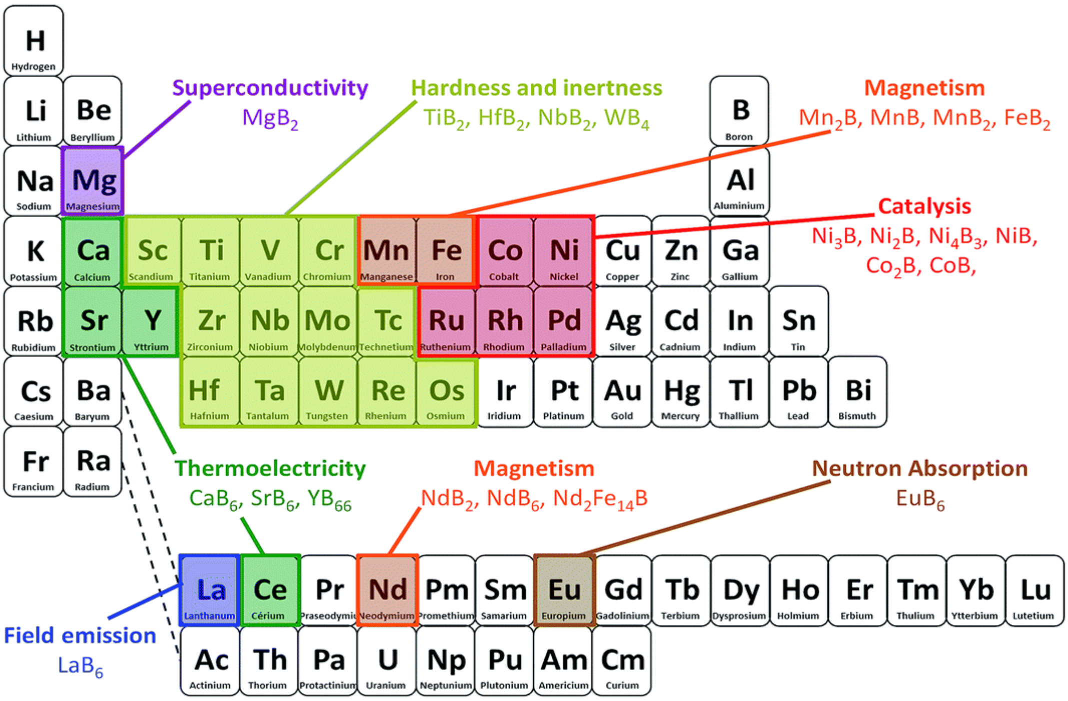

Figure 2.14 : Periodic table demonstrating the properties of some metal borides [93].

2.5 Production Methods for Transition Metal Borides

Various methods are used in the production of metal borides. Due to the high melting point of transition metal borides and the strong covalent bonds of their high boron-containing phases, most metal boride production methods require high temperatures [94]. Since, high temperatures involved, it is difficult to prepare metal borides in a homogeneous, single-phase form with high purity, and the subsequent purification process is also generally difficult [95]. Several pyrometallurgical and hydrometallurgical methods exist in the literature as follows [84];

- High-temperature solid state and borothermal routes
- Self-propagating high-temperature synthesis (SHS) and combustion methods
- Mechanochemical synthesis
- Chemical reduction-based precipitation method
- Hydrothermal and solvothermal synthesis
- Vapor phase and thin film deposition methods
- Molten salt electrolysis etc.

2.5.1 High temperature solid state and borothermal routes

These are solid-solid reactions controlled by a slow diffusion mechanism. The main advantage of borothermal reduction is the purity of the final powders produced and the potential to obtain these powders in a fine particle size. However, this method generally requires a pure boron source, which is more expensive than carbon, and necessitates a higher reaction temperature. Although it is the most suitable method for the industrial production of boride powders, large-scale production requires high amounts of boron and leads to rapid resource depletion [96]. The reaction occurs during borothermal synthesis given in equation 2.1.

$$MO_2 + 4B \rightarrow MB_2 + B_2O_2 \qquad (2.1)$$

2.5.2 Self-propagating high-temperature synthesis (SHS) and combustion methods

Self-propagating high-temperature synthesis, also known as combustion synthesis, is a simple method for synthesis of advanced ceramics and intermetallics. The principle of this method is triggering an enormously exothermic reaction to spontaneously start and propagate spontaneously in a wave-like manner over the reaction mixture. In order to ensue this event, the reaction should exhibit a high activation energy and produce extremely high heat.

With the SHS method, the production of refractory compounds (i.e. boride, nitride, silicide, hydride, carbide, sulfide, selenite, tellurite, and oxide), intermetallic materials such as aluminite, nickelite, germanite; superconducting materials; corrosion and wear resistant coatings; catalysts materials is carried out by using mixtures consisting any of the metal-metal, metal-nonmetal and nonmetal-nonmetal couples releasing significantly high energy during the process [97]. For the boride synthesis the reaction is given in equation 2.2.

$$M + B \rightarrow MB \qquad (2.2)$$

2.5.3 Mechanochemical synthesis

Mechanochemical synthesis involves mechanical activation (MA) and reactive grinding processes that begin after the mechanical activation of reactants. Mechanical activation increases the reactivity of powders by expanding the surface area or accelerating the reaction. Mechanical deformation of crystal structures causes local structural excitations and creates unstable thermodynamic conditions that significantly increase chemical reactivity. In plastic deformation, the impact energy obtained in fracture and friction processes is converted into other forms of energy, such as structural defects, broken bonds, and other excess energy types. These energies accumulate in the system and a new and active state of matter is obtained, which increases the chemical reactivity of the powders. Furthermore, the increased surface area of the powder particles eliminates the need for diffusion throughout the product layer. New contact surfaces allow reactions to occur at lower temperatures without the need for any external heat application. Alternatively, the reduction in diffusion distances can significantly lower the reaction temperature as a result of particle thinning [98]. In equation 2.3, where R is the reductant material the boride formation via mechanochemical synthesis is given.

$$2MO + B_2O_3 + 5R = 2MB + 5RO \qquad (2.3)$$

2.5.4 Chemical reduction-based precipitation method

Chemical reduction is the slowest and most common method for synthesizing colloidal nanoparticles due to its simple equipment and ease of use. This involves the reduction of the required coating from a source to a substrate using reducing agents. Smaller nanoparticles are produced using strong reducing agents (sodium borohydride) rather than weak reducing agents (citrate). Even though the process simple and economical the produced particles are generally in amorphous form [99]. The reaction mechanism is demonstrated in equation 2.4.

$$2MCl_2 + 4NaBH_4 + 9H_2O \rightarrow MB_2 + 12.5H_2 + 3HBO_3 \qquad (2.4)$$

2.5.5 Hydrothermal and solvothermal synthesis

Hydrothermal and solvothermal syntheses are important branches of inorganic synthesis. Hydrothermal synthesis refers to synthesis carried out through chemical reactions in an aqueous solution above the boiling point of water, while solvothermal synthesis refers to synthesis carried out in a dry solution at relatively high temperatures. Nanomaterials synthesized using hydrothermal/solvothermal methods exhibit high purity, well-developed crystal structure, and low aggregation; thus, impurities and structural defects arising from calcination at high temperatures or ball milling are prevented. This approach enables the synthesis of single crystals, thin films, and various nanostructures [100].

2.5.6 Vapor phase and thin film deposition methods

Gas phase production usually occurs through the reaction of boron and metal compounds containing chloride with a reductant. In this process, $MeCl_4$ and BCl_3 are mostly used as metal and boron sources, while hydrogen is used as a reductant. The starting materials (metal halide and boron) used for metal boride thin film formation are preferred because they are inexpensive, readily available, used in large quantities and can be applied to various metal systems. With this process, thin films and metal boride coatings are obtained that provide precise control over the composition and structure [101]. The representative reaction is given in equation 2.5

$$MCl_4 + 2BCl_3 + 5H_2 \rightarrow MB + 10HCl \qquad (2.5)$$

2.5.7 Molten salt electrolysis

At the beginning of the century, Sir Humphrey Davy's extraction of alkali metals from molten hydroxides and Michael Faraday's development of the electrolysis rule in 1834 using molten lead halides marked the beginning of molten salt electrolysis studies. In 1886, Hall and Héroult developed the electrolytic production of aluminum from alumina-cryolite, demonstrating the industrial applicability of the method and laying the foundation for today's large-scale plants [83]. Since active metals such as Al, Na, Mg, and Li have a more negative electrode potential than hydrogen, hydrogen gas forms at the cathode instead of metal during electrolysis from aqueous solutions; therefore, methods such as molten salt electrolysis, which operates at high temperatures and removes H^+ ions, are required for the production of these metals. Molten salts offer advantages such as high electrochemical stability and electrical conductivity, low viscosity, and fast reaction kinetics [102].

Chlorides, fluorides, and chloride-fluoride mixtures are mostly chosen as electrolytes; the aim is to increase conductivity, lower the melting point, and control the electrolyte properties. While chloride salts are advantageous due to their low melting temperature and relatively lower corrosive effect, fluoride salts are used more restrictively due to their high melting temperatures and abrasiveness, despite their ability to dissolve oxides well [103].

2.5.7.1 Molten salt electrolysis from oxide salts

The electrochemical boriding process typically involves immersing the metal substrate material in a molten salt electrolyte, usually containing boron compounds such as borax ($Na_2B_4O_7$), and charging it as the cathode. Then, an insoluble material (graphite rod) charged as the anode is subjected to an electric current, causing the boron atoms to be reduced on the metal surface and diffused across the cross-sectional area. This process can be performed at relatively low temperatures, usually between 800°C and 1000°C, depending on the specific application and desired properties.

The high viscosity of molten borax leads to slow movement of ions within the electrolyte. To increase the conductivity and reduce the viscosity of the electrolyte, substances such as oxides, carbonates, and chlorides of alkali and alkaline earth metals, such as Na_2CO_3 and NaCl, are added. These additions reduce the viscosity of the electrolyte, resulting in a less corrosive bath and eliminating many potential problems; however, they incur additional costs in system design [30,31].

The electrochemical boriding process involves two basic reaction steps. First, boron atoms are formed on the surface of the substrate material. Then, these boron atoms diffuse into the substrate material in a specific crystallographic direction, leading to the formation of boride layers [83]. The schematic illustration of the oxide electrolyte based molten salt electrolysis also patented (TR2021012770B, TR2021012771B, US8951402, US10287700) by G.K. Şireli et. al. is given in Figure 2.15.

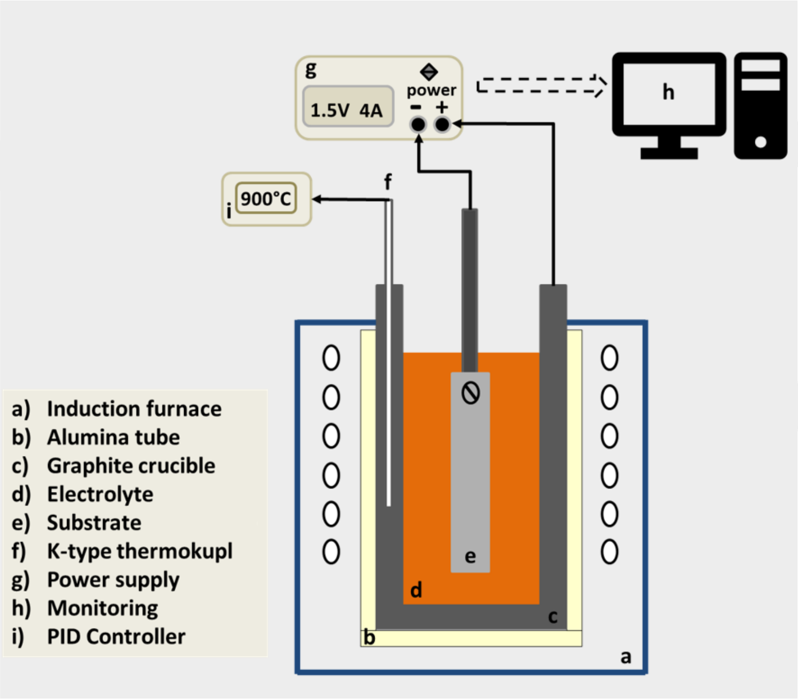

Figure 2.15 : The schematic illustration of oxide based molten salt electrolysis.

3. EXPERIMENTAL PROCEDURE

3.1 Production of Nickel Boride Electrodes

In the scope of this thesis two different approaches were applied in order to fabricate nickel boride electrodes as borided flat and foam surfaces and produced porous disc shaped nickel boride electrodes by producing nickel boride powders via cathodic reduction and thermal diffusion based boriding (CRTD-Bor).

3.1.1 Boriding of flat and foam surfaces

Highly pure nickel materials (99.9%) were selected with two distinct shapes: flat and foam. Samples measuring 0.5 cm x 1 cm x 2 cm and 0.2 cm x 1 cm x 2 cm were prepared for the flat and foam forms, respectively. All samples underwent ultrasonic cleaning with acetone, followed by air drying. The CRTD-Bor process combined with phase homogenization (PH) treatment consists of two main phases: (i) during the CRTD-Bor phase, boron atoms are electrochemically reduced on the cathodically polarized workpiece while simultaneously diffusing into the matrix, and (ii) in the PH stage, no cathodic polarization is applied, allowing for the continuous diffusion of boron atoms into the matrix to form uniform boride structures without any excess boron on the surface. The entire electrode manufacturing process was conducted using a medium-frequency induction furnace (Nersetech), where a graphite crucible functioned as the anode while the nickel pieces were designated as the cathode during the CRTD-Bor period. The electrolyte consisted of 90% borax ($Na_2B_4O_7$) and 10% sodium carbonate (Na_2CO_3). In the PH treatment, the borided substrate was placed in the electrolyte without applying any polarization. Figure 3.1 illustrates the various stages of electrode production schematically.

After 30 minutes of electrolysis at a temperature of 950 °C and a current density of 200 mA/cm², a 10-minute PH process was conducted on flat samples. For the foam, boriding took place at 1000 °C for 45 minutes with a current density of 100 mA/cm², followed by 90 minutes of PH. All specimens that had been treated were taken out of the electrolyte, and the leftover electrolyte was removed by boiling water before being air-dried.

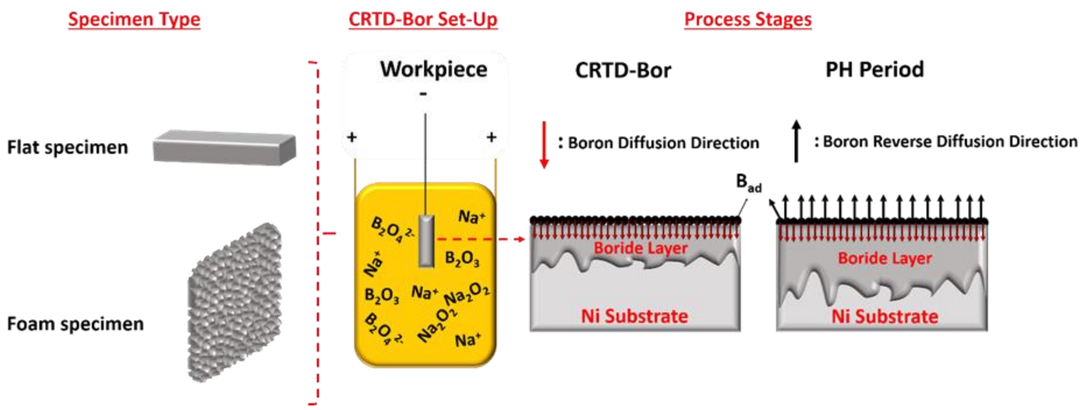

Figure 3.1 : Schematic illustration of nickel boride electrode production.

3.1.2 Production of porous nickel boride discs

High-purity (99.9%) mesh nickel substrates with a 7.5 mm^2 pore size were cut to dimensions of 3 cm x 5 cm x 0.07 cm. The nickel specimens were cleaned using acetone in an ultrasonic bath and subsequently dried in air.

The entire Ni-mesh structure was converted to Ni-boride by boriding the substrate at 1000 °C for 2 hours using CRTD-Bor at a current density of 200 mA/cm^2, followed by 1 hour of PH treatment. After this process, the Ni-boride specimen was cleaned with boiling water and air-dried. Subsequently, the boride samples were ground in a ball mill and cold-pressed to form porous discs.

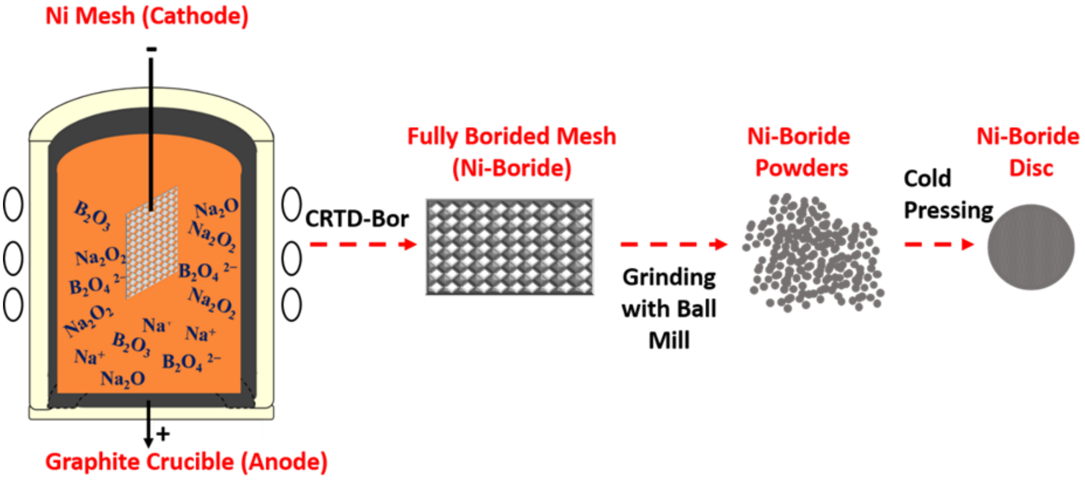

Figure 3.2 : Schematic illustration of Ni-boride disc production.

3.2 Production of Cobalt Boride Electrodes

In this part of the thesis, two different methods were followed for the production of cobalt boride electrodes, as was the case for the production of nickel boride electrodes. In the first stage, flat cobalt surfaces were borided with CRTD-Bor and the properties of the flat surface were examined. In the second stage, porous cobalt/cobalt boride discs were produced by molten salt electrolysis with a co-deposition principle and their detailed investigations were carried out.

3.2.1 Boriding of flat surfaces

Cobalt plates with 99.9% purity were cut to a geometry of 1 cm x 1cm x 0.2 cm and their surfaces were cleaned with acetone in an ultraonic bath. Subsequently the surface was borided at 950 °C and 200 mA/cm^2 for 15 min, following the same experimental procedure described in section 3.1.1. for boriding the nickel substrates. The borided sample was washed with boiling water to remove remnant electrolyte and then air dried.

3.2.2 Production of cobalt/cobalt boride discs

Low carbon steel with the dimensions of 3 cm x 7 cm x 0.2 cm was used as substrate material and was washed with acetone in ultrasonic bath. The co-deposition of Co and B was performed via molten salt electrolysis containing 86% $N_2B_4O_7$, 8% $Co(OH)_2$, 5% Na_2CO_3 and 1% CaF_2 where CaF_2 used as activator and remained chemically stable at reaction temperature. The electrolysis was conducted in graphite crucible which used as anode (+), while steel substrate was polarized as cathode (-). The system was heated via medium frequency induction furnace.

Experiments were performed at 900 °C for 1h under current densities of 200 and 600 mA/cm^2. Following the electrolysis, the Co/Co_xB powders were carefully collected form the substrate surface and washed with diluted HCl to remove remnant electrolyte. The powders were subsequently ground with a ball mill via high purity ethanol and cold-pressed into a disc shape for further electrochemical investigation. A schematic illustration of experimental route is demonstrated in Figure 3.3.

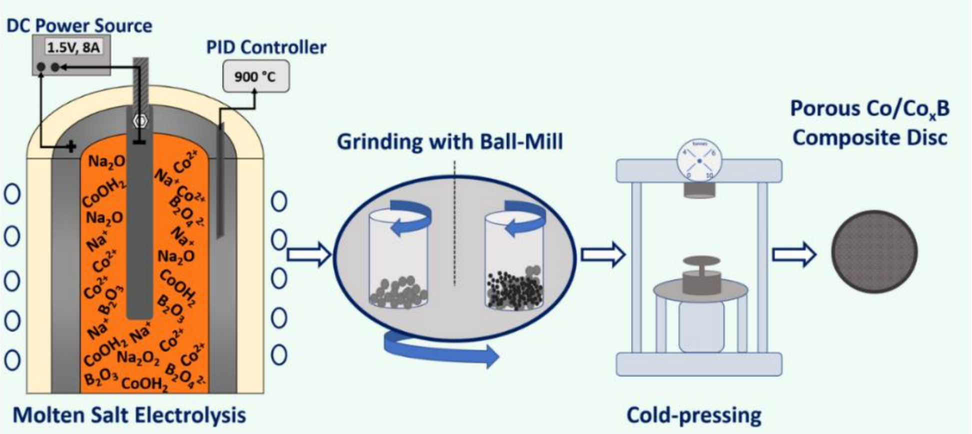

Figure 3.3 : Experimental route to Co/Co$_x$B disc electrode.

3.3 Structural Characterization of the Produced Electrodes

After CRTD-Bor process of flat and foam nickel boride surfaces, X-ray diffractometry (XRD- Philips PW-3710) with Cu-Kα radiation (40 kV, 40 mA) at a glancing angle of 2° was used to identify phase structure of the borides. The cross-sectional investigations borided flat surfaces along with the elemental analyses were carried out via a scanning electron microscope (SEM- CAMECA SX100) equipped with an electron probe microanalyzer (EPMA) and wavelength-dispersive X-ray spectroscopy (WDS). The detailed structural analysis of the outermost surfaces was performed through X-ray photoelectron spectrometry (XPS- Thermo K alpha) and Fourier Transform Infrared Spectrophotometry (FTIR- Bruker Alpha). The surface of the borided foam shape electrodes was also examined via Energy dispersive spectroscopy (EDS) equipped SEM (Thermo Scientific Axia ChemiSEM).

After boriding of nickel mesh with different parameters the cross-sectional investigations were carried out through an optical microscope (OM-Leica-DM 2500 M) to ensure entire cross section of the mesh was borided. The cold pressed disc shape electrode surface was examined via SEM (FEI Quanta FEG 250) and XRD (Philips PW-3710, Cu-Kα radiation (40 kV, 40 mA)). Match 3.15 software was utilized to identify produced phases and for semi-quantitative Rietveld analysis. Furthermore, the crystallographic examinations were conducted via the transmission electron microscope (TEM-Jeol Jem 2100).

In the Co/Co$_x$B composite electrode production, the phase composition of the produced Co/Co$_x$B powders were examined by XRD (Panalytical Aeris, Malvern, UK) using Co-Kα radiation. The morphology and the growth mechanism of the synthesized powders were analyzed by scanning electron microscopy SEM (Thermoscientific Quattro S), besides further microstructural features were examined via TEM (FEI TALOS F200S, 200 kV). In addition, selected area electron diffraction (SAED) was performed for detailed investigation in crystal structure and phase identification.

3.4 Electrochemical Characterization of the Produced Electrodes

The electrochemical behavior of the nickel and cobalt boride electrodes was investigated via Gamry Reference 1010E potentiostat/galvonostat and Biologic SP150 potentiostats. Throughout the process, a three-electrode system was operated, wherein the produced boride pieces served as the working electrode, platinum wire functioned as the counter electrode, and calomel was used as the reference electrode in the 6M KOH solution. To use the disc-shaped Ni and Co boride as an electrode, a copper wire was soldered to the back side of the disc, and then a heat shrink sleeve was applied along the entire wire to ensure sealing. Then, the soldered section of the disc and copper wire were embedded in epoxy. The bare surface was immersed in the electrolyte, while the outer copper tip was connected to the working electrode terminal of the potentiostat (Figure 3.4).

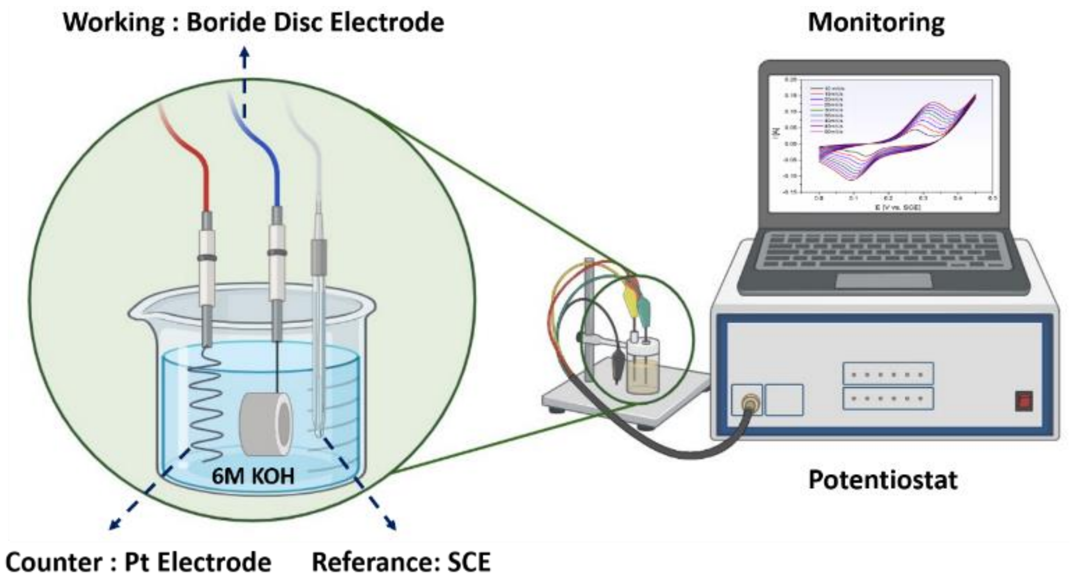

Figure 3.4 : The demonstration of electrochemical testing and 3-electrode system (Drawn in BioRender 2024).

Cyclic voltammetry (CV) measurements were conducted on both flat and foam surfaces up to 2000 cycles at 200 mV/s with the potential range of 0-0.45 V to evaluate the variation in areal capacitance (Ca) during repeating cycles and also with different scan rates (1-50 mV/s and 100 mV/s) to calculate the areal capacitance of the specimens. Additionally, the galvanostatic charge/discharge (GCD) method was conducted to measure the charge/discharge performance of the produced nickel boride electrodes at the range of 0.01 A/cm^2-0.1 A/cm^2 current densities for the flat and foam shape electrodes. The electrochemical impedance spectroscopy (EIS) method was utilized to identify the equivalent circuit elements of the electrochemical cell and provide additional information about the electrochemical performance of the boride electrodes at an open circuit potential with 10 mV amplitude in the frequency range of 100 kHz and 45 mHz.

For the disc shape Ni_xB_y electrode, in the first part of electrochemical tests, the cyclic voltammetry (CV) experiment was conducted up to 2000 cycles at the scan rate of 200 mV/s within 0-0.45 V potential window (V vs. SCE) as in the flat and foam Ni_xB_y electrodes. Then, different scan rates were applied between 10-50 mV/s with 5 mV/s intervals. Likewise, the galvanostatic charge/discharge (GCD) method was performed at 0.01-0.1 A/cm^2 current density range to investigate the charge/discharge behavior of the produced electrode as well as to calculate the energy and the power densities.

In case of Co/Co_xB composite electrodes, CV measurements were conducted up to 750 cycles at 200 mV/s to assess the variation in areal capacitance (Ca) during repeating cycles. In order to evaluate the charge-transfer kinetics of electrodes, CV tests were also performed at different scan rates ranging from 10-100 mV/s. GCD tests were conducted to investigate charge/discharge ability of the electrodes at different current densities (0.01- 0.1 A/cm^2). Furthermore, LSV experiments were utilized to investigate and compare the surface electrocatalytic activity of the electrodes within the potential range of 0-0.5 V at a scan rate of 1 mV/s.

4. RESULTS AND DISCUSSION

4.1 Structural and Electrochemical Properties of Flat and Foam Nickel Boride Surfaces

The thin film XRD analysis of borided flat sample indicated the presence of a combination of nickel boride structures, including NiB, Ni_4B_3, and Ni_2B, with Ni_4B_3 being the most prevalent one (Figure 4.1a). Cross-sectional studies using EPMA validated the formation of three distinct boride phases, which exhibited different color contrasts in SEM image (Figure 4.1b). Elemental analysis with WDS (shown in Table 4.1) revealed boron concentrations of 47.7 at.% and 46.2 at.% at points 1 and 3, respectively, while the nickel concentrations were measured at 52.3 at.% and 53.4 at.%, respectively. This aligns well with the stoichiometric ratio expected for the NiB phase that forms on the top surface, attributed to the high level of boron atoms that have diffused.

At points 2, 4, 5, 6, and 7, boron concentrations ranged from 37 to 39 at.%, while nickel contents were measured at 60 to 62 at.%, consistent with the stoichiometry of Ni_4B_3. Although non-uniform NiB islands with a darker appearance were observed on the uppermost surface, the predominant boride structure was Ni_4B_3. This predominance can be attributed to the more negative Gibbs free energy of formation value of Ni_4B_3 compared to the other borides (Figure 4.2). At point 8 in Figure 4.2b, a third phase was identified, containing 30 at.% boron and 70 at.% nickel, corresponding to the stoichiometry of the Ni_2B phase. At point 9, the boron content decreased sharply to 2.34 at.%, and further declined to 1.37 at.% at point 13. Therefore, the region between points 9 and 13 can be designated as the diffusion zone, with an average depth of ~150 µm.

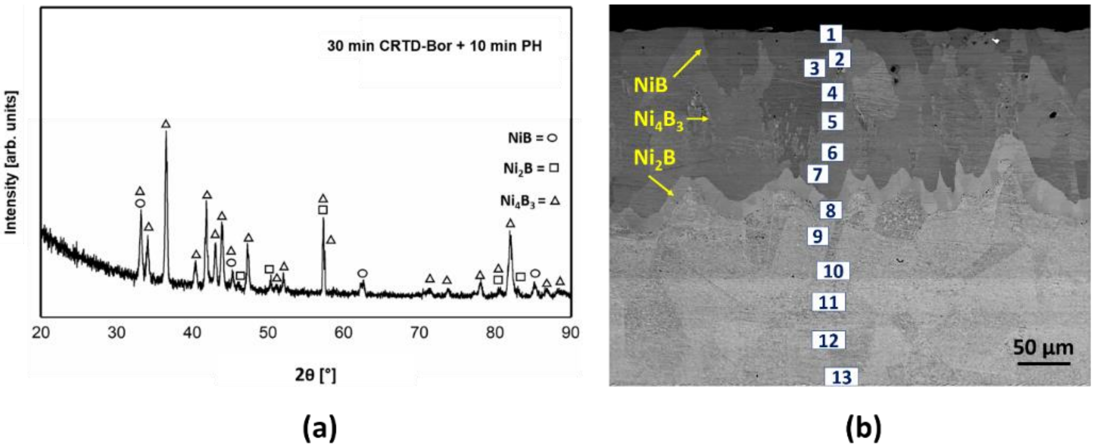

Figure 4.1 : a) Thin film XRD pattern and **b)** cross-sectional micrograph of borided nickel flat electrode with WDS elemental analysis points.

Table 4.1 : Results of the WDS analysis of the points in at.% marked in Figure 4.1b.

Spectrum Point	B	Ni
1	47.74	52.26
2	39.7	60.2
3	46.54	53.46
4	37.4	62.6
5	38.1	60.96
6	39.04	60.96
7	37.75	62.25
8	30.77	69.23
9	2.34	97.66
10	2.1	97.9
11	1.79	98.3
12	1.73	98.21
13	1.37	98.63

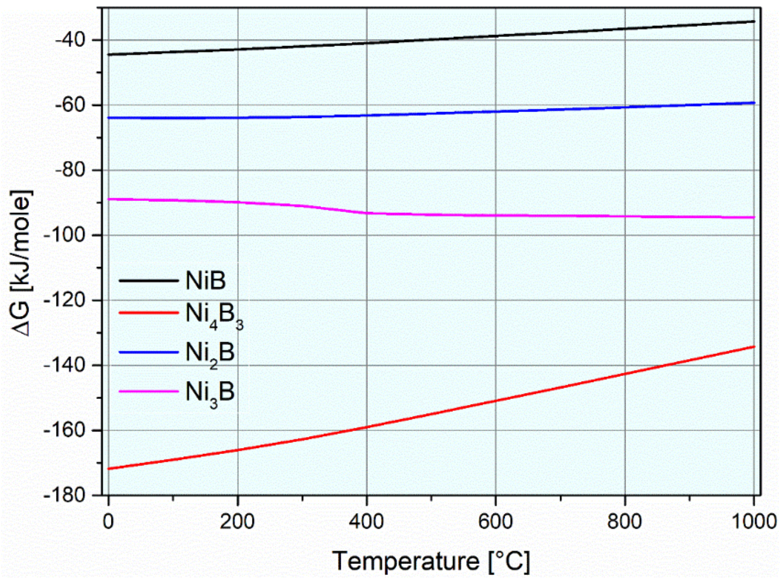

Figure 4.2 : Variations in Gibbs free energy of formation values of nickel borides with temperature [HSC Chemistry ver. 4.1.].

Figure 4.3 presents an SEM micrograph of the borided nickel foam structure, accompanied by EDS-elemental mapping analysis, which reveals homogeneous nickel boride formations with a consistent Ni_4B_3 stoichiometry. The similarity in boride phase compositions formed on both flat and foam-shaped substrates enables a direct comparison of the influence of substrate geometry on the electrochemical properties and performance of the resulting electrodes.

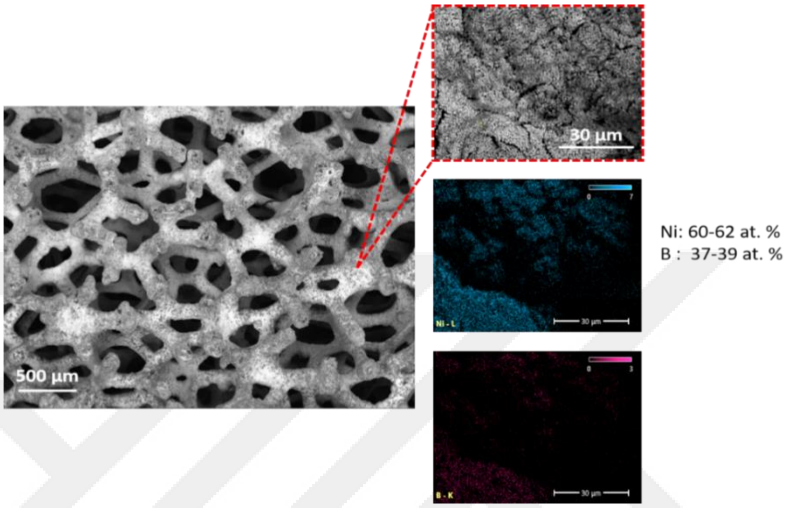

Figure 4.3 : Micrograph and mapping analyses of borided nickel foam.

A three-electrode system was implemented to evaluate the electrochemical properties of electrodes fabricated in two distinct geometries. Cyclic voltammetry (CV) experiments were conducted at a scan rate of 100 mV/s for 2000 cycles (Figures 4.4a and 4.4c). The areal capacitance (C_a) of the electrodes was determined using equation 4.1, where ν represents the scan rate, S denotes the electrode area, ΔV is the potential range, and I(V) is the integral of the CV curve.

$$Ca=\frac{1}{2vS\Delta V}\int I(V)dV \tag{4.1}$$

Figure 4.4b presents the C_a values for flat specimens, calculated as approximately 35, 170, 270, 325, and 350 mF/cm² for the 10th, 500th, 1000th, 1500th, and 2000th cycles at a 100 mV/s scan rate, respectively. The observed increase in C_a values, with an R^2 of 0.998, suggests a non-linear trend characterized by a diminishing rate of increase (Figure 4.4b). The consistent rise in areal capacitance with each cycle indicates the potential of nickel borides as electrode materials for supercapacitor applications. These values were obtained from flat surfaces. It can be inferred that transforming the substrate geometry into a porous structure would increase the surface area, potentially enhancing capacitance due to additional Faradaic reactions [104,105]. Consequently, foam structures yielded C_a values of 250, 410, 585, 720, and 760 mF/cm² for the 5th, 500th, 1000th, 1500th, and 2000th cycles at a 100 mV/s scan rate, respectively. A similar trend of a decreasing rate of increase in C_a with cycle number was observed for the foam electrode, as seen in the flat specimen (Figure 4.4d).

When comparing the rate of increase in C_a values with cycling, the flat electrode exhibited a significant change (approximately tenfold), whereas the foam electrode showed a smaller increase (approximately threefold). This difference is attributed to the initially high C_a value observed in the foam structure, which results from its greater surface area and porosity. These characteristics provide more electroactive sites and facilitate faster ion diffusion at the electrode/electrolyte interface [104,106].

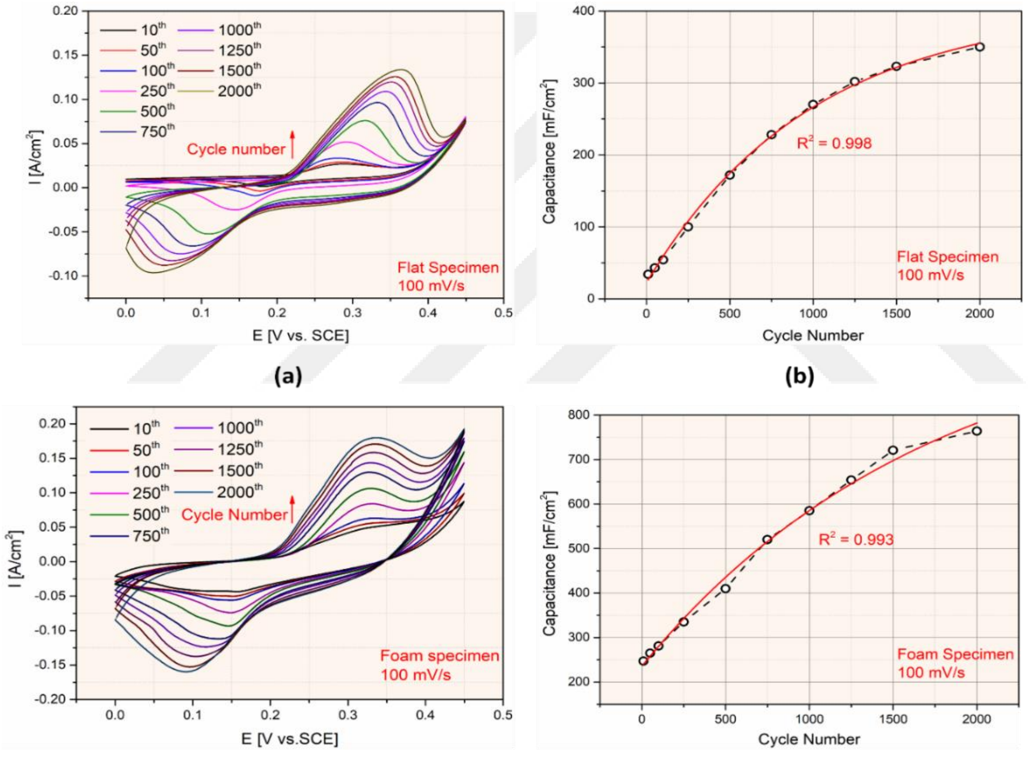

(c) (d)

Figure 4.4 : Cyclic voltammograms of flat (a) and foam (c) at 100 mV/s scan rate up to 2000 cycles. Non-linear fitting of the capacitance increments in flat (b) and foam (d) with respect to cycle number.

Cyclic voltammetry (CV) experiments were also performed at various scan rates (1–50 mV/s) on both geometries (Figures 4.5a and 4.5c) to investigate reaction kinetics. The relationship between anodic peak current (*i*) and scan rate (*v*) was analyzed using the power law, where *b* represents the slope of the *log(i)* versus *log*(*v*) curve and a is a constant. The b value indicates the dominant mechanism, with a value of 0.5 corresponding to diffusion control and 1.0 to capacitive control. The calculated b values were 0.74 and 0.66 for flat and foam electrodes, respectively (Figures 4.5b and 4.5d), indicating that the produced electrodes operate under mixed control.

Further analysis of the capacitive and diffusive contributions to energy storage can be conducted using either the Trasatti [107] or Dunn's methods [108]. Given that the electrodes exhibited typical pseudo-capacitor behavior, as evidenced by the shift of peak currents to more positive and negative potentials with increasing scan rates, the Trasatti method [109] is considered more appropriate for this study.

The Trasatti method examines the change in capacity as a function of $1/v^{1/2}$ (Figures 6e and 6g) to determine C_o (y-intercept), which represents the capacitive contribution. Additionally, plotting 1/C versus $v^{1/2}$ (Figures 4.5f and 4.5h) enables calculation of the total capacitance as $1/C_T$ (y-intercept). Using the equation $C_T = C_i + C_o$, the diffusive contribution (C_i, associated with the faradaic reaction) and the capacitive contribution (C_o, related to double-layer capacitance) can be quantified [109].

In this study, C_o values of 71% and 40.6% and C_i values of 29% and 59.4% were obtained for flat and foam electrodes, respectively. These results align with the calculated b values and the mixed-controlled reaction model. The significantly higher capacitive contribution observed in flat electrodes is likely attributable to the double-layer capacitance characteristic of flat geometries, which facilitates rapid charge arrangement.

Table 4.2 presents a summary of the literature on nickel-based electrodes. Because the fabricated electrodes are bulky and only the surface is electrochemically active due to the selected production method, calculating areal capacitance is more appropriate than specific capacitance, which considers electroactive mass. As shown in the table, both specific and areal capacitance of the produced electrodes depend on several factors, including additive type and quantity, substrate selection and morphology, electrode area or mass, electrolyte type and concentration, and the applied scan rate in cyclic voltammetry. In this study, although C_a values were calculated at multiple scan rates, only those obtained at 10 mV/s and 100 mV/s were selected to enable more accurate comparison with reported data.

The C_a values obtained at 100 mV/s are at least ten times higher than those reported for nickel boride-based electrodes [110,111]. When comparing C_a values for nickel oxide/hydroxide structures, the produced electrode also exhibited higher values at a 10 mV/s scan rate [112,113].

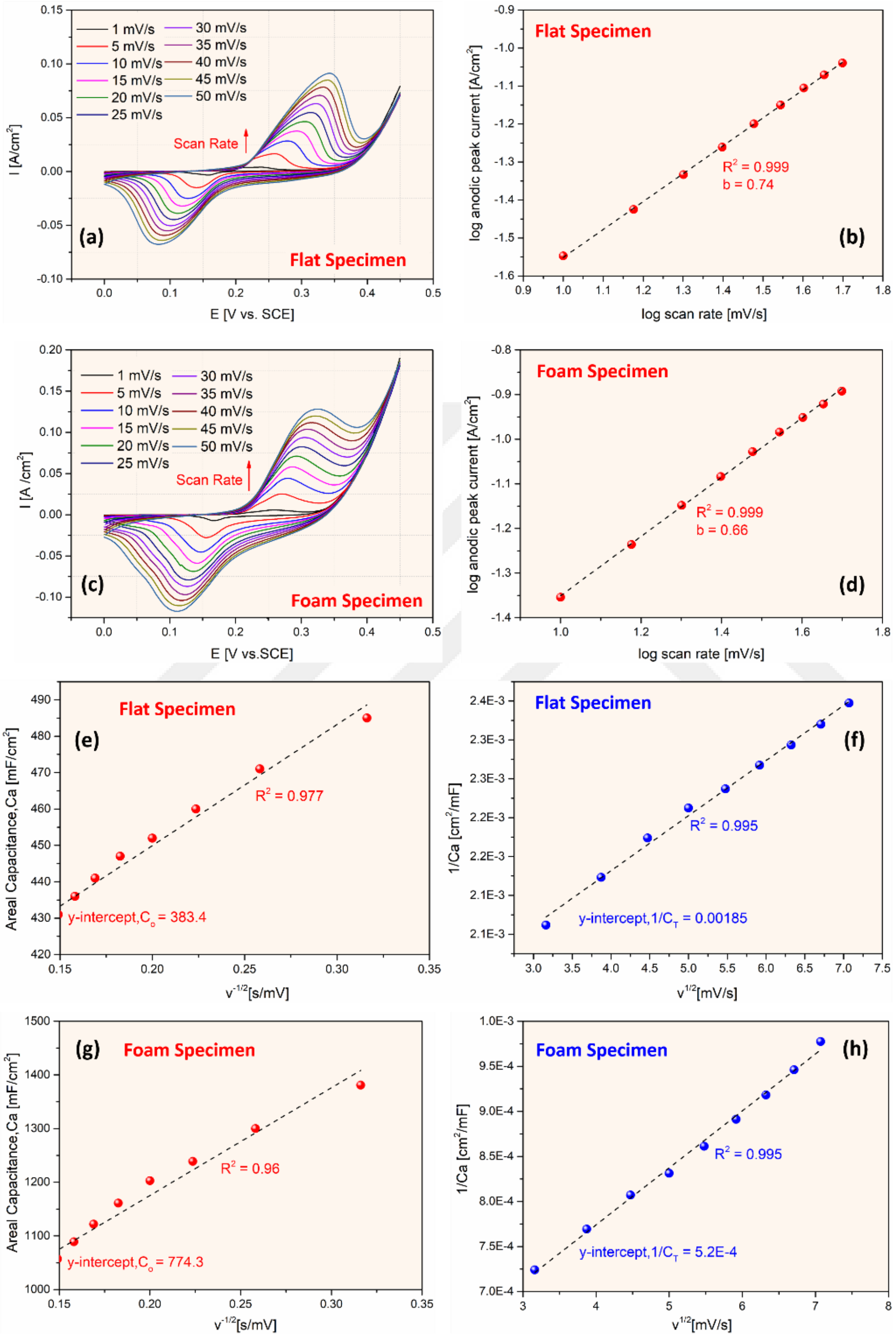

Figure 4.5 : Cyclic voltammograms of flat (a) and foam (c) at different scan rates (1-50 mV/s). Log anodic peak current vs. Log scan rate diagrams of flat (b) and foam (d). Plot of areal capacitance (Ca) versus $v^{-1/2}$ for flat (e) and foam (f) Plot of 1/Ct versus $v^{1/2}$ of flat (g) and foam (h).

Table 4.2 : Electrochemical performance of various Ni-based electrodes.

Material/Electrode	Production Type	Capacitance	Electrolyte	Scan Rate	Reference
NixB	Chemical precipitation	1334 F.g^{-1}	6M KOH	5 mV.s^{-1}	[114]
NixB/Graphane	Chemical precipitation	1822 F.g^{-1}	6M KOH	5 mV.s^{-1}	[114]
Amorphous Ni-B Alloy	Direct aqueous solution synthesis	2230 F.g^{-1}	2M KOH	5 mV.s^{-1}	[115]
Amorphous Ni-B Alloy	Chemical Reduction	562 F.g^{-1}	6M KOH	5 mV.s^{-1}	[116]
Ni_9S_8@Ni_2B composite	Chemical Reduction	901.2 C g^{-1}	2M KOH	5 mV.s^{-1}	[117]
Ni_2B/RGO nanoparticle	One-step reduction	1073.4 F. g^{-1}	6M KOH	-	[11]
Ni–B/MCNAs	Wetness technique and Chemical reduction	733 F g^{-1}	6M KOH	5 mV.s^{-1}	[118]
Amorphous NiB	Single-step redox approach	83.33 F g^{-1}	5M KOH	-	[119]
Amorphous Ni-B Alloy	Chemical Reduction	562 F.g^{-1}	6M KOH	5 mV.s^{-1}	[120]
NiB	Electroless Deposition	24.61 mF.cm^{-2}	2M KOH	100 mV.s^{-1}	[110]
CNWs-NiB	Electroless Deposition	52.58 mF.cm^{-2}	1M Na_2SO_4	100 mV.s^{-1}	[121]
SiNWs-NiB	Electroless Deposition	30.4 mF.cm^{-2}	1M Na_2SO_4	100 mV.s^{-1}	[121]
NiO	Hydrothermal Synthesis	137.7 F.g^{-1}	2M KOH	10 mV.s^{-1}	[122]
NiO nanowire	Electrospinning	670 F.g^{-1}	6M KOH	-	[21]
NiO nanoparticles	Sol-Gel	549 F.g^{-1}	1M KOH	1 mV.s^{-1}	[123]
Mesoporous Sphere NiO/CNT	Hydrothermal Synthesis	1329 F.g^{-1}	1M KOH	10 mV.s^{-1}	[124]
NiO/RGO composites	Hydrothermal Synthesis	1016.6 F.g^{-1}	6M KOH	1 mV.s^{-1}	[125]
NiO nanoflake film	Hydrothermal Synthesis	74.8 mF/cm^{2}	1M KOH	10 mV.s^{-1}	[112]
γ-NiOOH flakes	Anodic oxidation	1200 mF.cm^{-2}	6M KOH	25 mV.s^{-1}	[113]
Ni_xB_y (Flat Surface)	CRTD-Bor	478 mF.cm^{-2}	6M KOH	10 mV.s^{-1}	This work
Ni_xB_y (Foam Surface)	CRTD-Bor	1385 mF.cm^{-2}	6M KOH	10 mV.s^{-1}	This work
Ni_xB_y (Flat Surface)	CRTD-Bor	350 mF.cm^{-2}	6M KOH	100 mV.s^{-1}	This work
Ni_xB_y (Foam Surface)	CRTD-Bor	760 mF.cm^{-2}	6M KOH	100 mV.s^{-1}	This work

Following the 2000th cycle of CV, additional XRD and EPMA analyses were performed on the flat electrode to identify surface structural changes and elucidate the mechanism of Faradaic reactions (Figure 4.6a).

The XRD pattern revealed no significant changes, except for the emergence of new peaks corresponding to the Ni_4B_3 phase and the disappearance of certain peaks associated with the NiB phase. These results suggest that no substantial structural variations related to stable bulk oxide or hydroxide formation occurred as a consequence of the Faradaic reactions.

The cross-sectional EPMA micrograph and corresponding elemental analyses (Figure 4.6b and Table 4.3) corroborate the XRD findings by demonstrating the absence of oxide or additional phase growth. Furthermore, the elemental compositions remained nearly identical to those measured prior to the CV test, as shown in Figure 4.1b and Table 4.1.

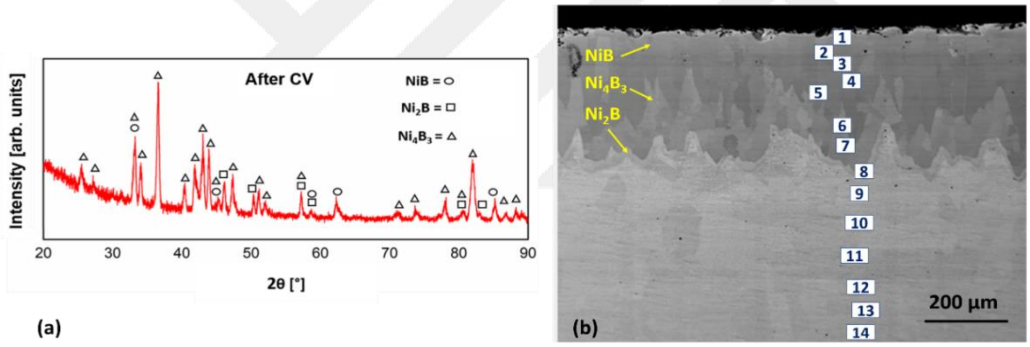

Figure 4.6 : After the 2000th cycle of CV, borided flat specimen’s a) thin film XRD pattern b) cross-sectional image with elemental analysis marks.

Table 4.3 : Results of the WDS analysis in at.% of points marked in Figure 4.6b.

Spectrum Point	B	Ni
1	47.74	52.26
2	47.2	52.8
3	46.54	53.46
4	46.81	53.19
5	45.57	54.43
6	39.04	60.96
7	37.75	62.25
8	30.8	69.2
9	4.12	95.88
10	2.1	97.9
11	0.42	99.58
12	0.54	99.46
13	0.38	99.62
14	0.45	99.55

Additional galvanostatic charge and discharge experiments were performed at varying current densities (10-100 mA/cm² for flat electrodes and 10-50 mA/cm² for foam electrodes). Figures 4.7a and 4.7b present the GCD profiles of flat and foam surfaces, respectively. The asymmetric triangular shape of the curves indicates a mixed control system, involving both capacitive and faradaic charge storage, where energy storage is governed by electrical double layer and faradaic redox reactions [126]. The observed charge-discharge curve trend further demonstrates the rapid discharging behavior of the boride electrodes, a critical property for supercapacitor applications.

Comparison of the two geometries reveals that foam structures exhibit significantly faster charge and discharge characteristics than flat electrodes, likely due to the increased surface area and greater number of surface-active sites present in the foam (Figure 4.7c) [29,127]. Electrochemical impedance spectroscopy (EIS) measurements were conducted between 100 kHz and 45 mHz to further elucidate the electrochemical properties of nickel boride electrodes. As shown in Figure 4.7d, the Nyquist plots for both flat and foam electrodes lack a semicircle in the high-frequency region, while steeper straight lines are observed in the low-frequency region [128].

Impedance spectroscopy measurements were used to model equivalent circuits comprising the solution resistance (R_s) in series with a parallel combination of the double layer constant phase element (Q_{dl}) and the impedance associated with the Faradaic reaction (Z_w), including the charge transfer resistance (R_{ct}). Analysis of the Nyquist plots (Figure 4.7d) shows that the slope of the Warburg curve is substantially higher for the foam electrode compared to the flat electrode, which suggests more rapid and efficient charge transfer. The Bode plots (Figures 4.7e and 4.7f) display phase shifts of approximately -65° for the flat electrode and -70° for the foam electrode. A phase angle of -90° is indicative of an ideal capacitor, whereas -45° reflects pseudocapacitive behavior [129]. Consequently, the system examined in this study can be classified as mixed controlled.

Following the establishment of the equivalent circuit for the working system, fitting was performed and the results are presented in Table 4.4. Comparison of flat and foam-shaped electrodes revealed significant differences in charge transfer resistance at high frequencies and mass transfer resistance at low frequencies. The foam electrode exhibited approximately 25 times lower charge transfer resistance, attributed to its higher surface area and increased number of active sites. This reduction facilitates efficient charge transfer and improved energy storage, resulting in higher areal capacitance for the foam electrode. In contrast, the foam surface demonstrated a tenfold increase in mass transfer resistance. This increase is likely due to the pronounced surface roughness of the foam structure, which creates pH gradients between the foam holes and frames. The roughness impedes mass transfer within the system, thereby increasing resistance formation [130].

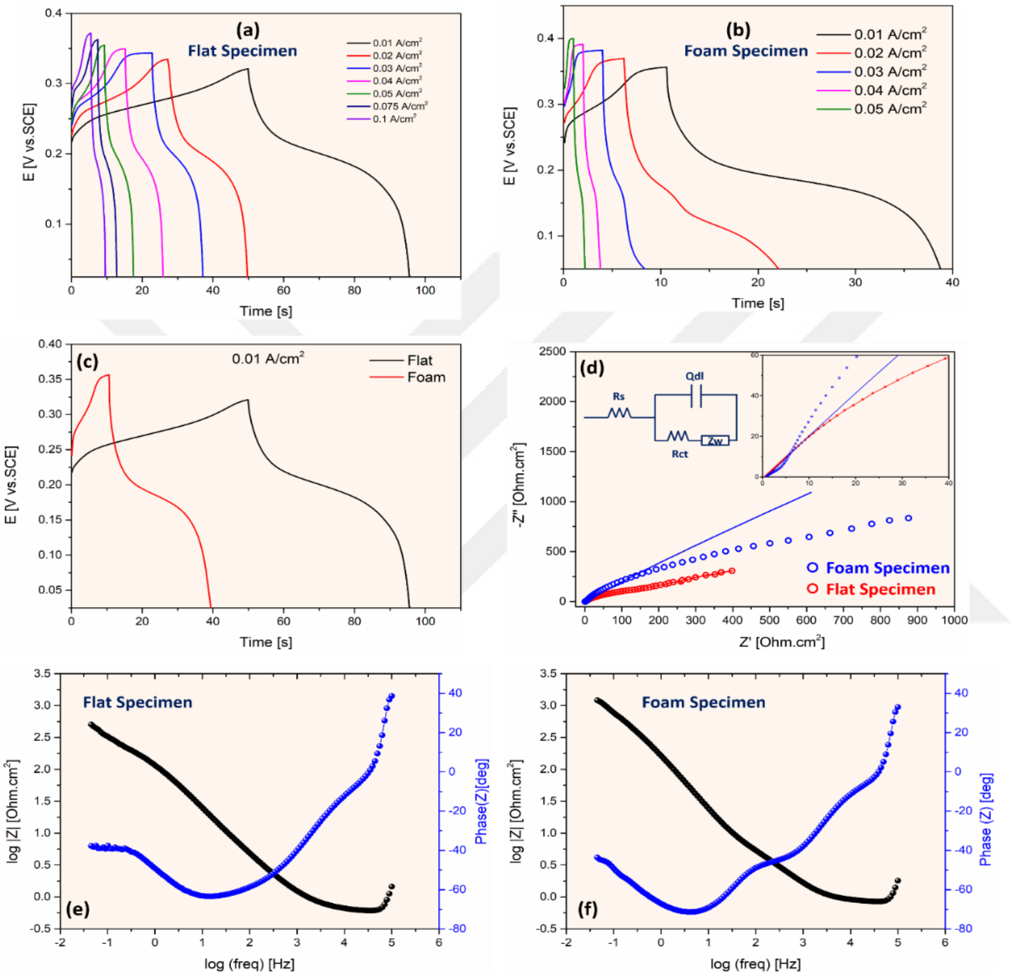

Figure 4.7 : GCD curves of flat (a)**,** foam (b) electrodes at different current densities, Comparison of GCD behavior of flat and foam electrodes (c) Nyquist plots of flat and, foam electrodes (d). Bode plots of flat (e), foam (f) electrodes.

Table 4.4 : Equivalent circuit elements of flat and foam electrodes.

	Nickel boride flat electrode	**Nickel boride foam electrode**
Solution Resistance (R_s)	0.5 Ω	0.7 Ω
Double layer constant phase element (Q_{dl})	2 e^{-3} $F.s^{(a-1)}$	1.75 e^{-3} $F.s^{(a-1)}$
Coefficient for CPE	0.75	0.75
Charge Transfer Resistance (R_{ct})	230 Ω	9 Ω
Mass Transfer Resistance (Z_w)	120 $Ω.s^{-1/2}$	1200 $Ω.s^{-1/2}$

To elucidate the high capacitance of the fabricated electrodes and identify potential Faradaic reactions, XPS analysis was performed before and after 2000-cycle CV experiments on the flat surface. The variations in nickel, boron, and oxygen content were systematically investigated. Figures 4.8a and 4.8b demonstrate that stable nickel boride structures were present on the surface both before and after CV, as indicated by the characteristic Ni-B peaks at 854.5 and 872.2 eV, corresponding to the 2+ oxidation state of nickel [130,131]. Following CV, two additional peaks at 856.3 and 874.4 eV were observed, representing the binding energies of the Ni-O bond and the presence of Ni^{3+} [132–136]. The appearance of satellite peaks at 879.2 and 860.9 eV further indicates the oxidation of nickel [136].

For boron (Figures 4.8c and 4.8d), both B-Ni (188.5 eV) and B-O (191.5 eV) peaks were detected prior to CV. After CV, the B-Ni peak was no longer observed, and only the B-O peak remained [133,135,137,138].

Figures 4.8e and 4.8f present the oxygen spectra, where both O-B (532.1 eV, O_I) and O-H (529.1 eV, O_{II}) peaks were detected before and after CV. This observation indicates oxygen adsorption on the specimen surface and nickel oxidation during the CV experiment [137,138]. The data suggest an increase in oxygen concentration on the nickel boride electrode surface, while the stable nickel boride structure was maintained, as evidenced by the persistence of Ni-B peaks after 2000-cycle CV experiments.

The Pourbaix diagram of nickel, presented in Figures 4.9, illustrate the behavior of nickel under strongly alkaline conditions (pH 14). The Frost diagram of nickel [80] (Figure 2.12a) indicates that the most stable phase is nickel hydroxide, specifically $Ni(OH)_2$, in the 2+ oxidation state. The highest valence state (4+) of nickel exhibits a labile character due to its high positive nE° value, indicating instability. Consequently, passivation of nickel to the NiO_2 form is not feasible, as it tends to disproportionate to oxyhydroxide and subsequently to hydroxide. This behavior at the electrode/electrolyte interface may account for the observed increase in capacitance of nickel boride electrodes with increasing cycles of CV particularly beyond 2000 cycles. Figure 4.9 shows that, at pH 14, nickel is prone to oxidation, which is consistent with the Ni-O peak observed in XPS results. However, these oxide formations occur at the atomic level and are not detectable by thin film X-ray diffraction (XRD) or electron microprobe analysis (EMPA), as previously discussed. For boron, at pH 14 (Figure

4.9), the formation of oxyanions leads to instability. The disappearance of the B-B peak and the increased intensity of the B-O peak after 2000 CV cycles, as observed in XPS results, further support this conclusion.

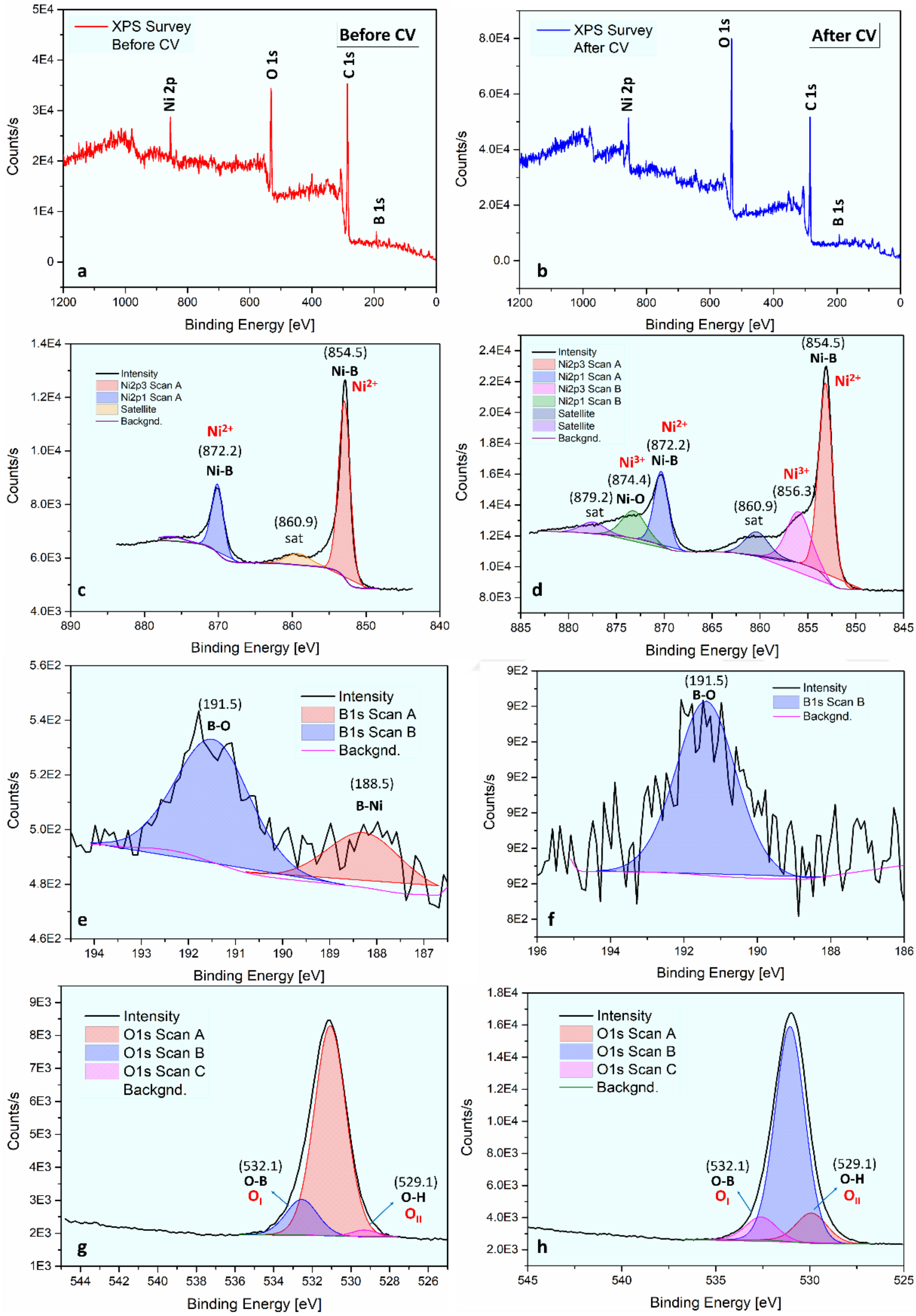

Figure 4.8 : XPS survey obtained on flat nickel boride electrodes (a) before and (b) after CV for 2000 cycles. Detailed XPS spectra of (c,d) nickel, (e,f) boron abd (g,h) oxygen before and after CV, respectively.

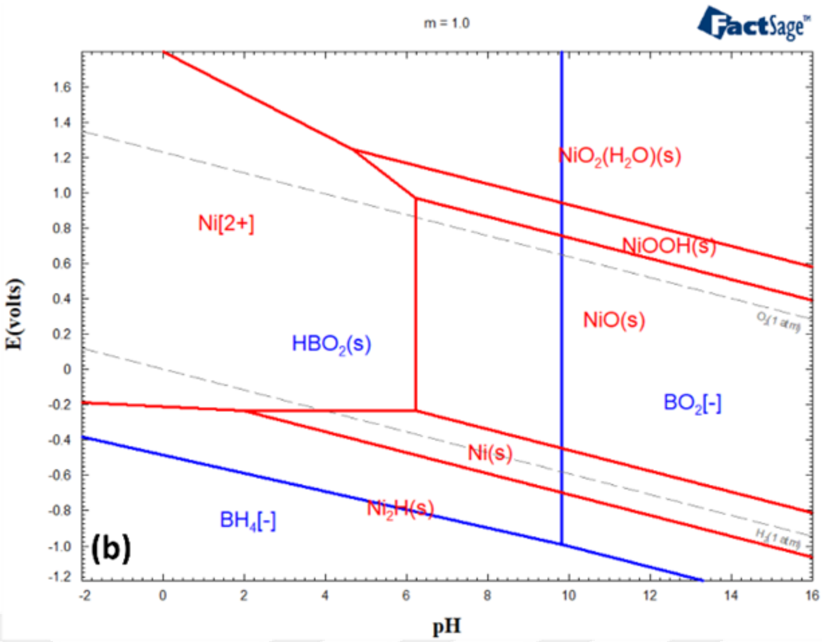

Figure 4.9 : Pourbaix diagram of nickel [FactSage education ver. 8.3].

Fourier-transform infrared (FTIR) analyses were conducted on boride flat electrodes before and after CV experiments (Figure 4.10). Following 2000 CV cycles, the intensity of B-O peaks increased, as did the O-H peak [139,140]. This increase is consistent with the repeated oxidation and reduction processes experienced by the electrodes during prolonged exposure to a strong alkaline environment (6M KOH). These results are in agreement with the findings of XPS analyses (Figure 4.8).

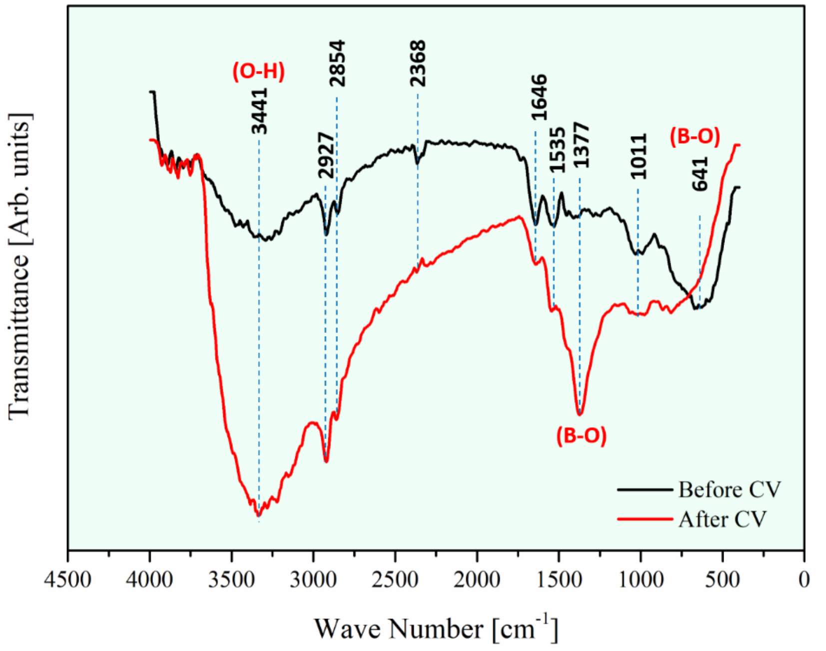

Figure 4.10 : FTIR spectrum of nickel boride electrode before and after CV experiments.

Given the high oxygen affinity of nickel and boron in alkaline environments (Figure 4.9) and the interpretation of XPS and FTIR results (Figures 4.8 and 4.10), the possible Faradaic reactions that account for the capacitive behavior of nickel boride are presented in equations 4.2 to 4.4. These reactions occur at the defective and active regions of the electrode–electrolyte interface. During the anodic cycle, both the formation of a labile compound and the decomposition of water are observed, whereas the cathodic cycle results exclusively in hydrogen gas generation.

$$\text{Anodic Reaction: } Ni_xB_y + H_2O = Ni_xB_yO_z^{\star} + 2H^+ + 2e^- \qquad (4.2)$$

$$\text{Anodic Reaction: } H_2O = 1/2\ O_2 + 2H^+ + 2e^- \qquad (4.3)$$

$$\text{Cathodic Reaction: } 2H_2O + 2e^- = H_2 + 2OH^- \qquad (4.4)$$

4.2 Structural and Electrochemical Properties of Porous Disc Shape Nickel Boride Electrode

Structural analysis demonstrated that the entire Ni-mesh substrate (Figure 4.11a) was transformed into the boride form, as illustrated in Figure 4.11b. Several boride phases were identified, distinguished by differences in color contrast. Voids and cracks were present, which are attributed to the intrinsic brittleness of borides [30]. The fully converted nickel boride samples were ground using a ball mill to evaluate phase composition. XRD analysis (Figure 4.11c) indicated that the resulting powders comprised of NiB, Ni_4B_3, Ni_2B, and Ni_3B phases in proportions of 5%, 49%, 34%, and 12%, respectively (Figure 4.11d).

Nickel boride powders were then cold-pressed to obtain porous discs for the electrochemical performance test. The general appearance of disc-shaped powders is given in Figure 4.12a. The average particle size of the Ni_xB_y (Ni_xB_y; $4 \geq x \geq 1$, $3 \geq y \geq 1$), powders was determined as ~ 4 µm according to the ImageJ program (Figure 4.12b).

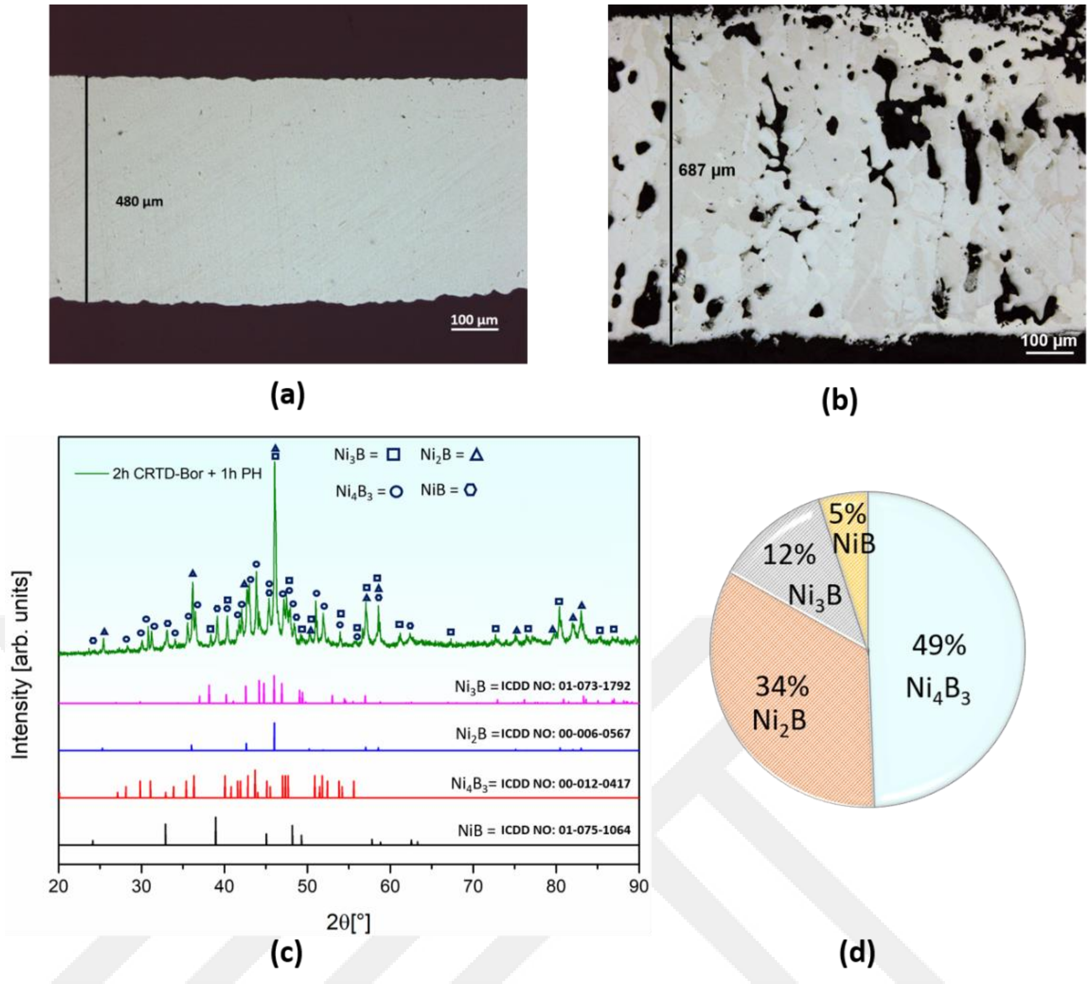

(a) (b) (c) (d)

Figure 4.11 : Cross-sectional optical micrograph of a) untreated, b) completely nickel boride converted mesh; c) XRD pattern, and d) Rietveld analysis of nickel boride powders [1000 °C, 2h of CRTD-Bor @ 200 mA/cm^2 plus 1h of PH].

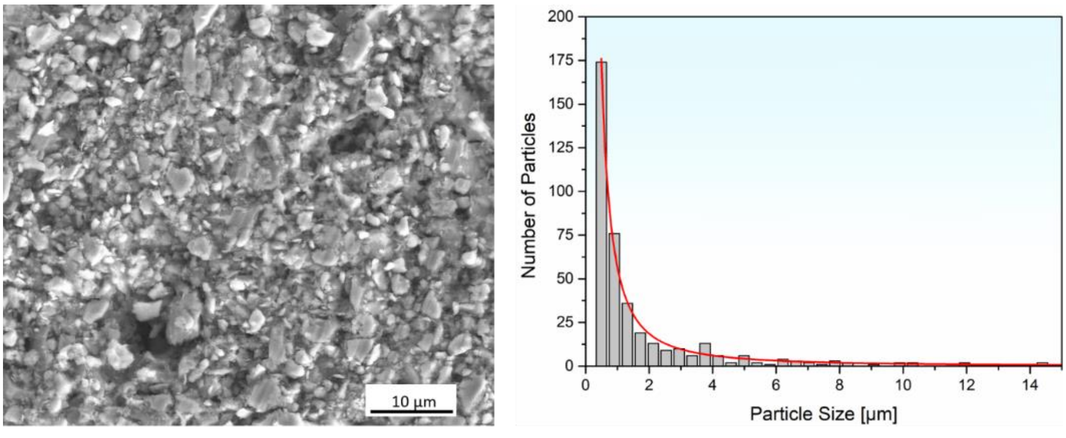

(a) (b)

Figure 4.12 : a) SEM micrograph and b) particle size distribution of disc-shaped Ni_xB_y powder.

The crystallographic characteristics of the powders, as determined by XRD analysis, are presented in Table 4.5. According to the results, NiB, Ni_4B_3, and Ni_3B crystallize in the orthorhombic system, whereas Ni_2B adopts a tetragonal structure. The corresponding space groups for these compounds are Cmcm, Pnma, Pnma, and I-42, respectively. The actual crystal structures of the synthesized phases were modeled using VESTA software [141] and are shown in Figure 4.13. In both NiB and Ni_4B_3, boron-boron interactions are stronger than in Ni_2B and Ni_3B; specifically, boron zigzag chains are present in NiB, while boron double chains are found in Ni_4B_3. In contrast, Ni_2B and Ni_3B exhibit isolated boron atoms arranged in layers with nickel atoms [16]. In all cases, nickel borides display strong covalent bonding, including Ni-B, Ni-Ni, and B-B interactions.

Table 4.5 : The structural properties of synthesized nickel boride phases.

	NiB	**Ni_4B_3**	**Ni_2B**	**Ni_3B**
Card number	00-006-0567	00-012-0417	01-075-1064	01-073-1792
Space group	Cmcm	Pnma	I-42m	Pnma
Crystal system	orthorhombic	orthorhombic	tetragonal	orthorhombic
Unit cell	a= 2.9360Å b= 7.3800Å c= 2.9680 Å	a= 11.9480 Å b= 2.9791 Å c= 6.5637 Å	a= 4.9800 Å c= 4.2360 Å	a= 5.2105 Å b= 6.6174 Å c= 4.3904 Å
Calculated density	7.17 g/cm^3	7.58 g/cm^3	8.11 g/cm^3	8.20 g/cm^3

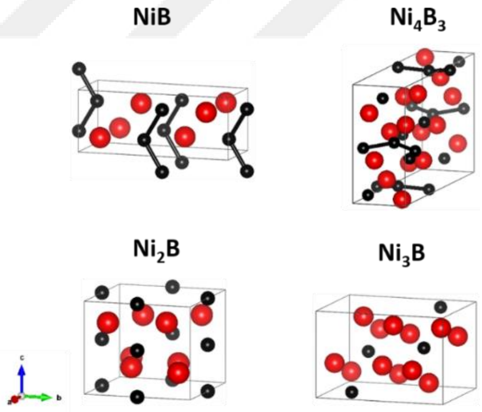

Figure 4.13 : Crystal structures of synthesized borides with the projection on the (001) plane; drawn by VESTA (Red and black atoms represent nickel and boron, respectively).

Additional TEM examinations, as shown in Figure 4.14, including a bright field image of Ni_xB_y powders and the ring pattern of a magnified selected area, were performed to assess the crystallinity of the synthesized powders and to corroborate the XRD findings. The observed ring pattern in the diffraction analysis indicated a polycrystalline structure with the coexistence of different stoichiometric phases. The Ni_2B ring patterns corresponded to the (213), (222), (310), (220), (211), and (002) planes, with d spacing of 2.14, 1.91, 0.75, 0.15, and 0.13 Å, respectively. Based on the XRD results, Ni_2B was identified as the second most abundant phase, suggesting that the TEM diffraction was likely obtained from a Ni_2B-rich region within the multiphase powder.

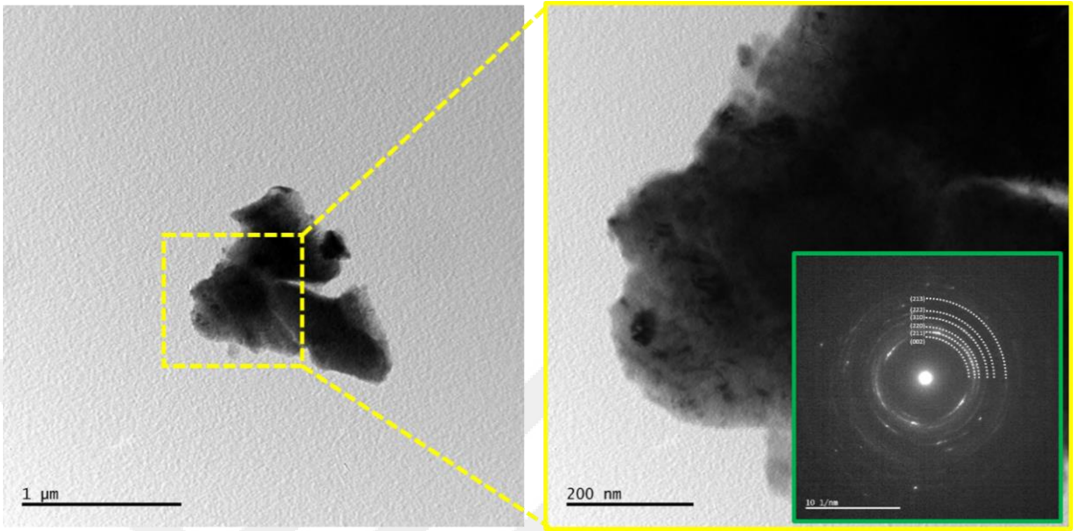

Figure 4.14 : Bright-field TEM images of Ni_xB_y powder and corresponding ring pattern of the selected region.

A three-electrode system was set up to evaluate the electrochemical properties of porous electrodes fabricated in disc form. CV curves of the Ni_xB_y electrode after 2000 cycles at the constant scan rate of 200 mV/s are presented in Figure 4.15a. The C_a value of the synthesized electrode was calculated by using equation 4.1.

The C_a capacity variation across different cycles at a constant scan rate of 200 mV/s exhibited an initial increase up to the 1000th cycle, after which it remained nearly constant until the 2000th cycle. At the 10th cycle, the C_a value was measured at 295 mF/cm^2, increasing to 520 mF/cm^2 by the 2000th cycle (Figure 4.15b). Nickel, as a catalytic metal, becomes more active with continuous voltage application due to the dissolution of oxide or passive layers on its surface, resulting in increased current with each cycle. This behavior is crucial for capacitor applications, as it contributes to extended electrode service life [18,20].

CV at various scan rates (10–50 mV/s) was also performed to investigate reaction kinetics. The C_a value was calculated as 1500 mF/cm^2 at a scan rate of 10 mV/s. As the scan rate increased, the current through the system also increased, as shown in Figure 4.15c. The relationship between anodic peak current and scan rate is presented in Figure 4.15d, where the slope of the curve, representing the b value, was determined to be 0.65. For this porous electrode, the b value of 0.65 suggests that both capacitive and faradaic mechanisms are involved.

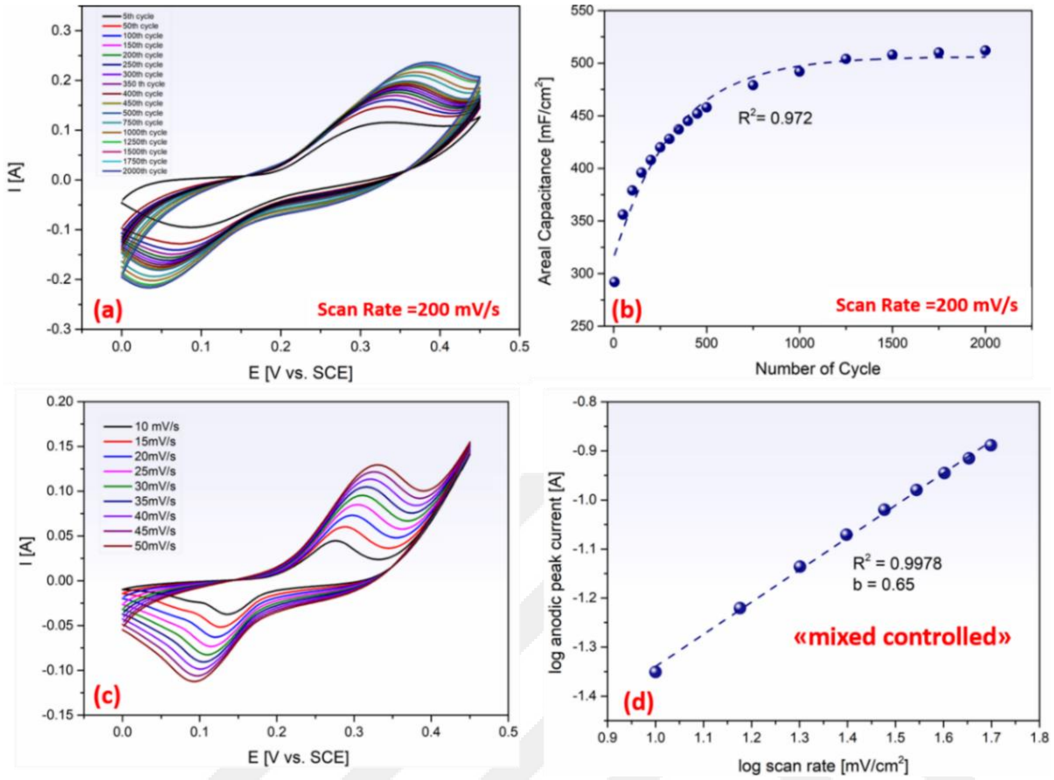

Figure 4.15 : a) Cyclic voltammogram of Ni_xB_y disc at 200 mV/s scan rate up to 2000 cycles, b) Non-linear fitting of the capacitance increments, c) cyclic voltammogram obtained at different scan rates (10-50 mV/s), d) log anodic peak current vs scan rate diagram.

To further investigate electrode behavior, GCD experiments were performed within a potential window of 0 to 0.45 V and a current density range of 0.01 to 0.1 A/cm^2. As shown in Figure 4.16, the resulting curves exhibited asymmetrical triangular shapes. This asymmetry indicates that the charge and discharge times are not identical, a characteristic feature of pseudocapacitive behavior [142]. The energy (E_a) and power density (P_a) values were calculated using equations 4.5 and 4.6, respectively, where C_a represents areal capacitance, V is the potential window, A is the geometric surface area, and t_d is the discharge time. Based on these calculations, the energy density and power density of the produced electrode were determined to be 57.5 mWh/cm^2 and 3450 mW/cm^2 at 0.01 A/cm^2, respectively. The relative energy and power densities from similar studies [111,136,143–148], along with the present results, are presented in the Ragone plot (Figure 4.17). The performance of the synthesized Ni_xB_y electrode surpasses that of previously reported electrodes. A summary of the electrochemical performance of the Ni_xB_y disc electrode is provided in Table 4.6.

$$Ea = \frac{1/2 \times Ca \times V^2}{3.6} \tag{4.5}$$

$$Pa = \frac{3600 \times Ea}{td} \tag{4.6}$$

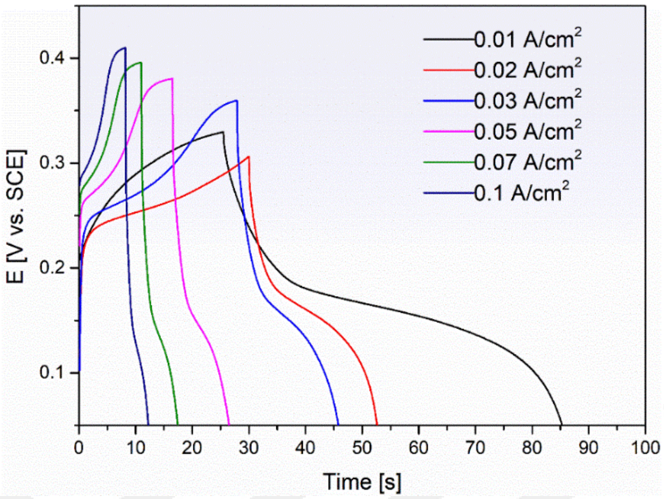

Figure 4.16 : GCD curves of synthesized Ni_xB_y disc at different current densities.

Table 4.6 : The electrochemical performance of Ni_xB_y disc electrode.

Property	**Value**
Areal capacitance (Ca)	520 mF/cm^2, at 200 mV/s
Areal capacitance (Ca)	1500 mF/cm^2, at 10 mV/s
Energy density (Ea)	57.5 mWh/cm^2, at 0.01 A/cm^2
Power density (Pa)	3450 mW/cm^2, at 0.01 A/cm^2

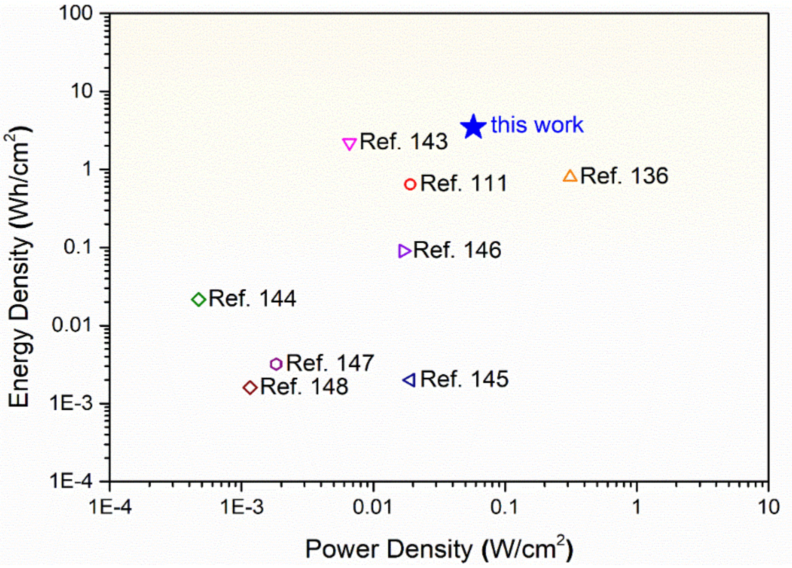

Figure 4.17 : Ragone plot for the comparison of resemble studies.

XRD analysis was conducted to examine changes in electrode structure following electrochemical testing, and phase quantities were determined using the Rietveld method (Figure 4.18). The peak intensity of Ni_4B_3 decreased, whereas those of NiB, Ni_2B, and Ni_3B increased. Quantitative analysis indicated that, compared to initial values (see Figure 4.11c and Figure 4.18), the proportions of Ni_4B_3 and NiB decreased to 43% and 4%, respectively, while Ni_2B and Ni_3B increased to 38% and 15%. These results suggest that, following faradaic reactions (4.7 and 4.8), the volumes of boron-rich phases declined as Ni-rich borides became more prevalent. This trend is attributed to oxidation reactions, as confirmed by surface analyses of electrochemically tested Ni-boride electrodes (Figure 4.19). After 2000 cycles of cyclic voltammetry (CV), a network structure formed around the boride particles as a result of nickel oxide formation.

$$\text{Anodic R.: } Ni_xB_y + 3\delta O^- + \delta H_2O \rightarrow Ni_{(x-\delta)}B_{(y-\delta)} + \delta NiOH + \delta[HBO_3]^- + 2\delta e^- \quad (4.7)$$

$$\text{Cathodic R.: } 2\delta OH^- + 2\delta e^- \rightarrow \delta H_{2(g)} + 2\delta O^{2-} \quad (4.8)$$

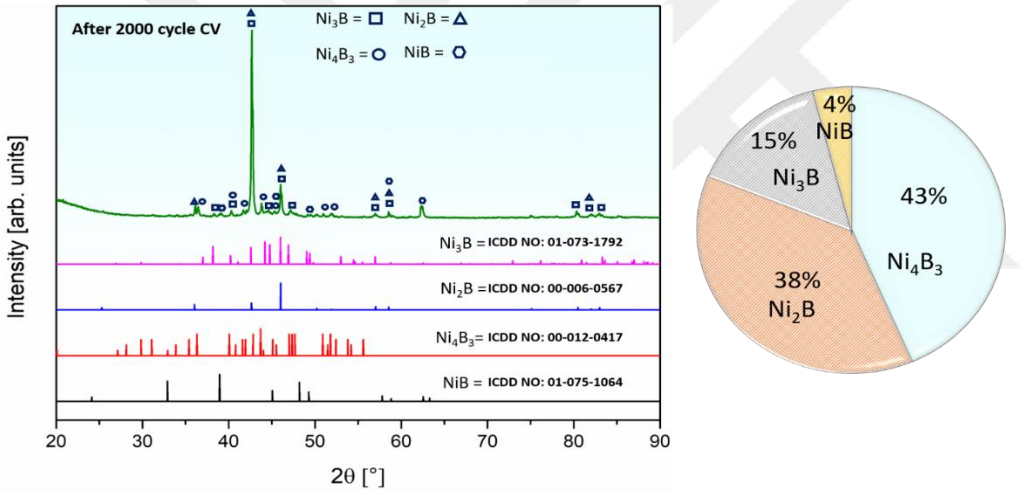

(a) (b)

Figure 4.18 : a) XRD pattern, b) Rietveld analysis of Ni_xB_y disc after 2000 cycles of CV.

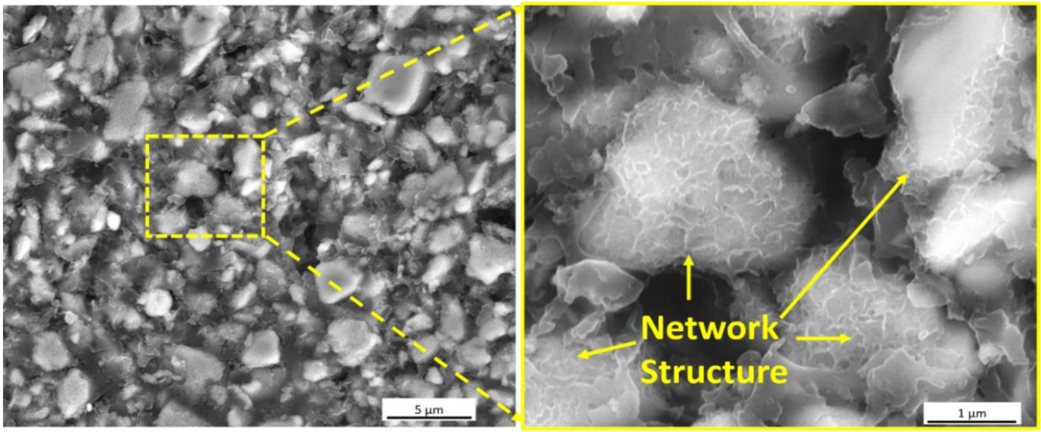

Figure 4.19 : SEM micrograph of Ni_xB_y disc after 2000 cycles of CV.

4.3 Structural and Electrochemical Properties of Flat Cobalt Boride Electrodes

To investigate the electrochemical behaviour of the cobalt boride (Co_xB) electrodes, 99.6% purity of cobalt substrates were borided via CRTD-Bor process at 950 °C and 200 mA/cm^2 for 15 min. In the XRD pattern of the borided sample recorded under Cu-K_α radiation revealed the presence of cobalt borides as CoB, Co_2B and Co_3B (Figure 4.20a). The total boride layer was measured as nearly 80 µm from the cross-sectional SEM image (Figure 4.20b). Figures 4.20c and 4.20d show the EPMA-WDS analysis results of the sample subjected only to 15 min boriding. As observed, the WDS analysis from points 1, 2, 3, and 4 indicates the presence of the Co_2B phase with the cobalt and boron composition of ~ at.% 62-65 and ~ at.% 35-38, respectively. These values were detected as ~ at.% 69-71 for cobalt and ~ at.% 29-31 for boron from points 4, 5, 6, and 7 that indicating a decreasing boron content from the surface towards the matrix. In order to observe the distribution of cobalt and boron towards the matrix, EPMA mapping analysis was also applied. As expected, the boron content is higher and the cobalt content is lower in the boride layer. When the dual-phase boride layer was examined, it was observed that the boron content was higher in the outermost layer compared to the second layer, whereas cobalt exhibited the opposite behavior, which is consistent with the results obtained from the WDX analysis.

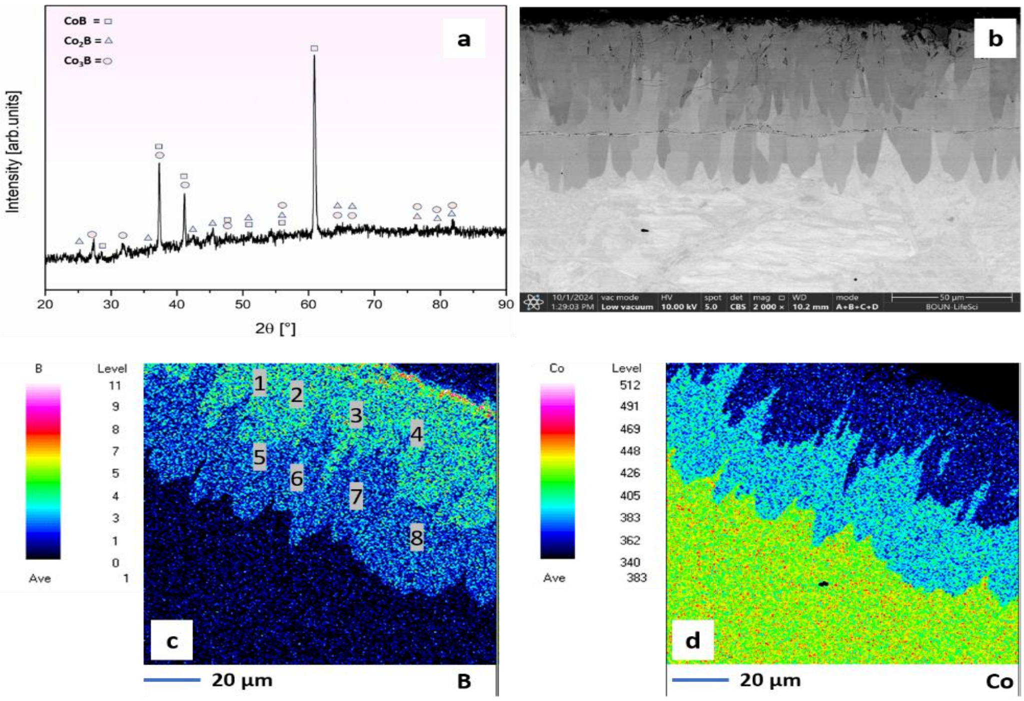

Figure 4.20 : a) XRD pattern, b) SEM micrograph and c) EPMA mapping analysis of cobalt boride plate,[950 °C and 200 mA/cm2 for 15 min.].

To investigate the electrochemical behavior of the cobalt boride specimen was subjected to CV. Initially, the 2000th cycle of CV was performed to examine the areal capacitance under long cycling conditions (Figure 4.21a). Subsequently, different scan rates were applied to study the system's kinetics (Figure 4.21b). The CV curves revealed two oxidation and two reduction peaks, indicating that two main redox reactions dominate the system. Although the potential range is wider (-0.5-0.5V) compared to the nickel boride specimens (0-0.45V) studied in sections, the current measured in the system was significantly lower. This difference impacts the areal capacitance of the cobalt boride surface; after 2000th cycle of CV, 55 mF/cm2 was measured (at 200 mV/s scan rate).

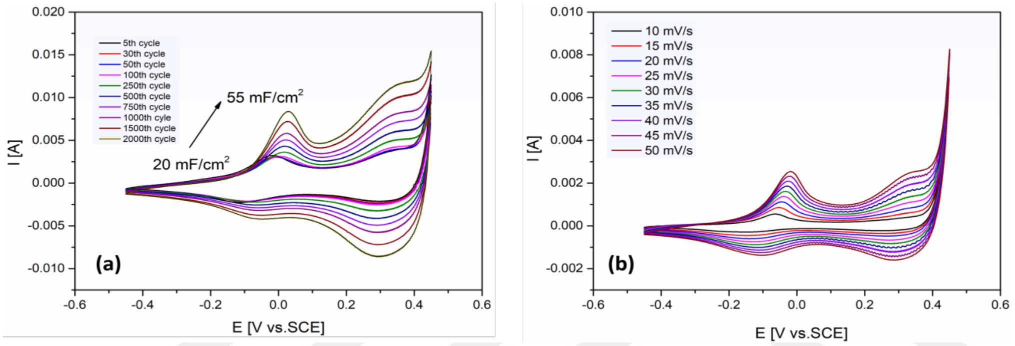

Figure 4.21 : CV curves of the flat cobalt boride surfaces (a) for multiple cycles and (b) at different scan rates.

GCD curves of the flat borided cobalt surfaces are given in Figure 4.22a at different current densities, showing typical pseudocapacitive behavior with assymetrical triangles. After EIS analyses, the resulting Nyquist diagram shown in Figure 4.22b explains the low capacitance values from the perspective of electrode kinetics and ion transport. The approximate cut-off of the Z' distribution in the high-frequency region of the curve by a very small value indicates that the ohmic resistance (Rs) formed by the solution and the electrode/collector section is the limit, and therefore the performance filter is not essentially due to series resistance. Accordingly, the broadening of the Z′ and −Z″ values, which are largely directed to the right and upward in the mid-low frequencies of the spectrum, indicates that the charge transfer and/or ion coupling within the electrode is compressed; i.e., polarization is increased. This is consistent with testing a single-surface electrode with a low specific surface area, such as a flat and compact boride layer, and paves the way for limiting the capacitive contribution and thus obtaining low capacitance values due to the activation of the active parts of the electrolyte.

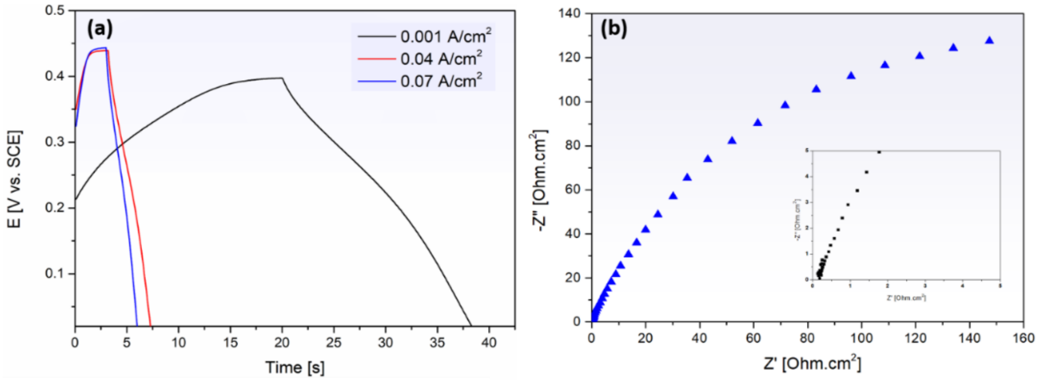

Figure 4.22 : (a) GCD curves and (b) Nyquist diagram of the flat cobalt boride surfaces.

4.4 Structural and Electrochemical Properties of Co/Co$_x$B Electrodes

XRD analysis of the synthesized powders at current densities of 200 mA/cm^2 and 600 mA/cm^2 is presented in Figure 4.23a. The dominant phases are metallic cobalt (cubic-Co) and Co$_3$B. A distinct peak splitting at 2θ = 52.2° indicates the presence of the Co$_3$B phase. The magnified XRD pattern in Figure 4.23b, focusing on 2θ = 50–55°, reveals that the most intense peaks correspond to cubic Co and Co$_3$B, supporting the coexistence of multiple phases. Increasing the synthesis current density to 600 mA/cm^2 results in the disappearance of a strong cobalt peak at 62° and the emergence of additional peaks, confirming the presence of mixed cobalt boride phases, including CoB, Co$_2$B, and Co$_3$B, along with a minor amount of metallic cobalt. The relatively strong Co diffractions observed in all XRD patterns are attributed to the overshadowing effect of metallic cobalt under Co-K$_\alpha$ radiation, which suppresses the intensity of the boride peaks [149,150].

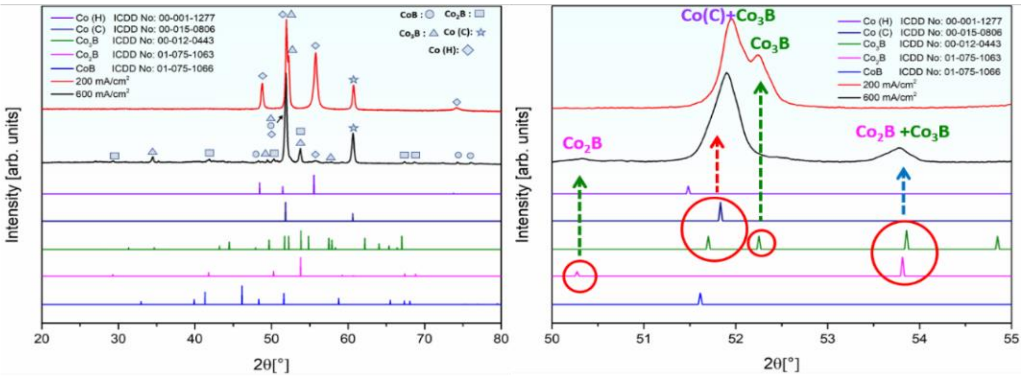

(a) (b)

Figure 4.23 : a) XRD patterns and b) magnified region of patterns of Co/Co$_x$B powders synthesized at current densities of 200 and 600 mA/cm^2 [900 °C, 1h at low carbon steel substrate].

To estimate probable phase formation during electrolysis, the relationship between the Gibbs free energy of formation (ΔG) and temperature was examined. As shown in Figure 4.24a, CoB exhibits the most thermodynamically stable configuration, possessing the lowest ΔG value (-86383.2 J/mole), followed by Co_2B and Co_3B. However, molten salt electrolysis is a non-spontaneous process governed by an external power source, which requires that phase formation occurs under the influence of the applied potential rather than solely by thermodynamic favorability [151,152]. Therefore, the electrode (cell) potentials (E) were determined using the thermodynamic relationship $\Delta G = -nEF$, where n *is* the number of electrons transferred, E is the cell potential, and F is the Faraday constant. The calculated variation in potential for phase formation with changing temperature (Figure 4.24b) indicates that Co_3B requires the lowest voltage among the cobalt borides, suggesting its preferential formation under the applied conditions. This theoretical approach corroborates the results obtained from XRD analysis.

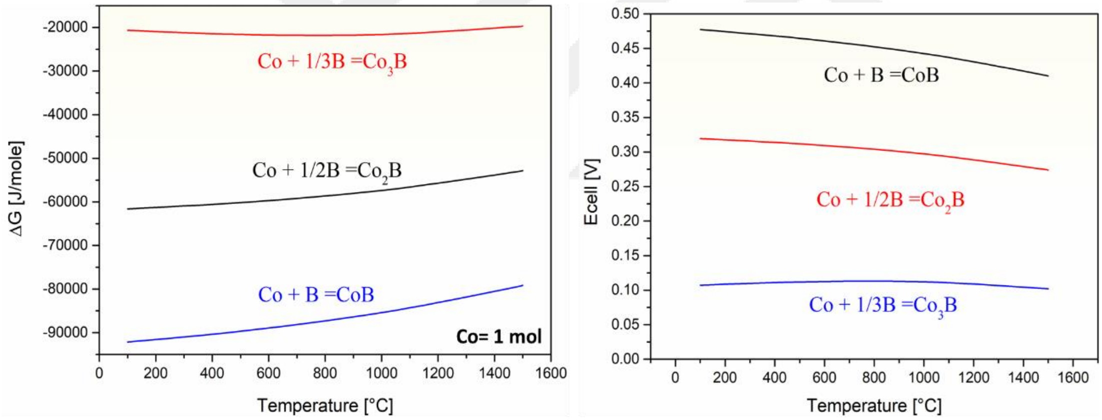

(a) (b)

Figure 4.24 : a) Gibbs free energy variations and b) corresponding cell potentials of cobalt boride phase formation [HSC Chemistry ver. 4.1.].

SEM micrographs presented in Figure 4.25 illustrate the powder morphology and specific growth mechanisms of Co/Co_xB powders. At a current density of 200 mA/cm^2, cobalt is deposited as well-defined cubic crystals that align in a chain-like structure. A magnified image of the regions surrounding the cubes (Figure 4.25b) shows a network-like morphology of boride phases distributed around the cubic cobalt crystals. At a higher current density of 600 mA/cm^2, the distinct cubic structure is no longer observed, and the boride phases predominantly surround the skeleton formed by cobalt cubes (Figures 4.25c and 4.25d). These morphological observations indicate that higher current densities promote boron reduction and incorporation, resulting in a more complex morphological structure.

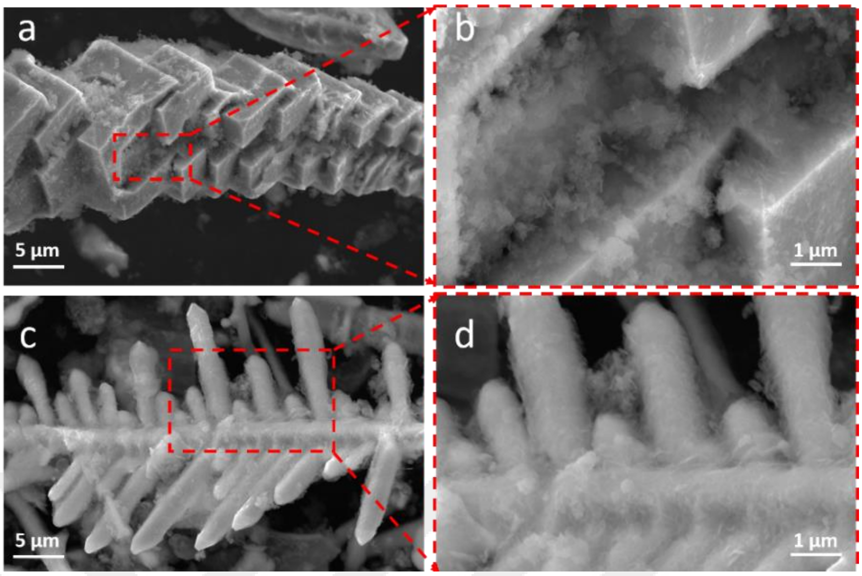

Figure 4.25 : SEM micrographs of Co/Co$_x$B composite powders synthesized at a-b) 200 mA/cm^2, c-d) 600 mA/cm^2.

The proposed growth mechanism of the Co/Co$_x$B composite powder is illustrated in Figure 4.26. XRD and SEM analyses indicate that cobalt is reduced prior to boron, resulting in sequential phase formation. Following electrolysis, the presence of cobalt within the composite structure confirms that the nucleation and growth kinetics of cobalt atoms are faster than those of boron and Co$_x$B phases. According to the proposed mechanism, cobalt ions are reduced into a cubic structure, which subsequently serves as a framework for boron reduction. After cobalt reduction, boron is reduced and deposited onto the cobalt skeleton, promoting the formation of dendritic cobalt boride arms. This distinctive growth and morphology of the Co/Co$_x$B composite structure significantly increases the surface area of the powders, which is expected to enhance electrochemical performance. In most supercapacitor electrode fabrication studies, carbon-based materials are extensively employed to improve electrical conductivity. However, the electrochemical behavior of carbon differs from that of transition metal compounds, often limiting the assessment of the intrinsic electrochemical properties of the electrode under investigation. In the present study, the inclusion of metallic cobalt provides the desired electrical conductivity and allows for the evaluation of the intrinsic electrochemical properties of the electrodes without compromising structural integrity.

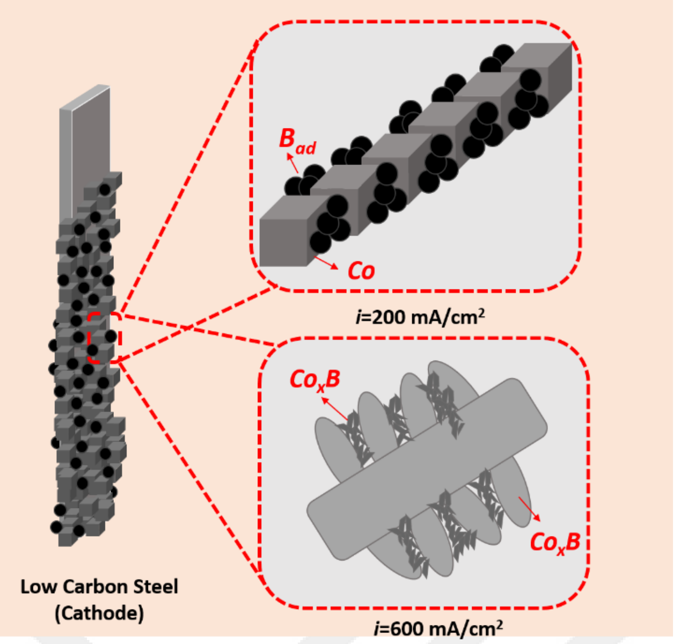

Figure 4.26 : Schematic illustration of Co and B reduction mechanism and formation of Co/Co_xB electrode.

TEM analysis was performed to corroborate the findings from XRD and SEM, as presented in Figure 4.27. The micrographs indicate that powders synthesized at both current densities (200 mA/cm^2, Figure 4.27a; 600 mA/cm^2, Figure 4.27b) possess irregular morphology in nanoscale dimensions. Selected area electron diffraction (SAED) patterns for powders produced at 200 mA/cm^2 show diffraction rings corresponding to the (111), (112), and (212) planes of the Co_3B phase, which supports the XRD results. Although XRD revealed a strong signal for metallic Co, the identification of boride phases by TEM is anticipated because TEM examines a very localized region [153,154], making it likely to detect nanoscale boride phases that accumulate around metallic cobalt cubes. For powders synthesized at 600 mA/cm^2, TEM analysis confirms the coexistence of multiple boride phases. The SAED pattern displays diffraction rings corresponding to the (222) and (332) planes (marked in white) of Co_2B, and the (111), (112), and (212) planes (marked in red) of Co_3B. Additionally, a shared ring is assigned to the (121) plane of Co_3B and the (031) plane of Co_2B. Both SAED patterns, together with high-resolution TEM (HRTEM) images, demonstrate that the powders are crystalline with nanoscale dimensions and further support the interpretation that the network structure observed around cobalt crystals in SEM images is attributable to boride compounds.

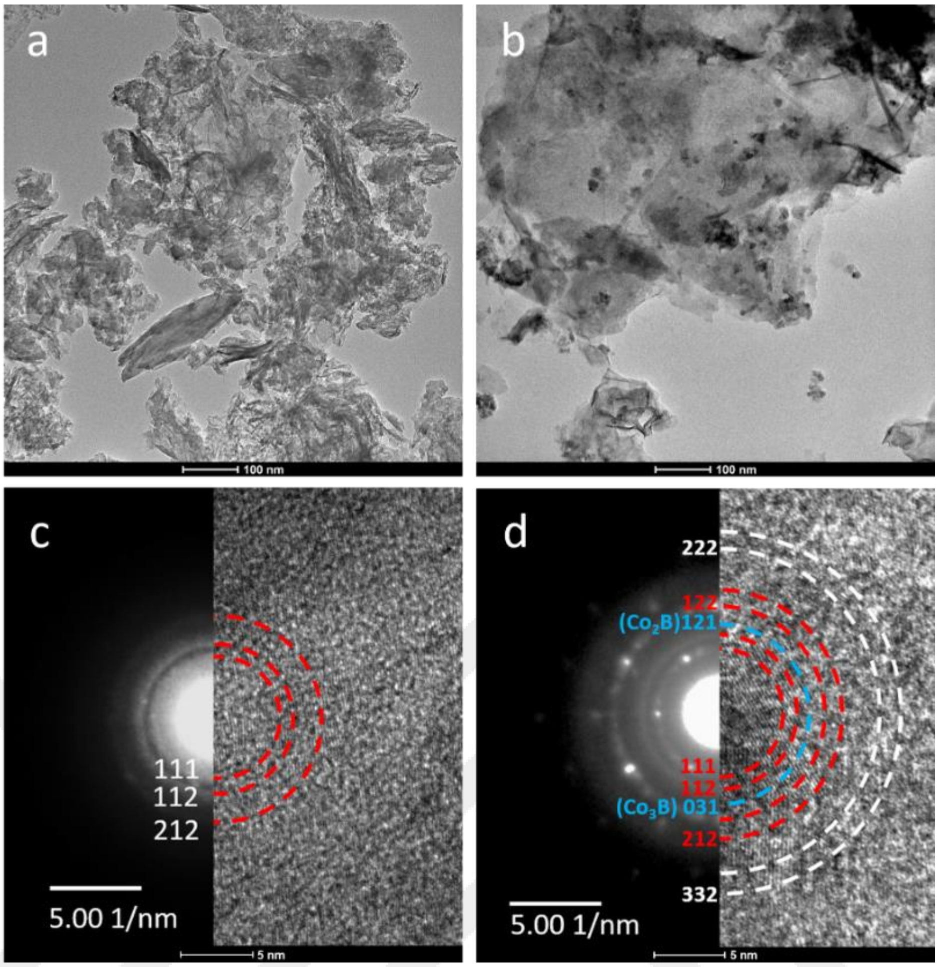

Figure 4.27 : TEM and HRTEM images with corresponding SAED patterns of Co/Co$_x$B composite powders produced at a-c) 200 mA/cm^2 and b-d)600 mA/cm^2.

Multi-cycle CV experiments were performed for up to 750 cycles on specimens produced at 200 and 600 mA/cm^2, as presented in Figures 4.28a and 4.28c, respectively. An initial increase in current density was observed until activation of the electrode surface occurred, which is characteristic of pseudocapacitive behaviour [155,156]. In the boride-rich electrode produced at 600 mA/cm^2, the increase in areal capacitance with cycling is more pronounced, indicating greater faradaic activity during the initial stages of CV. The CV curve profiles indicate that both electrodes display pseudocapacitive characteristics with distinct peaks. Areal capacitance values were calculated from CV data recorded at 200 mV/s using equation 4.1.

The initial areal capacitances were calculated as 360 and 190 mF/cm^2 for the specimens produced at 200 and 600 mA/cm^2, respectively. After 750 cycle of CV, these values reached up to 540 and 310 mF/cm^2, corresponding to 50 and 63.2 % increase in areal capacitance, as illustrated in Figures 4.28b and 4.28d.

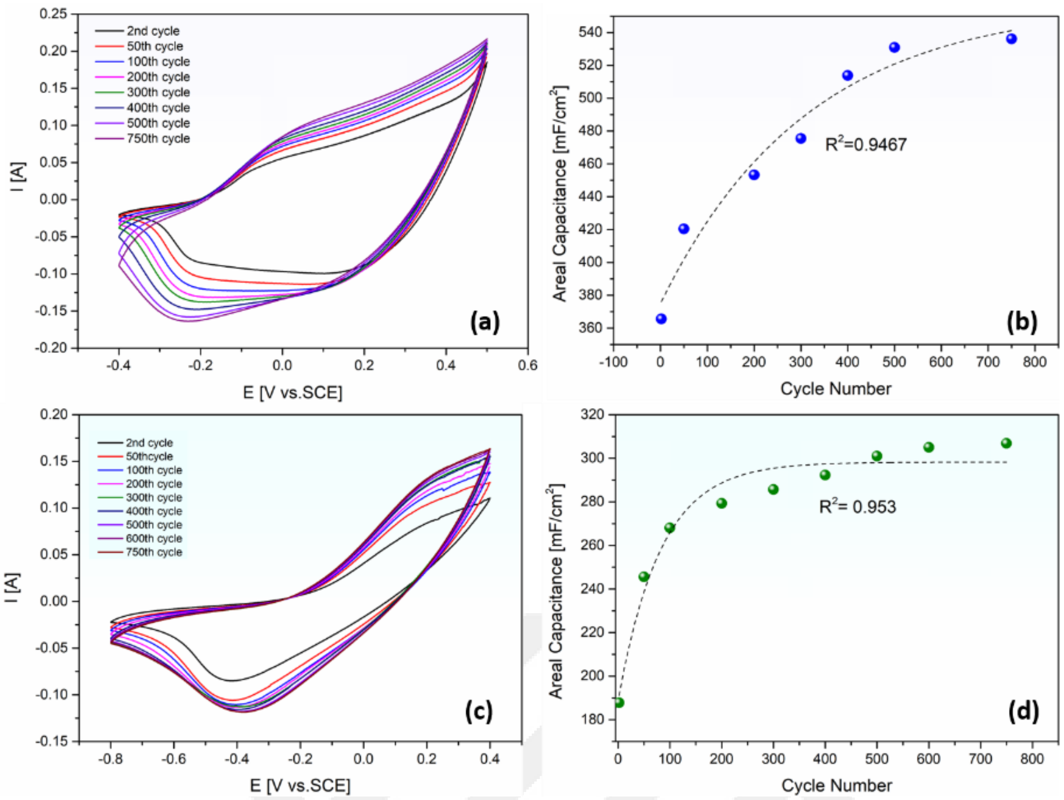

Figure 4.28 : The multi-scale CV curves and the increment in areal capacitance of the electrodes produced at a-b) 200 mA/cm^2 and c-d) 600 mA/cm^2.

CV experiments were also conducted at scan rates ranging from 10 to 100 mV/s (Figure 4.29a and 4.29c). At lower scan rates, the CV curves for both electrodes exhibited sharper redox peaks, indicating that faradaic reactions in both systems were more completely achieved at slower scan rates due to the extended time available for reaction completion [157,158]. Consequently, C_a values were determined using data obtained at 10 mV/s to ensure greater accuracy and facilitate precise comparison of electrode performance. The results showed that the electrode produced at 200 mA/cm^2 exhibited an areal capacitance of 1630 mF/cm^2, whereas the electrode produced at 600 mA/cm^2 demonstrated a capacitance of 1850 mF/cm^2. The potential window for the electrode produced at 200 mA/cm^2 was -0.4 to 0.5 V, while the CV for the electrode fabricated at 600 mA/cm^2 was performed between -0.8 and 0.4 V. The broader potential window observed in the boride-rich electrode suggests a more stable electrode surface. Therefore, higher energy density and improved electrode stability are anticipated for the electrode produced at 600 mA/cm^2.

The relationship between anodic peak current (i) and scan rate (v) was evaluated using the $i = a \cdot v^b$ power-law equation, where a is a constant and b represents the slope of the log(i) versus log(v) plot. The calculated b values were 0.71 and 0.68 (Figure 4.29b and

4.29d) for electrodes produced at 200 and 600 mA/cm^2, respectively, suggesting that both systems are governed by mixed capacitive-diffusive control.

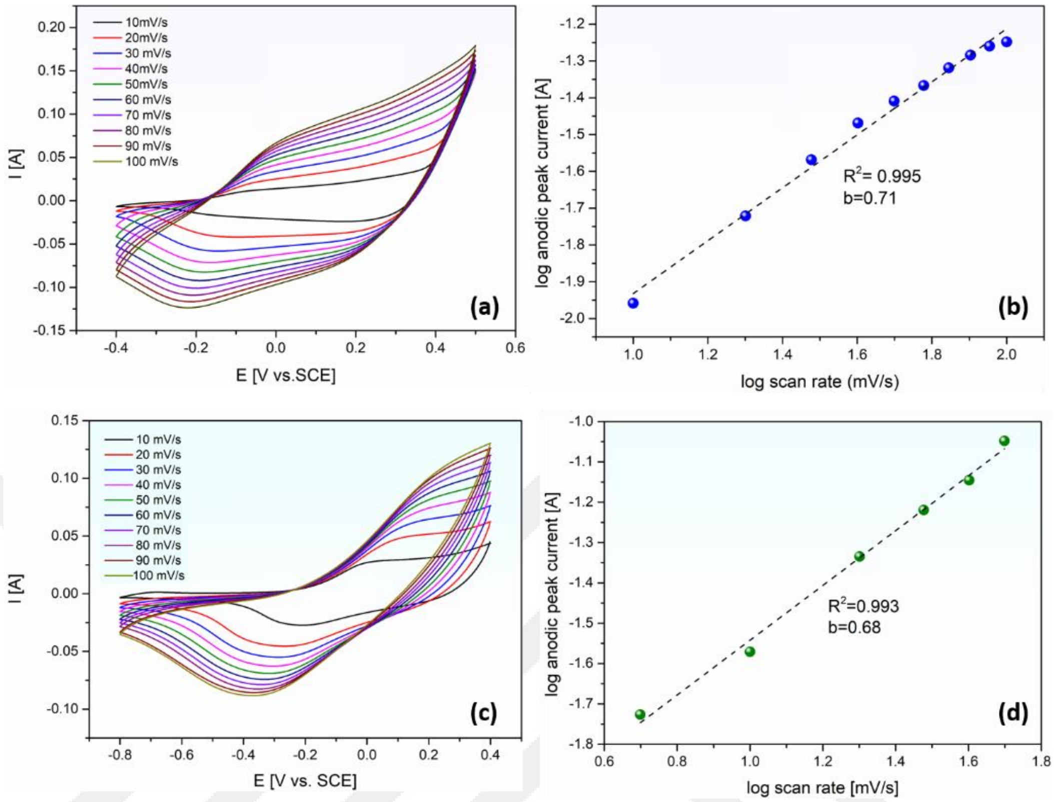

Figure 4.29 : CV curves recorded at different scan rates and corresponding log (*i*) vs. log (*v*) plots of the electrodes produced a-b) 200 mA/cm^2 and c-d) 600 mA/cm^2.

To investigate the capacitive and diffusive mechanisms of the electrodes in detail, the Trasatti method [107] was applied to CV data obtained at lower scan rates. The Trasatti model was selected over alternatives such as Dunn’s approach because both Co/CoxB electrodes display pseudocapacitive behavior, as indicated by the shift of anodic and cathodic peaks to more negative and positive potentials with increasing scan rate [109]. According to this model, C_o: 44.17% and C_i: 55.83% were determined for electrodes produced at 200 mA/cm^2 (Figure 4.30a-b), while C_o: 43.6% and C_i: 56.4% were found for those produced at 600 mA/cm^2 (Figure 4.30c-d). These findings indicate that both electrodes exhibit a mixed control mechanism, consistent with the b-value calculations.

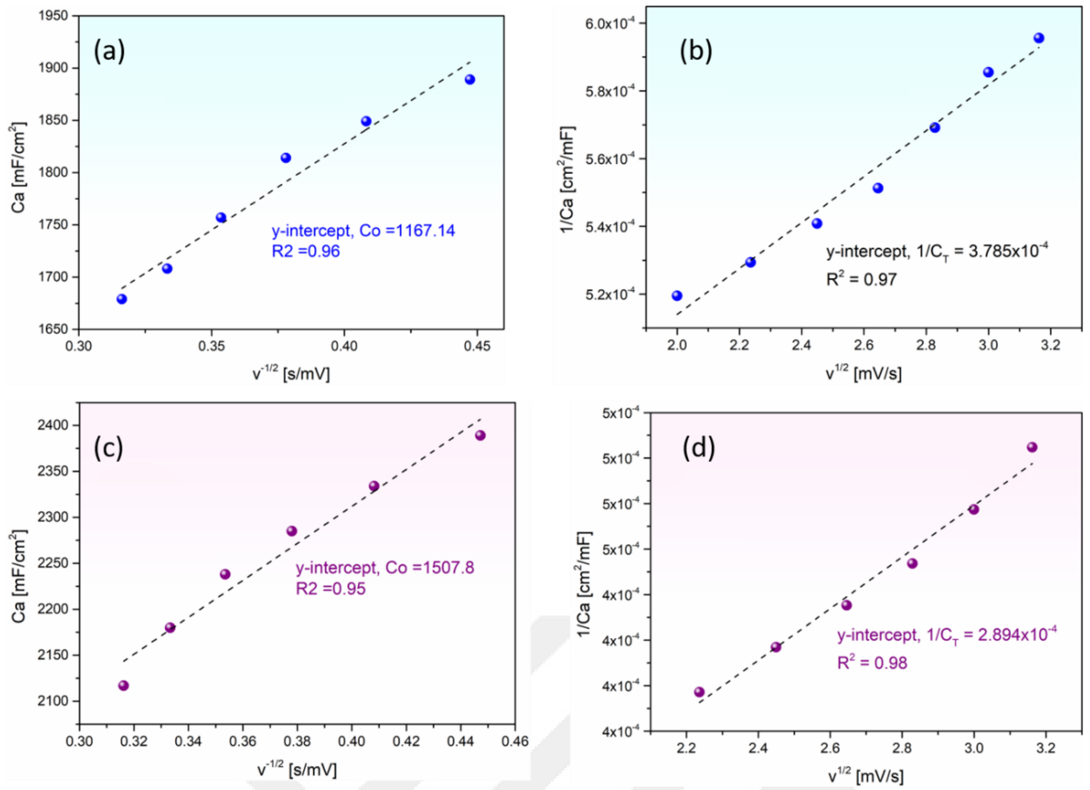

Figure 4.30 : Trasatti approach for electrodes produced at a-b) 200 mA/cm^2 and c-d) 600 mA/cm^2.

To further evaluate the electrochemical performance of the fabricated electrodes, GCD experiments were conducted. The GCD curves (Figure 4.31a-b) obtained at various current densities exhibited an asymmetric shape, which supports the pseudocapacitive nature and indicates redox reaction-dominated behavior of the electrodes [115]. The charge storage capability of the electrodes was calculated via following equation 4.9, where i is the current density, t_d is the discharge time V is the potential and S is the geometric surface area. Calculations showed that the areal capacitance of the electrode produced at 200 mA/cm^2 was 2900 mF/cm^2, while the boride-rich electrode produced at 600 mA/cm^2 exhibited a value of 4180 mF/cm^2. The GCD test is regarded as more accurate than CV, as it provides precise charge and discharge capacities of the electrode under constant current [127,159]. Therefore, in this study, the areal capacitance values determined from GCD were considered more reliable. Additionally, the energy and power densities of each electrode were calculated using equations 4.5 and 4.6, respectively. The electrode produced at 200 mA/cm^2 demonstrated energy and power densities of 48 mWh/cm^2 and 2300 mW/cm^2, respectively, while the boride-rich electrode produced at 600 mA/cm^2 achieved 78 Wh/cm^2 and 2800 mW/cm^2. These results indicate that the presence of boride phases enhances both the energy storage capacity and power density of the electrochemical system.

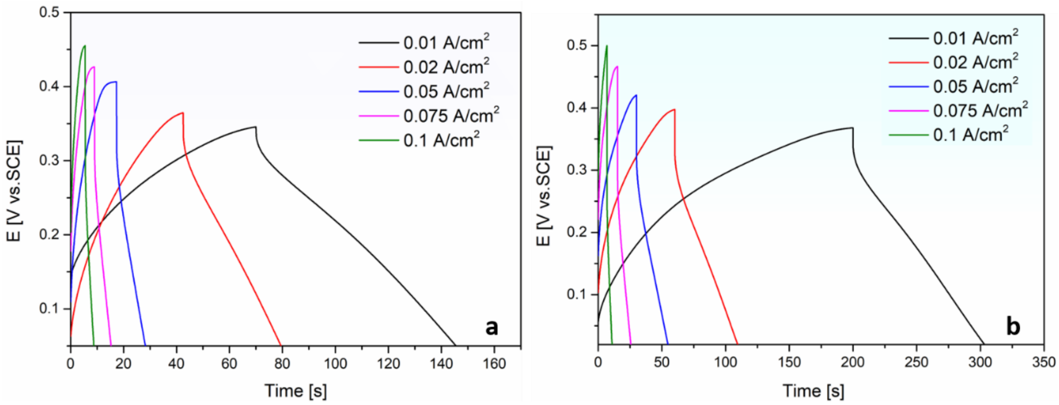

Figure 4.31 : GCD curves of Co/Co_xB composite electrodes produced at a)200 mA/cm^2 and b) 600 mA/cm^2.

$$C_a = \frac{ixt_d}{VXS} \tag{4.9}$$

LSV was conducted on both electrodes at the anodic side to evaluate the electrocatalytic behavior of the synthesized Co/Co_xB composite electrodes and further clarify their electrochemical performance (Figure 4.32). The electrode fabricated at 600 mA/cm^2, which contained a higher concentration of multiple boride phases, exhibited greater current density and lower overpotential. This result confirms the enhanced catalytic activity of the boride-rich electrode compared to the others [159]. These findings are consistent with the overall electrochemical results obtained for the investigated electrodes.

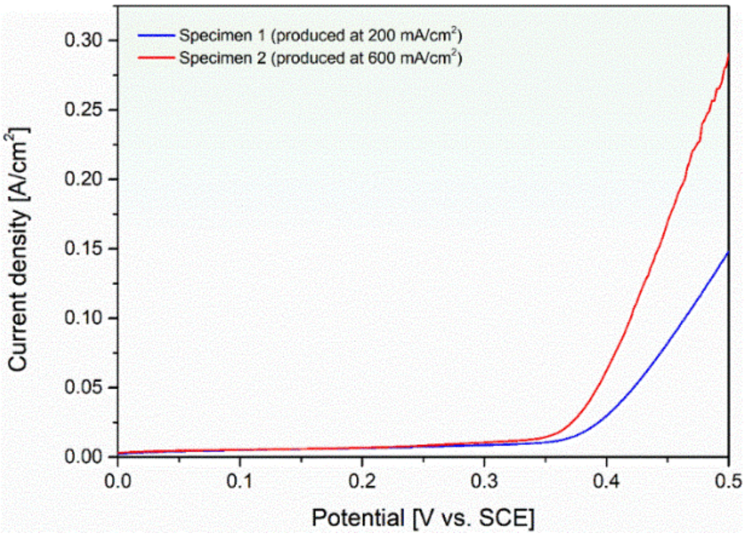

Figure 4.32 : The anodic LSV curve of produced Co/Co_xB electrodes at different current densities (200 and 600 mA/cm^2).

This study diverges from the conventional approach in the literature by evaluating performance based on C_a. The production method employed restricts redox reactions from occurring throughout the entire bulk structure of the electrodes. Because the electrolyte does not fully penetrate the entire cross section, mass-based calculations were excluded to prevent potentially misleading or unreliable results. Consequently, C_a was selected as a more accurate and reliable evaluation parameter. The C_a of the fabricated Co/Co$_x$B electrodes was compared with values reported for other cobalt-based materials, such as cobalt oxides and sulfides. As shown in Figure 4.33, selected literature reports presenting both specific [27,160,169,170,161–168] and areal capacitance [24,25,171–174] values indicate that the Co/Co$_x$B composite electrodes produced in this study exhibit significantly higher performance than those in comparable studies.

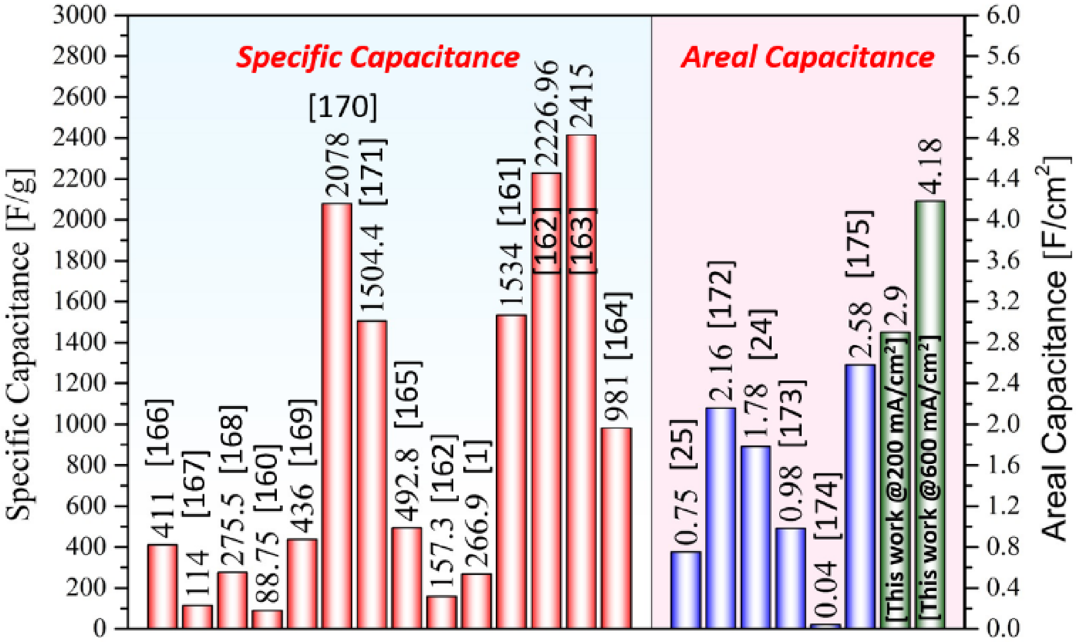

Figure 4.33 : Literature report for the specific (C_s) and areal (C_a) capacitance values of Co-based electrodes.

5. CONCLUSIONS AND RECOMMENDATIONS

This thesis study explores the electrochemical characteristics of nickel and cobalt boride electrodes produced through a fast, novel and environmentally firiendly molten salt electrolysis method. While nickel boride flat and foam surfaces and flat cobalt boride were produced via CRTD-Bor method, Co/Co_xB composite electrodes were fabricated co-deposition assisted molten salt electrolysis.

- In the first part of the thesis, the geometrical (flat and foam geometry) influence of electrodes on capacitance behavior was examined in detail. The structural characterizations released the produced electrodes composed of NiB, Ni_4B_3, and Ni_2B. NiB phase grew unevenly on the top surface, while Ni_4B_3 was the main phase. The reaction kinetics were determined via the Trasatti Method and it was found that the capacitive contribution was higher on the flat (capacitive contribution, C_o:71%), whereas the dominating mechanism is diffusive in foam form (diffusive contribution, C_i: 59.4%). The electrochemical behavior of the produced electrodes was assessed through cyclic voltammetry, galvanostatic charge-discharge, and impedance spectroscopy. The capacitances of the electrodes were calculated as 478 and 1385 mF/cm² for flat and foam specimens respectively at 10 mV/s with CV experiments. The possible mechanism behind the faradaic reactions was investigated via XPS and FTIR analyses conducted both before and after CV for two different geometries. The obtained results exhibited that the faradaic reactions were related to the formation of Ni-O bonds due to oxygen saturation on the defective and active areas on the surfaces.
- In the second part of the thesis, porous Ni-boride electrodes (Ni_xB_y; $4 \geq x \geq 1$, $3 \geq y \geq 1$) were fabricated. The structural characterizations revealed the mixed nature of the electrode composed of NiB, Ni_4B_3, Ni_2B, and Ni_3B, where Ni_4B_3 was the main phase. The synthesized boride powders were cold pressed to give the disc shape, and their electrochemical properties were investigated through CV and GCD techniques. During CV experiment, it was observed the

increasing tendency of areal capacity with the number of cycles. This behavior is a crucial characteristic desired in capacitor application. The areal capacity tremendously enhanced up to 1000 cycles and this sharp increasing trend slowed down afterward. The maximum Ca value was determined as 520 mF/cm^2 after the 2000 cycle. Additional CV tests at different scan rates were conducted to determine reaction kinetics, and it was deduced that the electrode works with the principle of both capacitive (EDLC) and faradaic (pseudocapacitors) according to the found b value; 0.65. The maximum Ca value was calculated as 1500 mF/cm^2 at 10 mV/s obtained via CV. GCD results confirmed the pseudocapacitive nature of the electrode by exhibiting asymmetrical charge-discharge behavior. The energy and power density values were determined as 57.5 mWh/cm^2 and 3450 mW/cm^2 at 0.01 A/cm^2. The power density of the produced porous Ni-boride electrode was 3-fold higher compared to the average findings in the open literature. Considering all outcomes obtained in the current work, the porous Ni-boride electrodes are a remarkable candidate for supercapacitor applications.

- In the third part of the thesis, the boriding of flat cobalt surfaces was conducted. The EPMA-WDX results indicated that approxiametely 80 µm thick dual phase of boride layer was formed on the surface and mapping analysis depicted the formation of Co_2B near surface. CV revealed that two oxidation and reduction peaks supporting two dominant faradaic reactions. Despite this, the current passing through the system was quiate low and resulted in 55 mF/cm^2 areal capacitance after 2000 cycles at 200 mV/s. The Nyquist curve revealed that altough there is no solution resistance limitation in low frequency region, the impedance at the mid-frequency region restiricts the charge transfer or ion transport.

- Last part involves synthesis of Co/Co_xB composite powders . In order to elucidate the effect of different type and amount of boride phases on electrochemical performance of the powders, two different current densities, 200 and 600 mA/cm^2, were applied. Following the electrolysis, the synthesized powders were mechanically ground via ball mill and compacted to get disc shape by cold press. The structural analysis depicted that both powders compose of mixed phases of Co and Co_xB. Specifically, at 200 mA/cm^2, the powders comprised of metallic Co and Co_3B, while the one produced at 600 mA/cm^2 contained Co, CoB, Co_2B and Co_3B. CV tests were performed to 750 cycles at a scan rate of 200 mV/s, revealing that electrode produced at 200 mA/cm^2 demonstrated a 50% increase in areal capacitance whereas the other electrode exhibited 63.2% rise. Trasatti model confirmed that both electrodes work under mixed control (both capacitive (C_o) and diffusive (C_i)); C_o: 44.2% - C_i:55.8% and C_o: 43.6% - C_i: 56.4% for the electrodes produced at 200 and 600 mA/cm^2, respectively. Areal capacitance values were determined via GCD test as 2900 mF/cm^2 and 4180 mF/cm^2 for the electrodes fabricated at 200 and 600 mA/cm^2, respectively. Energy and power densities were calculated as 48 mWh/cm^2 and 2300 mW/cm^2 for the electrode produced at 200 mA/cm^2: 78 mWh/cm^2 and 2800 mW/cm^2 for that of synthesized at 600 mA/cm^2. LSV results demonstrated that electrocatalytic activity of the Co/Co_xB composite electrode produced at 600 mA/cm^2 is higher than that of fabricated at 200 mA/cm^2.

- For the future studies, it is rocommeded to produce bimetallic borides of nickel and cobalt to combine the superior properties of both elements and to conduct the electrochemical tests to understand the electrochemical mechanisms behind the bimetallic boride electrodes. Furhermore, the performance of electrodes can be demonstrated in practice by assembling symmetrical or asymmetrical supercapacitors using the produced electrodes.

REFERENCES

[1] **Aydın, H., Kurtan, Ü., Üstün, B., Koç, S.N., Akgül, E., and Demir, M.** (2023) A review on the recent advancement of metal-boride derived nanostructures for supercapacitors. *Journal of Energy Storage*. *72* (PA), 108306.

[2] **Arslan-Kaba, M., Timur, S., and Kartal Sireli, G.** (2024) Evaluating the mechanism and the capacitive properties of nickel boride electrodes for supercapacitor applications. *Journal of Energy Storage*. *99* (PA), 113299.

[3] **Zhang, J., Yan, X., Cheng, Z., Han, Y., Zhang, Y., and Dong, Y.** (2024) Applications, prospects and challenges of metal borides in lithium sulfur batteries. *Journal of Colloid and Interface Science*. *657* (November 2023), 511–528.

[4] **Khedimallah, A., Zayani, W., Dabaki, Y., Khaldi, C., Lamloumi, J., El-Kedim, O., et al.** (2023) Electrochemical study of the LaNiO3 perovskite-type oxide used as anode in nickel-metal hydride batteries. *Solid State Sciences*. *146* (September), 107338.

[5] **Paksoy, A., Buldu-Akturk, M., Arabi, S., Erdem, E., and Balcı-Çağıran, Ö.** (2023) Synthesis and capacitive performance of ZrB2 and its composites as supercapacitor electrodes. *Solid State Sciences*. *142* (January),.

[6] **Winter, M. and Brodd, R.J.** (2004) What are batteries, fuel cells, and supercapacitors? *Chemical Reviews*. *104* (10), 4245–4269.

[7] **Poonam, Sharma, K., Arora, A., and Tripathi, S.K.** (2019) Review of supercapacitors: Materials and devices. *Journal of Energy Storage*. *21* (January), 801–825.

[8] **Libich, J., Máca, J., Vondrák, J., Čech, O., and Sedlaříková, M.** (2018) Supercapacitors: Properties and applications. *Journal of Energy Storage*. *17* (March), 224–227.

[9] **González, A., Goikolea, E., Barrena, J.A., and Mysyk, R.** (2016) Review on supercapacitors: Technologies and materials. *Renewable and Sustainable Energy Reviews*. *58* 1189–1206.

[10] **Wang, Y., Guo, J., Wang, T., Shao, J., Wang, D., and Yang, Y.W.** (2015) Mesoporous transition metal oxides for supercapacitors. *Nanomaterials*. *5* (4), 1667–1689.

[11] **Cao, X., Wang, X., Cui, L., Jiang, D., Zheng, Y., and Liu, J.** (2017) Strongly coupled nickel boride/graphene hybrid as a novel electrode material for supercapacitors. *Chemical Engineering Journal*. *327* 1085–1092.

[12] **Kumar, V., Aepuru, R., Faizal, A., and Panda, H.S.** (2022) Elucidating the pseudocapacitive mechanism of ternary Co-Ni-B electrodes–Towards miniaturization and superior electrochemical performance for building outmatched supercapacitors. *Electrochimica Acta*. *409* (November 2021), 140003.

[13] **Yang, F., Ma, X.J., Yang, J.L., Liu, J.H., Chen, B., Liu, X.Y., et al.** (2024) Clay minerals modified nickel boride for electrochemical supercapacitor electrode application. *Applied Clay Science*. *251* (November 2023), 107305.

[14] **Gao, P., Yang, S., Xue, Z., Liu, G., Zhang, G., Wang, L., et al.** (2012) High energy ball-milling preparation of Co-B amorphous alloy with high electrochemical hydrogen storage ability. *Journal of Alloys and Compounds*. *539* 90–96.

[15] **Braunschweig, H. and Colling, M.** (2001) Transition metal complexes of boron - Synthesis, structure and reactivity. *Coordination Chemistry Reviews*. *223* (1), 1–51.

[16] **Shveikin, G.P. and Ivanovskii, A.L.** (1994) The chemical bonding and electronic properties of metal borides. *Russian Chemical Reviews*. *63* (9), 711–734.

[17] **Hong, J., Mutalik, S., Miola, M., Gerlach, D., Mehrabi K, R., Ahmadi, M., et al.** (2023) Nickel Boride (NixB) Nanocrystals: From Solid-State Synthesis to Highly Colloidally Stable Inks. *Chemistry of Materials*. *35* (4), 1710–1722.

[18] **Lewandowski, M., Bartoszewicz, M., Jaroszewska, K., and Djéga-Mariadassou, G.** (2022) Transition metal borides of Ni-B (Co-B) as alternative non-precious catalytic materials: Advances, potentials, and challenges. Short review. *Journal of Industrial and Engineering Chemistry*. *116* 75–98.

[19] **Li, Y., Zhang, J., Chen, Z., and Chen, M.** (2022) Nickel-based materials: Toward practical application of the aqueous hybrid supercapacitors. *Sustainable Materials and Technologies*. *33* (May),.

[20] **Ahmad, R. and Shah, M.A.** (2023) Hydrothermally synthesised nickel oxide nanostructures on nickel foam and nickel foil for supercapacitor application. *Ceramics International*. *49* (4), 6470–6478.

[21] **Vidhyadharan, B., Zain, N.K.M., Misnon, I.I., Aziz, R.A., Ismail, J., Yusoff, M.M., et al.** (2014) High performance supercapacitor electrodes from electrospun nickel oxide nanowires. *Journal of Alloys and Compounds*. *610* 143–150.

[22] **Dhas, S.D., Maldar, P.S., Patil, M.D., Waikar, M.R., Sonkawade, R.G., and Moholkar, A. V.** (2022) Sol-gel synthesized nickel oxide nanostructures on nickel foam and nickel mesh for a targeted energy storage application. *Journal of Energy Storage*. *47* (November 2021), 103658.

[23] **AbdelHamid, A.A., Yang, X., Yang, J., Chen, X., and Ying, J.Y.** (2016) Graphene-wrapped nickel sulfide nanoprisms with improved performance for Li-ion battery anodes and supercapacitors. *Nano Energy*. *26* 425–437.

[24] **Han, Y., Cui, J., Yu, Y., Chao, Y., Li, D., Wang, C., et al.** (2022) Efficient Metal-Oriented Electrodeposition of a Co-Based Metal-Organic Framework with Superior Capacitive Performance. *ChemSusChem*. *15* (14), 1–8.

[25] **Kwak, J.H., Lee, Y.W., and Bang, J.H.** (2013) Supercapacitor electrode with an ultrahigh Co3O4 loading for a high areal capacitance. *Materials Letters*. *110* 237–240.

[26] **Kumar, V., Aepuru, R., Faizal, A., and Panda, H.S.** (2022) Elucidating the pseudocapacitive mechanism of ternary Co-Ni-B electrodes–Towards miniaturization and superior electrochemical performance for building outmatched supercapacitors. *Electrochimica Acta*. *409* (January), 140003.

[27] **Chai, S.S., Zhang, L., Zhang, W. Bin, Bao, X., Guo, Y.W., Han, X.W., et al.** (2022) Acid etching halloysite loaded cobalt boride material for supercapacitor electrode application. *Applied Clay Science*. *218* (November 2021), 106426.

[28] **Lokhande, P.E., Chavan, U.S., and Pandey, A.** (2020) Materials and Fabrication Methods for Electrochemical Supercapacitors: Overview. Springer Singapore, .

[29] **De, P., Halder, J., Gowda, C.C., Kansal, S., Priya, S., Anshu, S., et al.** (2023) Role of porosity and diffusion coefficient in porous electrode used in supercapacitors – Correlating theoretical and experimental studies. *Electrochemical Science Advances*. *3* (1), 1–15.

[30] **Sireli, G.K.** (2016) Molten Salt Baths: Electrochemical Boriding. *Encyclopedia of Iron, Steel, and Their Alloys*. (May), 2284–2300.

[31] **Timur, S., Kartal, G., Eryilmaz, O.L., and Erdemir, A.** (2015) Ultra-fast boriding of metal surfaces for improved properties, US Patent No. 8,951,402, 2015.

[32] **Volta A.** (1800) On the electricity exited by contact. *Phil. Trans. R. Soc. 90* (December), 403–431.

[33] **Brockman, C.J.** (1927) Primary Cells A Brief Historical Sketch. *Journal of Chemical Education 4* (6), 770.

[34] **Szydło, Z.A.** (2021) Chemical Electricity. *Chemistry, Didactics, Ecology, Metrology*. *26* (1–2), 5–29.

[35] **Kurzweil, P.** (2010) Gaston Planté and his invention of the lead-acid battery-The genesis of the first practical rechargeable battery. *Journal of Power Sources*. *195* (14), 4424–4434.

[36] **Bernard, P. and Lippert, M.** (2015) Nickel-Cadmium and Nickel-Metal Hydride Battery Energy Storage, In P.T. Moseley and J. Garche (Eds.), *Electrochemical Energy Storage for Renewable Sources and Grid Balancing*, (pp. 223-251), Oxford : Elsevier B.V.

[37] **Dunn, B., Kamath, H., and Tarascon, J.M.** (2011) Electrical energy storage for the grid: A battery of choices. *Science*. *334* (6058), 928–935.

[38] **Mahmud, S., Rahman, M., Kamruzzaman, M., Ali, M.O., Emon, M.S.A., Khatun, H., et al.** (2022) Recent advances in lithium-ion battery materials for improved electrochemical performance: A review. *Results in Engineering*. *15* (May), 100472.

[39] **Kötz, R. and Carlen, M.** (2000) Principles and applications of electrochemical capacitors. *Electrochemica Acta*. *45* 2483–2498.

[40] **Lobato-Peralta, D.R., Okoye, P.U., and Alegre, C.** (2024) A review on carbon materials for electrochemical energy storage applications: State of the art, implementation, and synergy with metallic compounds for supercapacitor and battery electrodes. *Journal of Power Sources*. *617* (April),.

[41] **Zhai, Z., Zhang, L., Du, T., Ren, B., Xu, Y., Wang, S., et al.** (2022) A review of carbon materials for supercapacitors. *Materials and Design*. *221* 111017.

[42] **Conway, B.E., Birss, V., and Wojtowicz, J.** (1997) The role and utilization of pseudocapacitance for energy storage by supercapacitors. *Journal of Power Sources*. *66* 1–14.

[43] ***History of Batteries: A Timeline.*** *(2014) Retrieved December 12, 2025, from https://blog.upsbatterycenter.com/history-batteries-timeline/*

[44] **Amir, M., Deshmukh, R.G., Khalid, H.M., Said, Z., Raza, A., Muyeen, S.M., et al.** (2023) Energy storage technologies: An integrated survey of developments, global economical/environmental effects, optimal scheduling model, and sustainable adaption policies. *Journal of Energy Storage*. *72* (PE), 108694.

[45] **Rosen, M.A.** (2020) A review of energy storage types , applications and recent developments. *Journal of Energy Storage*. *27* (October 2019), 101047.

[46] **Kandhasamy, M., Duvaragan, B.K., and Kamaraj, S.** (2024) An Overview on Classification of Energy Storage Systems. *Materials for Boosting Energy Storage. Volume 2: Advances in Sustainable Energy Technologies, Part 1 - An Overview on Classification of Energy Storage Systems*. *2* 1–25.

[47] **Ragone, D. V** (1968) Review of Battery Systems for Electrically Powered Vehicles Review of Battery Systems for Electrically Powered Vehicles.

[48] **Olabi, A.G., Allam, M.A., Abdelkareem, M.A., Deepa, T.D., Alami, A.H., Abbas, Q., et al.** (2023) Redox Flow Batteries : Recent Development in Main Components , Emerging Technologies , Diagnostic Techniques , Large-Scale Applications , and Challenges and Barriers.

[49] **Mekonnen, Y.** (2016) A Review of Cathode and Anode Materials for Lithium-Ion Batteries. *SoutheastCon 2016*. (1541108), 1–6.

[50] **Borah, R., Hughson, F.R., Johnston, J., and Nann, T.** (2020) On battery materials and methods. *Materials Today Advances*. *6* 100046.

[51] **Coralli, A., Sarruf, B.J.M., De Miranda, P.E. V., Osmieri, L., Specchia, S., and Minh, N.Q.** (2019) Fuel cells, In P. E.V. de Miranda (Ed), *Science and Engineering of Hydrogen-Based Energy Technologies*, (pp. 39-122), London : Elsevier Inc.

[52] **Chukwuka, C. and Folly, K.A.** (2012) Batteries and super-capacitors. *IEEE Power and Energy Society Conference and Exposition in Africa: Intelligent Grid Integration of Renewable Energy Resources, PowerAfrica 2012*. (July), 1–6.

[53] ***Fuel Cell Basics and Benefits.*** *(2023), Retrieved December, 12, 2025, from https://www.matsusada.com/column/words-fuel_cell.html.*

[54] **Sarjeant, W.J.** (1990) Capacitors. *IEEE Transactions on Electrical Insulation*. *25* (5), 861.

[55] **Liu, W., Sun, X., Yan, X., Gao, Y., Zhang, X., Wang, K., et al.** (2024) Review of Energy Storage Capacitor Technology. *Batteries*. *10* (8),.

[56] ***Basic knowledge about capacitors.*** *(2018), Retrieved December 10, 2025, from https://industrial.panasonic.com/ww/ds/ss/technical/b2.*

[57] **Sun, J., Luo, B., and Li, H.** (2022) A Review on the Conventional Capacitors, Supercapacitors, and Emerging Hybrid Ion Capacitors: Past, Present, and Future. *Advanced Energy and Sustainability Research*. *3* (6),.

[58] **Olabi, A.G., Abbas, Q., Al Makky, A., and Abdelkareem, M.A.** (2022) Supercapacitors as next generation energy storage devices: Properties and applications. *Energy*. *248* 123617.

[59] **Karthikeyan, S., Narenthiran, B., Sivanantham, A., Bhatlu, L.D., and Maridurai, T.** (2020) Supercapacitor: Evolution and review. *Materials Today: Proceedings*. *46* 3984–3988.

[60] **Kar, K.K.** (2023) Springer series in materials science 300 handbook of nanocomposite supercapacitor materials I. .

[61] **Banerjee, S., De, B., Sinha, P., Cherusseri, J., and Kar, K.K.** (2020) Applications of supercapacitors. .

[62] **Artemov, V.** (2021) *The Electrodynamics of Water and Ice,* New York: Springer.

[63] **Bolt, G.H.** (1955) Analysis of the validity of the Gouy-Chapman theory of the electric double layer. *Journal of Colloid Science*. *10* (2), 206–218.

[64] **He, X. and Zhang, X.** (2022) A comprehensive review of supercapacitors: Properties, electrodes, electrolytes and thermal management systems based on phase change materials. *Journal of Energy Storage*. *56* (PC), 106023.

[65] **Noked, M., Okashy, S., Zimrin, T., and Aurbach, D.** (2012) Composite carbon nanotube/carbon electrodes for electrical double-layer super capacitors. *Angewandte Chemie - International Edition*. *51* (7), 1568–1571.

[66] **Sharma, P. and Bhatti, T.S.** (2010) A review on electrochemical double-layer capacitors. *Energy Conversion and Management*. *51* (12), 2901–2912.

[67] **Ren, K., Liu, Z., Wei, T., and Fan, Z.** (2021) Recent Developments of Transition Metal Compounds-Carbon Hybrid Electrodes for High Energy/Power Supercapacitors. Springer Singapore, .

[68] **Feng, L., Zhu, Y., Ding, H., and Ni, C.** (2014) Recent progress in nickel based materials for high performance pseudocapacitor electrodes. *Journal of Power Sources*. *267* 430–444.

[69] **Chodankar, N.R., Pham, H.D., Nanjundan, A.K., Fernando, J.F.S., Jayaramulu, K., Golberg, D., et al.** (2020) True Meaning of Pseudocapacitors and Their Performance Metrics: Asymmetric versus Hybrid Supercapacitors. *Small*. *16* (37), 1–35.

[70] **Costentin, C., Porter, T.R., and Savéant, J.M.** (2017) How Do Pseudocapacitors Store Energy? Theoretical Analysis and Experimental Illustration. *ACS Applied Materials and Interfaces*. *9* (10), 8649–8658.

[71] **Costentin, C. and Savéant, J.M.** (2019) Energy storage: Pseudocapacitance in prospect. *Chemical Science*. *10* (22), 5656–5666.

[72] **Kumar, N., Kim, S. Bin, Lee, S.Y., and Park, S.J.** (2022) Recent Advanced Supercapacitor: A Review of Storage Mechanisms, Electrode Materials, Modification, and Perspectives. *Nanomaterials*. *12* (20),.

[73] **Gogotsi, Y. and Penner, R.M.** (2018) Energy Storage in Nanomaterials - Capacitive, Pseudocapacitive, or Battery-like? *ACS Nano*. *12* (3), 2081–2083.

[74] **Simon, P. and Gogotsi, Y.** (2008) Materials for electrochemical capacitors *Nature Materials. 7* (11), 845–854.

[75] **Ashok Kumar, K., Pandurangan, A., Arumugam, S., and Sathiskumar, M.** (2019) Effect of Bi-functional Hierarchical Flower-like CoS Nanostructure on its Interfacial Charge Transport Kinetics, Magnetic and Electrochemical Behaviors for Supercapacitor and DSSC Applications. *Scientific Reports*. *9* (1), 1–16.

[76] **Gonzalez, Z., Ferrari, B., Sanchez-Herencia, A.J., Caballero, A., and Morales, J.** (2016) Use of Polyelectrolytes for the Fabrication of Porous NiO Films by Electrophoretic Deposition for Supercapacitor Electrodes. *Electrochimica Acta*. *211* (2016), 110–118.

[77] **Liu, R., Zhou, A., Zhang, X., Mu, J., Che, H., Wang, Y., et al.** (2021) Fundamentals, advances and challenges of transition metal compounds-based supercapacitors. *Chemical Engineering Journal*. *412* (January), 128611.

[78] **Riedel, S. and Kaupp, M.** (2009) The highest oxidation states of the transition metal elements. *Coordination Chemistry Reviews*. *253* (5–6), 606–624.

[79] **Wang, T., Chen, H.C., Yu, F., Zhao, X.S., and Wang, H.** (2019) Boosting the cycling stability of transition metal compounds-based supercapacitors. *Energy Storage Materials*. *16* (August 2018), 545–573.

[80] **Atkins, P.** (2010) *Shriver and Atkins' inorganic chemistry.* USA : Oxford University Press.

[81] **Timur, S.İ.** (1996) Eibfluss von Co, Rh und Pd auf die Sauerstoffdepolarisation an elektrochemisch beschichteten Bleianoden, Technische Universität Bergakademie, 1996.

[82] **Laubengayer, A.W., Hurd, D.T., Newkirk, A.E. and Hoard, J.L.** (1943) Boron. I. Preparation and Properties of Pure Crystalline Boron. *Journal of American Chemical Society 65* (10), 1924–1931.

[83] **Kartal, G.** (2011) *Katodik redüksiyon-termal difüzyon yöntemi ile metallerin borlanması (KRTD-bor) ve süreçlerin optimizasyonu (Ph.D. Thesis),* Istanbul Technical University, Science Engineering and Technology Institute, ISTANBUL.

[84] **Hong, J., Mutalik, S., Pescarmona, P.P., and Protesescu, L.** (2024) Metal Borides: From Industrial Classics to Versatile Colloidal Nanocrystals for Energy, Catalysis, and Hard Coatings Applications†. *Chemistry of Materials*. *36* (5), 2147–2164.

[85] **Ma, S., Ge, Y., Lian, M., Ma, X., Zhu, P., Tayal, A., et al.** (2026) Unlocking superior mechanical properties: the synergistic enhancement of hardness and fracture toughness in nanopolycrystalline tantalum diboride. *Advanced Powder Materials*. *5* (3), 100374.

[86] **Zhang, D., Li, Y., Du, X., Fan, H., and Gao, F.** (2022) Microstructure and tribological performance of boride layers on ductile cast iron under dry sliding conditions. *Engineering Failure Analysis*. *134* (November 2021), 106080.

[87] **Fahrenholtz, W.G. and Hilmas, G.E.** (2012) Oxidation of ultra-high temperature transition metal diboride ceramics. *International Materials Reviews*. *57* (1), 61–72.

[88] **Ujah, C.O. and Olubambi, P.A.** (2026) Evaluating the properties and applications of high entropy borides, nitrides and carbides. *Next Materials*. *10* (November 2025),.

[89] **Gupta, S., Patel, M.K., Miotello, A., and Patel, N.** (2020) Metal Boride-Based Catalysts for Electrochemical Water-Splitting: A Review. *Advanced Functional Materials*. *30* (1),.

[90] **Yada, K., Masaoka, H., Shoji, Y., and Tanji, T.** (1989) Studies of refractory carbides, nitrides, and borides as the thermionic emitters for electron microscopy. *Journal of Electron Microscopy Technique*. *12* (3), 252–261.

[91] **House, J.E. and House, K.A.** (2016) Boron. in: Descr. Inorg. Chem., pp. 139–150.

[92] **Greenwood, N.N., Parish, R.V. and Thornton, P.** (1965) Metal Borides, *Querterly Reviews, Chemical Society 20* (3), 441-464.

[93] **Gouget, G., Beaunier, P., Portehault, D., and Sanchez, C.** (2016) New route toward nanosized crystalline metal borides with tuneable stoichiometry and variable morphologies. *Faraday Discussions*. *191* 511–525.

[94] **Ma, T., Zhu, P., and Yu, X.** (2021) Progress in functional studies of transition metal borides∗. *Chinese Physics B*. *30* (10), 1–10.

[95] **Knoch, H.** (1991) Borides. *Concise Encyclopedia of Advanced Ceramic Materials*. 35–38.

[96] **Fahrenholtz, W.G., Binner, J., and Zou, J.** (2016) Synthesis of ultra-refractory transition metal diboride compounds. *Journal of Materials Research*. *31* (18), 2757–2772.

[97] **Ravichandran, K., Praseetha, P.K., Arun, T., and Gobalakrishnan, S.** (2018) Synthesis of Nanocomposites. In S.M. Bhagyaraj, O.S. Oluwafemi, N. Kalarikkal, S. Thomas (Eds.), *Synthesis of Inorganic Nanomaterials: Advances and Key Technologies* (pp. 141-168). Cambridge : Woodhead Publishing.

[98] **Do, J.L. and Friščić, T.** (2017) Mechanochemistry: A Force of Synthesis. *ACS Central Science*. *3* (1), 13–19.

[99] **Akkala, S.R., Kaviti, A.K., ArunKumar, T., and Sikarwar, V.S.** (2021) Progress on suspended nanostructured engineering materials powered solar distillation- a review. *Renewable and Sustainable Energy Reviews*. *143* (February), 110848.

[100] **Feng, S.H. and Li, G.H.** (2017) Hydrothermal and Solvothermal Syntheses, In R. Xu and Y. Xu. (Eds), *Modern Inorganic Synthetic Chemistry* (2nd ed. pp. 73-104), Amsterdam : Elsevier.

[101] **Daryal, B.** (2020) *Ergimiş Tuz Elektrolizi ile Metal Oksit/Sülfürden Başlanarak Metal ve Metal Borür Sentezi* (Ph.D. Thesis), Istanbul Technical University, Science Engineering and Technology Institute, ISTANBUL.

[102] **Xi, X. li, Feng, M., Zhang, L. wen, and Nie, Z. ren** (2020) Applications of molten salt and progress of molten salt electrolysis in secondary metal resource recovery. *International Journal of Minerals, Metallurgy and Materials*. *27* (12), 1599–1617.

[103] **Minh, N.Q.** (1985) Extraction of Metals by Molten Salt Electrolysis: Chemical Fundamentals and Design Factors. *Jom*. *37* (1), 28–33.

[104] **Ma, X., Jing, Z., Feng, C., Qiao, M., and Xu, D.** (2023) Research and development progress of porous foam-based electrodes in advanced electrochemical energy storage devices: A critical review. *Renewable and Sustainable Energy Reviews*. *173* (December 2022), 113111.

[105] **Salleh, N.A., Kheawhom, S., and Mohamad, A.A.** (2020) Characterizations of nickel mesh and nickel foam current collectors for supercapacitor application. *Arabian Journal of Chemistry*. *13* (8), 6838–6846.

[106] **Pimsawat, A., Tangtrakarn, A., Pimsawat, N., and Daengsakul, S.** (2019) Effect of Substrate Surface Roughening on the Capacitance and Cycling Stability of Ni(OH)2 Nanoarray Films. *Scientific Reports*. *9* (1), 1–11.

[107] **Ardizzone, S., Fregonora G., T.S.** (1990) “Inner” and “Outer” Active Surface of RuO, Electrodes. *Electrochimica Acta*. *35* 263–267.

[108] **Wang, J., Polleux, J., Lim, J., and Dunn, B.** (2007) Pseudocapacitive contributions to electrochemical energy storage in TiO2 (anatase) nanoparticles. *Journal of Physical Chemistry C*. *111* (40), 14925–14931.

[109] **Pholauyphon, W., Charoen-amornkitt, P., Suzuki, T., and Tsushima, S.** (2024) Perspectives on accurately analyzing cyclic voltammograms for surface- and diffusion-controlled contributions. *Electrochemistry Communications*. *159* (December 2023), 107654.

[110] **Czagany, M., Hompoth, S., Windisch, M., and Baumli, P.** (2023) Investigation of the Supercapacitive Behavior of Electroless Ni-B Coatings. *Metals*. *13* (7), 1–19.

[111] **Chen, B., Tang, H., Zhang, N., and Sun, Q.** (2024) Amorphous Nickel Boride Deposited on Silicon Nanowires and Carbon Nanowall Templates for High-Performance Micro-supercapacitors. *Journal of Materials Engineering and Performance*. *33* (5), 2268–2278.

[112] **Chen, Y., Wang, Y., Sun, P., Yang, P., Du, L., and Mai, W.** (2015) Nickel oxide nanoflake-based bifunctional glass electrodes with superior cyclic stability for energy storage and electrochromic applications. *Journal of Materials Chemistry A*. *3* (41), 20614–20618.

[113] **Mohamed, N., Örnek, C., Timur, S., and Ürgen, M.** (2022) Anodic behavior of nickel in sub-molten KOH and its relevance for the production of electroactive nickel oxides. *Surfaces and Interfaces*. *31* (April),.

[114] **Chen, Y., Zhou, T., Li, L., Pang, W.K., He, X., Liu, Y.N., et al.** (2019) Interfacial Engineering of Nickel Boride/Metaborate and Its Effect on High Energy Density Asymmetric Supercapacitors. *ACS Nano*. *13* (8), 9376–9385.

[115] **Li, W., Wang, S., Wu, M., Wang, X., Long, Y., and Lou, X.** (2017) Direct aqueous solution synthesis of an ultra-fine amorphous nickel-boron alloy with superior pseudocapacitive performance for advanced asymmetric supercapacitors. *New Journal of Chemistry*. *41* (15), 7302–7311.

[116] **Zhang, W., Tan, Y., Gao, Y., Wu, J., Tang, B., and Zhao, J.** (2014) Amorphous nickel-boron and nickel-manganese-boron alloy as electrochemical pseudocapacitor materials. *RSC Advances*. *4* (53), 27800–27804.

[117] **Wan, L., Wang, Y., Jiang, D., Zhang, Y., Xie, M., Chen, J., et al.** (2023) Constructing nickel sulfide @ nickel boride hybrid nanosheet arrays with crystalline/amorphous interfaces for supercapacitors. *Journal of Colloid and Interface Science*. *649* (June), 815–825.

[118] **Tan, Y., Zhang, W., Gao, Y., Wu, J., and Tang, B.** (2015) Synthesis of ordered mesoporous carbon nanofiber arrays/nickel–boron amorphous alloy with high electrochemical performance for supercapacitor. *Journal of Materials Science*. *50* (13), 4622–4628.

[119] **Tripathy, R.K., Samantara, A.K., and Behera, J.N.** (2021) Metal-organic framework (MOF)-derived amorphous nickel boride: an electroactive material for electrochemical energy conversion and storage application. *Sustainable Energy and Fuels*. *5* (4), 1184–1193.

[120] **Ma, X., Ren, Q., Wang, H., and Ji, S.** (2018) Mesoporous and amorphous NiCoBP alloys with high specific capacitance for supercapacitors. *Ionics*. *24* (2), 529–537.

[121] **Chen, B., Tang, H., Zhang, N., and Sun, Q.** (2023) Amorphous Nickel Boride Deposited on Silicon Nanowires and Carbon Nanowall Templates for High-Performance Micro-supercapacitors. *Journal of Materials Engineering and Performance*.

[122] **Zheng, Y. zhen, Ding, H. yang, and Zhang, M. lin** (2009) Preparation and electrochemical properties of nickel oxide as a supercapacitor electrode material. *Materials Research Bulletin*. *44* (2), 403–407.

[123] **Pilban Jahromi, S., Pandikumar, A., Goh, B.T., Lim, Y.S., Basirun, W.J., Lim, H.N., et al.** (2015) Influence of particle size on performance of a nickel oxide nanoparticle-based supercapacitor. *RSC Advances*. *5* (18), 14010–14019.

[124] **Lin, P., She, Q., Hong, B., Liu, X., Shi, Y., Shi, Z., et al.** (2010) The Nickel Oxide/CNT Composites with High Capacitance for Supercapacitor. *Journal of The Electrochemical Society*. *157* (7), A818.

[125] **Cao, P., Wang, L., Xu, Y., Fu, Y., and Ma, X.** (2015) Facile hydrothermal synthesis of mesoporous nickel oxide/reduced graphene oxide composites for high performance electrochemical supercapacitor. *Electrochimica Acta*. *157* 359–368.

[126] **Schoetz, T., Gordon, L.W., Ivanov, S., Bund, A., Mandler, D., and Messinger, R.J.** (2022) Disentangling faradaic, pseudocapacitive, and capacitive charge storage: A tutorial for the characterization of batteries, supercapacitors, and hybrid systems. *Electrochimica Acta*. *412* (February), 140072.

[127] **Sharma, S. and Chand, P.** (2023) Supercapacitor and electrochemical techniques: A brief review. *Results in Chemistry*. *5* (November 2022), 100885.

[128] **Mei, B.A., Lau, J., Lin, T., Tolbert, S.H., Dunn, B.S., and Pilon, L.** (2018) Physical Interpretations of Electrochemical Impedance Spectroscopy of Redox Active Electrodes for Electrical Energy Storage. *Journal of Physical Chemistry C*. *122* (43), 24499–24511.

[129] **Laschuk, N.O., Easton, E.B., and Zenkina, O. V.** (2021) Reducing the resistance for the use of electrochemical impedance spectroscopy analysis in materials chemistry. *RSC Advances*. *11* (45), 27925–27936.

[130] **Yewale, M.A., Kadam, R.A., Kaushik, N.K., Koduru, J.R., Velhal, N.B., Nakate, U.T., et al.** (2023) Interconnected plate-like NiCo2O4 microstructures for supercapacitor application. *Materials Science and Engineering: B*. *287* (November 2022), 116072.

[131] **Yewale, M.A., Kadam, R.A., Kaushik, N.K., Nguyen, L.N., Nakate, U.T., Lingamdinne, L.P., et al.** (2022) Electrochemical supercapacitor performance of NiCo2O4 nanoballs structured electrodes prepared via hydrothermal route with varying reaction time. *Colloids and Surfaces A: Physicochemical and Engineering Aspects*. *653* (August), 129901.

[132] **Karthik, R., Sukanya, R., Chen, S.M., Hasan, M., Dhakal, G., Shafi, P.M., et al.** (2023) Development of an Amorphous Nickel Boride/Manganese Molybdate Heterostructure as an Efficient Electrode Material for a High-Performance Asymmetric Supercapacitor. *ACS Applied Materials and Interfaces*. *15* (9), 11927–11939.

[133] **Wagner, C.D.** (1991) NIST X-ray Photoelectron Spectrometry Database. *NIST Standard Reference Database 20, Version 4.1*. 1–76.

[134] **Zhou, Z., Zhang, K., Xiao, G., Wang, Y., He, Q., Wang, N., et al.** (2023) Surface Growth of Boron Nitride Nanotubes through Boron Source Design. *Advanced Functional Materials*. *33* (48), 1–8.

[135] **Liang, X., Dong, R., Li, D., Bu, X., Li, F., Shu, L., et al.** (2018) Coupling of Nickel Boride and Ni(OH)2 Nanosheets with Hierarchical Interconnected Conductive Porous Structure Synergizes the Oxygen Evolution Reaction. *ChemCatChem*. *10* (20), 4555–4561.

[136] **Yewale, M.A., Kumar, V., Kadam, R.A., Kharade, R.B., Teli, A.M., Beknalkar, S.A., et al.** (2023) Wrapped nanochain microstructures of Ni3V2O8 nanoparticles for supercapacitor applications using the hydrothermal method. *Journal of Energy Storage*. *73* (PB), 109005.

[137] **Schild, D., Ulrich, S., Ye, J., and Stüber, M.** (2010) XPS investigations of thick, oxygen-containing cubic boron nitride coatings. *Solid State Sciences*. *12* (11), 1903–1906.

[138] **Ong, C.W., Huang, H., Zheng, B., Kwok, R.W.M., Hui, Y.Y., and Lau, W.M.** (2004) X-ray photoemission spectroscopy of nonmetallic materials: Electronic structures of boron and BxOy. *Journal of Applied Physics*. *95* (7), 3527–3534.

[139] **Casas-Cabanas, M., Radin, M.D., Kim, J., Grey, C.P., Van Der Ven, A., and Palacín, M.R.** (2018) The nickel battery positive electrode revisited: Stability and structure of the β-NiOOH phase. *Journal of Materials Chemistry A*. *6* (39), 19256–19265.

[140] **Zhang, C.C., Shi, J., Hartlaub, S., Palamara, J.P., Petrovic, I., and Yilmaz, B.** (2021) In-situ diffuse reflective infrared Fourier transform spectroscopy (DRIFTS) study on Ni passivation in FCC catalysts from boron-based technology. *Catalysis Communications*. *150* 106273.

[141] **Momma, K. and Izumi, F.** (2008) VESTA: A three-dimensional visualization system for electronic and structural analysis. *Journal of Applied Crystallography*. *41* (3), 653–658.

[142] **Gaire, M., Liang, K., Luo, S., Subedi, B., Adireddy, S., Schroder, K., et al.** (2020) Nanostructured manganese oxides electrode with ultra-long lifetime for electrochemical capacitors. *RSC Advances*. *10* (28), 16817–16825.

[143] **Li, T., Zhu, C., Yang, X., Gao, Y., He, W., Yue, H., et al.** (2017) Co3O4 nanoneedle@electroactive nickel boride membrane core/shell arrays: A novel hybrid for enhanced capacity. *Electrochimica Acta*. *246* 226–233.

[144] **Rama Raju, G.S., Pavitra, E., Nagaraju, G., Sekhar, S.C., Ghoreishian, S.M., Kwak, C.H., et al.** (2018) Rational design of forest-like nickel sulfide hierarchical architectures with ultrahigh areal capacity as a binder-free cathode material for hybrid supercapacitors. *Journal of Materials Chemistry A*. *6* (27), 13178–13190.

[145] **Gao, M., Li, Y., Yang, J., Liu, Y., Liu, Y., Zhang, X., et al.** (2022) Nickel-cobalt (oxy)hydroxide battery-type supercapacitor electrode with high mass loading. *Chemical Engineering Journal*. *429* (May 2021), 132423.

[146] **Deng, B., Yang, Y., Liu, Y., Yin, B., and Yang, M.** (2022) A hierarchically combined reduced graphene oxide/Nickel oxide hybrid supercapacitor device demonstrating compliable flexibility and high energy density. *Journal of Colloid and Interface Science*. *618* 399–410.

[147] **Wang, W., Liu, Y., Wang, M., Ren, G., Wu, S., and Shen, J.** (2018) Facilely prepared oxidized carbon Fiber@Co 3 O 4 @RGO as negative electrode for a novel asymmetric supercapacitor with high areal energy and power density. *Applied Surface Science*. *450* 66–76.

[148] **Kong, M., Wang, Z., Wang, W., Ma, M., Liu, D., Hao, S., et al.** (2017) NiCoP Nanoarray: A Superior Pseudocapacitor Electrode with High Areal Capacitance. *Chemistry - A European Journal*. *23* (18), 4435–4441.

[149] **Zhili, D.** (2022) Fundamentals of Crystallography, Powder X-ray Diffraction, and Transmission Electron Microscopy for Materials Scientists. .

[150] **Omori, M.** (2021) Powder X-ray Diffraction Basic Course Second installment: Selection of equipment configuration to obtain high-quality data. *Rigaku Journal*. *37* (1), 2021.

[151] **Osarinmwian, C. and Roberts, E.P.L.** (2023) Modelling diffusion controlled electro-deoxidation of metal oxide to metal in molten salt. *Journal of Solid State Electrochemistry*. *27* (12), 3383–3391.

[152] **De Silva, U. and Coons, T.P.** (2024) Molten Salt Electrodeposition: Review. *Energies*. *17* (15),.

[153] **Schneider, S., Eppler, F., Weber, M., Olowojoba, G., Weiss, P., Hübner, C., et al.** (2016) Multiscale dispersion-state characterization of nanocomposites using optical coherence tomography. *Scientific Reports*. *6* (July), 1–12.

[154] **Nzodom Djozing, W., Valange, S., Nikitenko, S.I., and Chave, T.** (2024) Sonohydrothermal synthesis of zeolite A and its phase transformation into sodalite. *Dalton Transactions*. *53* (39), 16407–16421.

[155] **Wang, H., Yan, J., Wang, R., Li, S., Brett, D.J.L., and Ji, S.** (n.d.) Nano-chain amorphous CoB @ porous Ni (OH) 2 ultrathin sheets as a high-performance supercapacitor material.

[156] **Arslan-Kaba, M., Timur, S., and Kartal Sireli, G.** (2024) Evaluating the mechanism and the capacitive properties of nickel boride electrodes for supercapacitor applications. *Journal of Energy Storage*. *99* (A).

[157] **Sandford, C., Edwards, M.A., Klunder, K.J., Hickey, D.P., Li, M., Barman, K., et al.** (2019) A synthetic chemist's guide to electroanalytical tools for studying reaction mechanisms. *Chemical Science*. *10* (26), 6404–6422.

[158] **Sampaio, R.S., Correia, J.P., Silva, T.M., and Montemor, M.F.** (2025) New insights into the degradation of pseudocapacitive MnOx under floating. *Journal of Energy Storage*. *131* (PA), 117546.

[159] **Xu, N., Cao, G., Chen, Z., Kang, Q., Dai, H., and Wang, P.** (2017) Cobalt nickel boride as an active electrocatalyst for water splitting. *Journal of Materials Chemistry A*. *5* (24), 12379–12384.

[160] **Venkatkarthick, R., Qin, J., and Maiyalagan, T.** (2022) Amorphous cobalt boride nanoparticles incorporated vanadium carbide MXene composite for asymmetric supercapacitor applications. *International Journal of Energy Research*. *46* (15), 22474–22485.

[161] **Hou, J.F., Gao, J.F., and Kong, L. Bin** (2020) Boosting the performance of cobalt molybdate nanorods by introducing nanoflake-like cobalt boride to form a heterostructure for aqueous hybrid supercapacitors. *Journal of Colloid and Interface Science*. *565* 388–399.

[162] **Fang, S., Chen, Y., Wang, S., Xu, J., Xia, Y., Yang, F., et al.** (2023) Modified CNTs interfacial anchoring and particle-controlled synthesis of amorphous cobalt-nickel-boron alloy bifunctional materials for NaBH4 hydrolysis and supercapacitor energy storage. *Journal of Alloys and Compounds*. *936* 167990.

[163] **Wang, H., Yan, J., Wang, R., Li, S., Brett, D.J.L., Key, J., et al.** (2017) Toward high practical capacitance of Ni(OH)2 using highly conductive CoB nanochain supports. *Journal of Materials Chemistry A*. *5* (1), 92–96.

[164] **Zhang, L., Chai, S.S., Zhang, W. Bin, Guo, S.B., Han, X.W., Guo, Y.W., et al.** (2022) Cobalt boride on clay minerals for electrochemical capacitance. *Applied Clay Science*. *218* (September 2021), 106416.

[165] **Yan, J., Zhu, C., Liu, B., and Shu, R.** (2022) Co(OH)2 nanosheets anchored on CoB nanochains with enhanced electrochemical performance. *Journal of Materials Science*. *57* (44), 20580–20588.

[166] **Yang, F., Ma, X.J., Liu, J.H., Chen, B., Yang, K., Liu, X.Y., et al.** (2025) Acid-etched halloysite and Co-Ni-B composites for high-performance supercapacitor application. *Applied Clay Science*. *263* (August 2024), 107637.

[167] **Chen, R., Liu, L., Zhou, J., Hou, L., and Gao, F.** (2017) High-performance nickel-cobalt-boron material for an asymmetric supercapacitor with an ultrahigh energy density. *Journal of Power Sources*. *341* 75–82.

[168] **Zhang, Q., Zhao, J., Wu, Y., Li, J., Jin, H., Zhao, S., et al.** (2020) Rapid and Controllable Synthesis of Nanocrystallized Nickel-Cobalt Boride Electrode Materials via a Mircoimpinging Stream Reaction for High Performance Supercapacitors. *Small*. *16* (39),.

[169] **Meng, Q., Xu, W., Zhu, S., Liang, Y., Cui, Z., Yang, X., et al.** (2019) Low-cost fabrication of amorphous cobalt-iron-boron nanosheets for high-performance asymmetric supercapacitors. *Electrochimica Acta*. *296* 198–205.

[170] **Gao, J.F., Hou, J.F., and Kong, L. Bin** (2021) Amorphous Cobalt Boride Alloy Synthesized by Liquid Phase Methods as Electrode Materials for Electrochemical Capacitors. *Particle and Particle Systems Characterization*. *38* (5), 1–7.

[171] **Phonsuksawang, P., Khajondetchairit, P., Ngamchuea, K., Butburee, T., Sattayaporn, S., Chanlek, N., et al.** (2021) Enhancing performance of NiCo2S4/Ni3S2 supercapacitor electrode by Mn doping. *Electrochimica Acta*. *368* 137634.

[172] **Aloqayli, S., Ranaweera, C.K., Wang, Z., Siam, K., Kahol, P.K., Tripathi, P., et al.** (2017) Nanostructured cobalt oxide and cobalt sulfide for flexible, high performance and durable supercapacitors. *Energy Storage Materials*. *8* (April), 68–76.

[173] **Shinde, V.R., Mahadik, S.B., Gujar, T.P., and Lokhande, C.D.** (2006) Supercapacitive cobalt oxide (Co 3 O 4) thin films by spray pyrolysis. *Applied Surface Science*. *252* (20), 7487–7492.

[174] **Wang, Q., Yang, F., Yu, Z., Yoon, S., and Yoo, B.** (2024) Potential difference-induced electrodeposition of defect-rich α-cobalt hydroxide on porous copper (PCu): High-voltage performance of supercapacitor. *Journal of Alloys and Compounds*. *1008* (September), 176690.

CURRICULUM VITAE

Name Surname **:** Mehtap Arslan Kaba

EDUCATION **:**

- **B.Sc.** **:** 2017, Istanbul Technical University, Faculty of Chemical and Metallurgical Engineering, Metallurgical and Materials Engineering Department
- **M.Sc.** **:** 2020, Istanbul Technical University, Faculty of Chemical and Metallurgical Engineering, Metallurgical and Materials Engineering Department

PROFESSIONAL EXPERIENCE AND REWARDS:

- 2019 - present Research Assistant
- 2017 – The Best Graduation Project Award

PUBLICATIONS, PRESENTATIONS AND PATENTS ON THE THESIS:

- **Arslan-Kaba, M.**, Timur, S. Sireli, G. 2024. Evaluating the mechanism and the capacitive properties of nickel boride electrodes for supercapacitor applications, *Journal of Energy Storage*, 99(Part A), 113299.
- **Arslan-Kaba, M.**, Timur, S. Sireli, G. 2025. Production of high capacity porous nickel borides via novel molten salt electrolysis, *Solid State Sciences*, 163, 107889.
- **Arslan-Kaba, M.,** Timur, S. Sireli, G. 2024: 22nd International Symposium on Boron, Borides and Related Materials. International Symposium, September 8-12, 2024 Istanbul, Turkey.
- **Arslan-Kaba, M.**, S. Sireli, G. 2025: BORON2025. International Boron Symposium, December 3-5, 2025 Ankara, Turkey.
- **Arslan-Kaba, M.,** Sireli, G. 2025: The World Energy Storage Conferance, December 7-10, 2025 Istanbul, Turkey.

OTHER PUBLICATIONS, PRESENTATIONS AND PATENTS:

- Ozguvenc, E.E., **Arslan-Kaba, M.,** Sireli G., 2024. Electrochemical synthesis of vanadium boride powders from their oxide salts, *Journal of Alloys and Copmpounds*, 1005, 176029.

- Yanik, S., **Arslan.M,** Sireli, G., 2024. Chemical Strengthening of Soda Lime Glasses via Ion Exchange Method, *Journal of the Turkish Chemical Society Section A: Chemistry,* 11, 1237-1244.
- Sireli, G. Yuce, H., **Arslan, M**., Karimzadehkhoei, M, Timur, S. 2023. Improving the surface performance of discarded AISI T1 steel by cathodic reduction and thermal diffusion-based boriding, *Journal of Materials Engineering and Performance,* 32(21), 9504-9514.
- **Arslan-Kaba, M.**, Karimzadehkhoei, Keddam, M. Timur, S. Sireli, G. 2023. An experimental and modelling study on pulse current integrated CRTD-Bor process, *Materials Chemistry and Physics,* 302, 127735
- **Arslan, M.**, Karimzadehkhoei, M., Sireli, G., Coskun, O.K., Sert M., Timur S. 2022. Investigating Growth of Iron Borides with the Formation of Monolithic Fe2B Layer on AISI 304 Stainless Steel via Cathodic Reduction and Thermal Diffusion-Based Boriding, *Journal of Materials Engineering and Performance,* 31, 3274-3286.
- **Arslan, M.** Coskun, O.K., Karimzadehkhoei, M., Sireli, G., Timur, S. 2022. Evaluation of pulse current integrated CRTD-Bor for boron diffusion in low carbon steel, *Materials Letters,* 308, 131299.
- **Arslan, M.**, Ok A.C., Sireli, G., Timur, S. 2022. Investigation on structural and tribological properties of borided gear steel after phase homogenization, *Surface and Coating Technologies*, 429, 127967.
- **Arslan, M.,** Coskun, O.K., Sireli, G., Timur, S. 2021: 20th International Metallurgical and Materials Congress (IMMC’21), June, 2021, Istanbul, Turkey.
- Yanik, S., Turkay, B., Ilhan, I.C., **Arslan, M.,** Sireli, G., 2022: 26th International Congress on Glass/DGG Conference (ICG 2022), 3-8 July, 2022, Berlin, Germany.
- Coskun, O.K., **Arslan, M.,** Karimzadehkhoei, M., Sireli, G. Timur, S. 2021: 20th International Metallurgical and Materials Congress (IMMC’21), June, 2021, Istanbul, Turkey.
- Orman. R. Daryal, B., Coskun, O., **Arslan, M.** Sireli, G., Timur, S. 2021: 20th International Metallurgical and Materials Congress (IMMC’21), June, 2021, Istanbul, Turkey.
- Özer, O.C., Şireli, G., Gezici, U.O., **Arslan-Kaba, M.,** Timur, S. 2023: International Graduate Research Symposium (IGRS’23), 16-18 May, 2023, Istanbul Turkey.
- Tunçyürek, E. Gezici, U.O., **Arslan-Kaba, M.** Karimzadehkhoei, M., Tunç, M., Timur, S. 2023: International Graduate Research Symposium (IGRS’23), 16-18 May, 2023, Istanbul Turkey.
- Özgüvenç, E.E., **Arslan-Kaba, M.**, Sireli, G. 2024: International Graduate Research Symposium (IGRS’24), 8-10 May, 2023, Istanbul Turkey.
- Heper, K.K., **Arslan-Kaba, M.** Sireli, G. . 2024: International Graduate Research Symposium (IGRS’24), 8-10 May, 2023, Istanbul Turkey.
- Akgül D., **Arslan-Kaba, M.** Sireli, G. . 2024: International Graduate Research Symposium (IGRS’24), 8-10 May, 2023, Istanbul Turkey.

- Tunç, M., **Arslan-Kaba, M.,** Sireli, G., Sözer, B., Timur, S. 2024: 22th International Metallurgical and Materials Congress (IMMC’24), 19-21 September, 2021, Istanbul, Turkey.
- Gezici, U.O., Baştürkcü, E., **Arslan-Kaba, M.** Ertürk, S., Sözer, B., Sireli, G., Timur, S., 2024: 22th International Metallurgical and Materials Congress (IMMC’24), 19-21 September, 2021, Istanbul, Turkey.
- Özer, O., **Arslan-Kaba, M.,** Sireli, G., Sözer, B., Timur, S. 2024: 22th International Metallurgical and Materials Congress (IMMC’24), 19-21 September, 2021, Istanbul, Turkey.
- Demir E., **Arslan-Kaba, M.,** Sireli, G.K, 2024: 25th International Conference on Advances in Materials&Processing Technologies (AMPT2024), October 30-November 3, 2024, Istanbul, Turkey.
- Nalcı, D. **Arslan-Kaba,M.,** Sireli, G., Kazmanlı, K. 2025: International Graduate Research Symposium (IGRS’25), 12-14 May, 2023, Istanbul Turkey.
- Nalcı, D. **Arslan-Kaba,M.,** Sireli, G., Kazmanlı, K. 2025: 19th Nanoscience and Nanotechnology Conference, 27-29 August, 2025, Ankara, Turkey.
- Özgüvenç, E.E., Yanık, S., **Arslan-Kaba, M.**, S. Sireli, G. 2025: BORON2025. International Boron Symposium, December 3-5, 2025 Ankara, Turkey.
- Heper K.K., Ertürk, S., **Arslan-Kaba, M.,** Sireli, G., **Arslan-Kaba, M.**, S. Sireli, G. 2025: BORON2025. International Boron Symposium, December 3-5, 2025 Ankara, Turkey.
- Doğduaslan, N.M., Özer, O.C., **Arslan-Kaba, M.**, S. Sireli, G. 2025: BORON2025. International Boron Symposium, December 3-5, 2025 Ankara, Turkey.